NEAR-BED HYDRODYNAMICS AND SEDIMENT TRANSPORT IN THE SWASH ZONE

by

Thijs Lanckriet

A dissertation submitted to the Faculty of the University of Delaware in partial fulfillment of the requirements for the degree of Doctor of Philosophy in Civil Engineering

Summer 2014

NEAR-BED HYDRODYNAMICS AND SEDIMENT TRANSPORT

IN THE SWASH ZONE

by

Thijs Lanckriet

Approved: _____

Harry W. Shenton III, Ph.D.
Chair of the Department of Civil and Environmental Engineering

Approved: _____

Babatunde A. Ogunnaike, Ph.D.
Dean of the College of Engineering

Approved: _____

James G. Richards, Ph.D.
Vice Provost for Graduate and Professional Education

I certify that I have read this dissertation and that in my opinion it meets the academic and professional standard required by the University as a dissertation for the degree of Doctor of Philosophy.

Signed: _____

Jack A. Puleo, Ph.D.
Professor in charge of dissertation

I certify that I have read this dissertation and that in my opinion it meets the academic and professional standard required by the University as a dissertation for the degree of Doctor of Philosophy.

Signed: _____

Tian-Jian Hsu, Ph.D.
Member of dissertation committee

I certify that I have read this dissertation and that in my opinion it meets the academic and professional standard required by the University as a dissertation for the degree of Doctor of Philosophy.

Signed: _____

James T. Kirby, Ph.D.
Member of dissertation committee

I certify that I have read this dissertation and that in my opinion it meets the academic and professional standard required by the University as a dissertation for the degree of Doctor of Philosophy.

Signed: _____

Gerd Masselink, Ph.D.
Member of dissertation committee

"I do not know what I may appear to the world, but to myself I seem to have been only like a boy playing on the sea-shore, and diverting myself in now and then finding a smoother pebble or a prettier shell than ordinary, whilst the great ocean of truth lay all undiscovered before me."

Sir Isaac Newton

ACKNOWLEDGMENTS

I wish to thank my advisor, Jack Puleo, for the invaluable guidance that he has given me during my PhD. I am immensely grateful for the many enlightening discussions, the advice, and all the opportunities he has given me to develop myself through field work, travel, and teaching. I also treasure the countless great memories, the many sand-covered, sleep-deprived laughs we had during field work, and all the Duvels we imbibed. Jack truly went above and beyond as an advisor and made these past five years an experience I will never forget.

I also want to thank my doctoral committee members, Tom Hsu, Jim Kirby, and Gerd Masselink for their input in my research. A special thanks goes out to Gerd Masselink for graciously hosting me as a visiting scholar at the Coastal Processes Research Group at Plymouth University. Many thanks also go to the entire team of the BeST field experiment: Chris Blenkinsopp, Daniel Buscombe, Daniel Conley, Claire Earlie, Peter Ganderton, Gerd Masselink, Robert McCall, Luis Melo De Almeida, Tim Poate, Barbara Proença, Jack Puleo, Paul Russell, Megan Sheridan, and Ian Turner, it was an honor to count sand grains with all of you, and I hope you enjoy reading this dissertation as a product of our work. The development of the Conductivity Concentration Profiler (CCP) was also essential to obtaining the measurements presented in this work. I gratefully acknowledge Michael Davidson, Joe Faries, Betsy Hicks and Jack Puleo for developing and testing the earlier versions of this sensor, thus paving the way for the development of the current version CCP

that I used. Nick Waite was the mastermind behind the development of the electronics of the current CCP, and I am greatly indebted to Nick for his work.

Lastly, many thanks go to all my fellow students, researchers and staff at the Ocean Engineering Lab at the University of Delaware and at Plymouth University for the great work experience, to all my friends who supported me throughout this journey, and to my family in Belgium, who had to miss me for the past five years.

TABLE OF CONTENTS

LIST OF TABLES

LIST OF FIGURES

LIST OF SYMBOLS AND ABBREVIATIONS

ADCP	Acoustic Doppler Current Profiler
Bardex II	Barrier Dynamics Experiment II
BeST	Beach Sand Transport study
c	Sediment concentration (expressed as a volume fraction)
C	Sheet load
CCP	Conductivity Concentration Profiler
CCM	Conductivity Concentration Meter
d	(Generic) grain diameter
d_{50}	Median grain diameter
$D(z,r,t)$	Structure function
UDM	Ultrasonic Distance Meter
$E(k)$	Wavenumber spectrum
EMCM	Electromagnetic Current Meter
f	Frequency
F	Formation factor
FOBS	Fiber Optic Backscatter Sensor
g	Gravitational acceleration
h	Water depth
H_s	Significant wave height
I	Normalized pixel intensity
IBC	In-Situ Bed Camera

k	Wavenumber
m	Calibration coefficient for Archie's law
NTP	Network Time Protocol
$O(...)$	On the order of magnitude of
OBS	Optical Backscatter Sensor
$P(f)$	Frequency spectrum
$\mathcal{P}$	Turbulence production rate
PIV	Particle Image Velocimetry
PV	Profiling Velocimeter
r	Pearson correlation coefficient, separation distance
R^2	Coefficient of determination
RBG	Red-Blue-Green (visible-band)
Ri	Gradient Richardson number
s	relative density of sediment
S	Turbulence reduction due to stratification
T_p	Spectral peak period
u	Cross-shore velocity
u_*	Friction velocity
UTC	Coordinated Universal Time
v	Alongshore velocity
w	Vertical velocity
β	Bottom slope
δ_s	Sheet flow layer thickness
ϵ	Turbulence dissipation rate

$\bar{\epsilon}$	Vertically averaged dissipation rate
θ	Shields number
κ	Von Kármán constant
ν	Molecular kinematic viscosity
ν_t	Eddy viscosity
π	Dessert
ρ_f	Density of water (in the absence of sediment)
ρ_s	Sediment density
σ_c	Prandtl-Schmidt number
σ_f	Electrical conductivity of fluid in absence of sediment
σ_m	Electrical conductivity of sand/fluid mixture
τ_b	Bed shear stress
ϕ	Porosity
Φ	Volumetric sheet load
ψ	Mobility number

ABSTRACT

The swash zone, the section of the beach that is alternatingly inundated and exposed as a result of wave runup, is an important part of the nearshore coastal zone because of hydrodynamic and sediment transport processes that affect the morphology and ecology of the broader littoral area. The understanding of these swash-zone processes is poor and suffers from a lack of detailed measurements under natural conditions. A new comprehensive dataset of swash zone processes was collected during the Beach Sand Transport (BeST) field study, which was conducted in Perranporth (UK) in October 2012. Measurements were taken for approximately 3 hours around high tide during 10 consecutive tidal cycles, and included several innovative measurement techniques. First, a novel Conductivity Concentration Profiler (CCP) was developed that measures sediment concentration in the sheet flow layer using electrical conductivity as a proxy. The CCP measures a 29-point conductivity profile at 1 mm resolution by multiplexing through a vertical array of 32 plate electrodes. The relationship between conductivity and sediment concentration was calibrated during lab experiments with known masses of sediment neutrally suspended in a heavy liquid. The horizontal and vertical extent of the CCP measurement volume was analyzed using a numerical model of the electric field around the sensor, and indicated that sheet flow layers with a thickness greater than 5 mm are resolved accurately. CCP measurements during the BeST field study demonstrated that sheet flow occurs frequently in the swash zone during both the uprush and the backwash. A detailed analysis of sheet flow focusing on quasi-steady

backwash events (when effects of phase lags, surface-generated turbulence and accelerations were small) showed that the sheet flow sediment concentration profile has a linear shape in the lower section of the sheet flow layer and a power-law shape in the upper section. The shape of the concentration profile is self-similar and can be described by a single curve for sheet flow layer thicknesses ranging from 6 to 18 mm. The sheet flow layer thickness and sheet load (the sediment mass mobilized in the sheet flow layer) are well-correlated with the hydrodynamic forcing represented by the mobility number. Secondly, high-resolution near-bed velocity profiles were measured by three profiling acoustic Doppler velocimeters and were used to estimate near-bed turbulence dissipation rates, derived from the structure function. Dissipation rates between $6 \cdot 10^{-5}$ m^2/s^3 and $8 \cdot 10^{-3}$ m^2/s^3 were observed. Temporal phasing of strong turbulence dissipation events agreed well with remotely sensed pixel intensity associated with wave breaking. Bore-generated turbulence decayed rapidly following bore arrival and followed a decay rate similar to grid turbulence. Vertical dissipation profiles demonstrate that turbulence was dominated by (advected) bore-generated turbulence during the uprush and initial stages of the backwash, and by bed-generated turbulence during the later stages of the backwash. A scaling analysis shows that near the bed, sediment-induced density stratification effects on the turbulent kinetic energy budget may have been an order of magnitude larger than turbulence dissipation.

Chapter 1

INTRODUCTION

This dissertation discusses hydrodynamic and sediment transport processes that take place in the swash zone of sandy beaches. A First International Workshop on Swash Zone Processes was convened in Lisbon, Portugal in September 2004 [*Puleo and Butt*, 2006] to synthesize swash zone research findings and identify a number of key needs for future research. Several recommendations made during the workshop formed the basis for the work presented in this dissertation, including the need for comprehensive field measurements of swash zone processes in general and measurements of turbulence and sheet flow sediment transport in particular [*Masselink and Puleo*, 2006]. A second workshop will take place in Newark, Delaware, in July 2014, ten years after the first workshop and roughly at the time of printing of this dissertation. This workshop will provide a new synthesis of the swash zone research conducted since the previous workshop, as well as a new set of recommendations for future research, and bring the process full circle.

This work is organized as follows. A concise overview of the state of the art on the swash zone and sheet flow processes is given in the remainder of this chapter. Chapter 2 discusses the development of the Conductivity Concentration Profiler, a new sensor to measure sediment concentration in the sheet flow layer. Experimental conditions are described in Chapter 3 for the Beach Sand Transport (BeST) field experiment which provided the measurements discussed in this work. Results from the field measurements of sheet flow processes are discussed in Chapter 4 and of

turbulence dissipation rates in Chapter 5. Chapter 6 provides a set of recommendations for further research, and general conclusions are given in Chapter 7.

1.1 The Swash Zone

The swash zone is defined as the section of the beach that is intermittently submerged and subaerial as a result of wave action, i.e. the area between wave run-up and run-down [*Elfrink and Baldock*, 2002]. Other definitions have also been proposed; e.g. *Puleo et al.* [2000] define the seaward edge of the swash zone as the location where bore turbulence begins to significantly affect the bed.

The swash zone is an area of active research interest for various reasons [*Bakhtyar et al.*, 2009a]. First, it is an important area for beach morphodynamics since it is an area of intense sediment transport as well as a sediment transport boundary condition. In the cross-shore, the swash zone is the place where sediment exchange between the subaqueous and subaerial zones of the beach and hence shoreline change occur [*Masselink and Hughes*, 1998]. In the alongshore sense, between 5% and 60% of the total alongshore sediment transport takes place in the

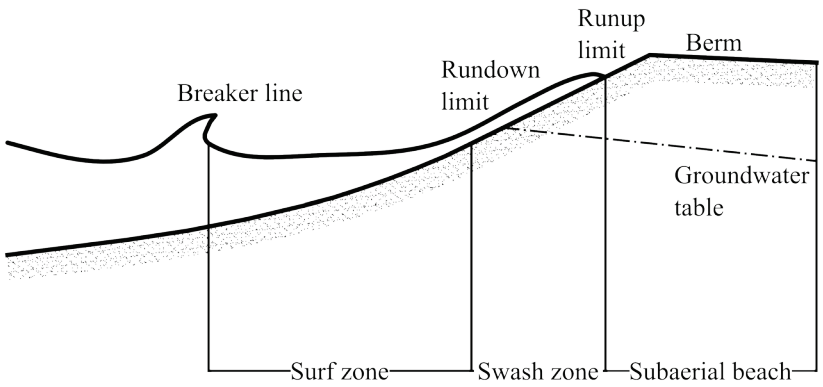

Figure 1.1: Location of the swash zone on the beach.

swash zone, depending on the breaker type [*Bodge*, 1989; *Wang et al.*, 2002]. For aeolian sediment transport on the subaerial beach, the swash zone acts as the seaward boundary where sediment pick-up begins [*Bauer and Davidson-Arnott*, 2003].

The swash zone is also important for nearshore hydrodynamics. Wave runup processes that take place in the swash zone are crucial to coastal safety and dune erosion [*Stockdon et al.*, 2006]. The swash zone is also the landward boundary for breaking wave energy dissipation and turbulence generation. Breaking wave-generated turbulence is exchanged between the surf zone and the swash zone, with the swash zone acting as a sink for surf zone turbulence [*Sou et al.*, 2010]. The swash zone is also a crucial part of the beach ecosystem [*Moreno et al.*, 2006]. Biological processes that take place in the swash zone are affected by morphodynamic (physical) processes. For example, the horseshoe crab (Limulus polyphemus) buries its eggs in the top 0.20 m of the sediment bed in the swash zone, and some eggs are lost due to exhumation by wave-induced sediment transport [*Jackson et al.*, 2014].

Despite their recognized importance, a thorough understanding of swash zone processes is still lacking. The main reason for this is that taking measurements in the swash zone is difficult since swash flows are shallow, ephemeral and frequently laden with sediment and bubbles [*Puleo et al.*, 2014b]. Furthermore, rapid bed level fluctuations [*Puleo et al.*, 2014a] hinder the accurate positioning of sensors. Reviews of swash zone processes were given by *Elfrink and Baldock* [2002], *Longo et al.* [2002], *Puleo and Masselink* [2006], and *Bakhtyar* [2009a]. In the years since these reviews have been published, research has continued in the form of laboratory [*Masselink et al.*, in preparation; *Barnes et al.*, 2009; *Sou et al.*, 2010; *O'Donoghue et al.*, 2010; *Alsina and Cáceres*, 2011; *Sou and Yeh*, 2011; *Alsina et al.*, 2012; *Astruc et*

al., 2012; *Cáceres and Alsina*, 2012; *Kikkert et al.*, 2012; *Othman et al.*, 2014], numerical [*Calantoni et al.*, 2006; *Hsu and Raubenheimer*, 2006; *Guard and Baldock*, 2007; *Puleo et al.*, 2007; *Zhang and Liu*, 2008; *Alsina et al.*, 2009; *Bakhtyar et al.*, 2009b, 2010; *Barnes and Baldock*, 2010; *Briganti et al.*, 2011; *Steenhauer et al.*, 2012; *van Rooijen et al.*, 2012; *Torres-Freyermuth et al.*, 2013; *Desombre et al.*, 2013] and field [*Aagaard and Hughes*, 2006; *Baldock and Hughes*, 2006; *Masselink and Russell*, 2006; *Turner et al.*, 2008; *Baldock et al.*, 2008; *Russell et al.*, 2009; *Masselink et al.*, 2009, 2010; *Puleo*, 2009; *Blenkinsopp et al.*, 2010a, 2011; *Austin et al.*, 2011; *Puleo et al.*, 2012, 2014b] studies.

In recognition of the fact that the swash zone poses a uniquely difficult measurement environment, many of these recent studies have presented innovative measurement techniques, including acoustic distance meters [*Turner et al.*, 2008], lidar [*Blenkinsopp et al.*, 2010a] and stereovision [*Astruc et al.*, 2012] to measure bed level change and free surface elevation, a shear plate to directly measure bed shear stress [*Barnes et al.*, 2009], a next-generation acoustic profiling velocimeter [*Puleo et al.*, 2012], and a new conductivity concentration profiler for sheet flow that is described in this work. Several laboratory studies were conducted in large wave flume facilities [*Masselink et al.*, in preparation; *Alsina and Cáceres*, 2011; *Alsina et al.*, 2012; *Astruc et al.*, 2012; *Cáceres and Alsina*, 2012]. In smaller flumes, dam breaks have become an increasingly popular alternative to conventional (paddle-type) wave makers for generating swash events since dam breaks can generate larger runup events [*Barnes et al.*, 2009; *O'Donoghue et al.*, 2010; *Kikkert et al.*, 2012; *Othman et al.*, 2014]. Dam breaks also generate repeatable swash events that are suitable for ensemble-averaging, e.g. to calculate turbulence characteristics [*Kikkert et al.*, 2012].

An important finding of swash-zone sediment transport measurements of the last two decades is that conventional sediment transport formulations such as the energetics-type formulation described by *Bagnold* [1966a], *Bowen* [1980] and *Bailard* [1981] or the *Meyer-Peter and Müller* [1948] equations, both of which relate the sediment transport to the flow velocity cubed, do not lead to satisfactory results when applied to the swash zone [*Hughes et al.*, 1997; *Masselink and Hughes*, 1998; *Puleo et al.*, 2000; *Nielsen*, 2002; *Butt et al.*, 2004, 2005; *Masselink et al.*, 2005; *Masselink and Russell*, 2006; *Othman et al.*, 2014]. Additional processes that are not included in the flow velocity cubed law significantly affect sediment processes, including sediment mobilization by pressure gradients [*Butt and Russell*, 1999; *Drake and Calantoni*, 2001; *Nielsen*, 2002; *Puleo et al.*, 2003; *Baldock and Hughes*, 2006; *Calantoni and Puleo*, 2006; *Othman et al.*, 2014], advected sediment and bore turbulence [*Puleo et al.*, 2000; *Butt et al.*, 2004; *Jackson et al.*, 2004; *Aagaard and Hughes*, 2006], swash-swash interactions [*Hughes and Moseley*, 2007] and groundwater in- and exfiltration [*Nielsen*, 1998; *Turner and Masselink*, 1998; *Butt et al.*, 2001; *Karambas*, 2003; *Masselink and Turner*, 2012; *Steenhauer et al.*, 2012]. It is still unclear, however, how these processes interact and ultimately determine the swash-zone sediment budget.

More recent field studies have challenged the long-standing notion that net sediment transport over an individual swash event is difficult to predict because net transport is a small signal that is the difference of two large signals, the uprush and backwash transport [*Osborne and Rooker*, 1999]. It is still agreed that uprush and backwash sediment transport are large, but recent measurements have shown that net sediment transport, and resulting bed level changes, over individual swash events are

not necessarily small. Event-scale bed level changes show significant variability and events with a bed level change of the same order as the net change over a tidal cycle frequently occur [*Masselink et al.*, 2009; *Russell et al.*, 2009; *Blenkinsopp et al.*, 2011; *Puleo et al.*, 2014a]. It may therefore be the case that the long-term net bed level change is driven by a slight shift in the distribution of event-by-event bed level changes [*Russell et al.*, 2009] or by 'large' swash events that are infrequent but cause large bed level changes [*Puleo et al.*, 2014a]. Predicting net sediment transport on the timescale of hours or longer using small-scale, process-based models may therefore be unsuccessful even if additional processes are included, since errors made by small-scale models will accumulate over time [*Masselink et al.*, 2009] .

Since the small water depths of swash flows limit the capacity for suspended load transport, the large sediment transport signals must be at least in part due to near-bed (bedload and sheet flow) sediment transport [*Masselink and Puleo*, 2006]. *Horn and Mason* [1994] deployed sediment traps on four different beaches and found that near-bed sediment transport was the dominant mode during the backwash phase, and that near-bed transport was also significant, and at certain locations dominant, during the uprush. In order to improve understanding of the swash zone sediment budget, it is therefore necessary to gain a better knowledge of sheet flow processes in the swash zone. Since sediment traps are only capable of measuring the time-integrated (bulk) sediment transport, other measurement techniques are needed to investigate the time-varying near-bed transport in greater detail.

1.2 Sheet Flow

Sheet flow is a form of intense near-bed transport of non-cohesive sediment, but the exact definition of 'sheet flow' is not universally agreed upon. A first

definition stems from measurements of sediment beds exposed to oscillatory flow in oscillatory flow tunnel experiments. Different regimes of bedforms are encountered as flow velocities increase. When the flow velocity exceeds a certain threshold, bedforms are washed out and the sediment bed becomes flat, with a dense layer of sediment moving over it [*Bagnold and Taylor*, 1946; *Dingler and Inman*, 1976]. In this sense, sheet flow is defined as 'near-bed sediment transport of such high intensity that bedforms are not present'. A second characteristic of sheet flow is that intergranular interactions are the dominant sediment mobilization mechanism (as opposed to turbulent suspension). A second definition of sheet flow is therefore 'a layer of mobilized sediment where intergranular interactions are the dominant mobilizing factor' [*Wilson*, 1987; *Hsu et al.*, 2004]. The difference in definition is important because the criterion for the onset of sheet flow may differ depending on the definition of sheet flow: a layer of sediment may be mobilized by intergranular interactions before bedforms are fully washed out, a situation that constitutes sheet flow under the second definition but not the first. Since bedforms are generally non-existent in the swash zone, the second definition (related to intergranular collisions) is used in this work. An interesting historical fact is that the sheet flow layer was referred to as a 'carpet' before the term 'sheet' was used [*Bagnold*, 1966a]. It is noted that the phrase sheet flow is also used in the context of rainfall runoff occurring as a thin film of water [*Julien and Simons*, 1985] but that process is not related to the sheet flow sediment transport process discussed in this work.

Sheet flow is sometimes referred to as a particular sub-type of bedload transport and sometimes seen as a transport mode separate from bedload. In this work, bedload and sheet flow sediment transport are regarded as two different

phenomena and the grouping of the two is referred to as near-bed sediment transport. Bedload is defined here as the process of individual grains rolling, sliding or saltating over the sediment bed without experiencing near-constant collisions with other mobilized grains (other than the bed). The bed load layer therefore has a thickness on the order of one grain diameter (although saltating grains might move higher above the bed). In contrast, sheet flow consists of a layer of mobilized sediment with a thickness of many [O(10-100)] grain diameters that are in constant collision and interaction, so that the sheet flow layer becomes a section of the flow with its own rheology [*Armanini et al.*, 2005]. It is clear that there are cases where the near-bed transport is purely bedload (e.g. a cobble-bed stream where the critical shear stress for sediment mobilization is only occasionally exceeded) or sheet flow (e.g. sheet flow with a thickness of over 10 mm over a sand bed, as frequently occurs in the swash zone, see Figure 4.1) but there are also cases that are intermediate between bedload and sheet flow.

The onset of sheet flow is typically defined using the Shields number θ [*Shields*, 1936]:

$$\theta = \frac{\tau_b}{\rho_f (s-1) g d} \tag{1.1}$$

where τ_b is the bed shear stress, ρ_f is the clear-water fluid density, $s = \rho_s/\rho_f$ is the relative density of the sediment, ρ_s is the density of the sediment, g is gravitational acceleration and d is a characteristic grain diameter (typically, d_{50}, the median grain diameter). The bed shear stress is generally quantified using a quadratic drag law and an empirical friction coefficient. Sheet flow is typically said to occur when θ exceeds a threshold value of 1.0 [*Nielsen*, 1992] although lower threshold values have also been proposed, particularly for smooth spherical particles [*Horikawa et al.*, 1982;

Asano, 1995]. The sediment mobility number ψ is also used to describe the onset of sheet flow sediment transport:

$$\psi = \frac{u_\infty^2}{(s-1)gd} \tag{1.2}$$

where u_∞ is the fluid velocity outside the boundary layer [*Asano*, 1995; *Dingler and Inman*, 1976; *Horikawa et al.*, 1982]. This formulation has the advantage that u_∞ is typically easier to quantify than τ_b and alleviates the need for an empirical friction coefficient. Dingler and Inman [*Dingler and Inman*, 1976] state that sheet flow occurs for $\psi > 240$. An estimate of the dimensionless thickness of the sheet flow layer under stationary flow is

$$\frac{\delta_s}{d} = 10\theta \tag{1.3}$$

where δ_s is the sheet flow layer thickness [*Wilson*, 1987]. The transition in sediment concentration from a packed bed at the bottom boundary of the sheet flow to dilute conditions at the top boundary has previously been described as approximately linear [*Wilson*, 1987; *Sumer et al.*, 1996; *Pugh and Wilson*, 1999].

Sheet flow is frequently observed in coastal settings, e.g. on the crests of sandbars [*Nielsen*, 1992; *Hassan and Ribberink*, 2005] and in the swash zone [*Hughes et al.*, 1997; *Masselink and Puleo*, 2006]. Sheet flow has also reportedly been observed in rivers during flood stage [*Wang and Yu*, 2007]. However, care must again be taken regarding the terminology. For example, it is uncertain whether the 'bed load sheets' (maximum Shields number $\theta = 0.3$) reported by *Dinehart et al.* [1992], constituted sheet flow. Sediment concentrations [O(1 kg/l)] in the sheet flow layer exceed maximum concentrations suspended higher in the water column [O(0.1 kg/l)] [*Beach and Sternberg*, 1988, 1991; *Puleo et al.*, 2000; *Butt et al.*, 2004; *Masselink et al.*, 2005]) by an order of magnitude, resulting in large sediment transport rates.

The first measurements of unidirectional sheet flow were conducted in annular, parallel-plate shear cells and provided constitutive relationships for the grain stresses that are the mobilizing mechanism for sheet flow [*Bagnold*, 1954; *Savage and Mckeown*, 1983; *Hanes and Inman*, 1985]. Experiments in recirculating flow tunnels [*Shook et al.*, 1982; *Sumer et al.*, 1996; *Pugh and Wilson*, 1999] provided additional insights into the velocity and sediment concentration profiles in the sheet flow layer and the increased bed roughness due to sheet flow. Sheet flow measurements under sinusoidal, asymmetric and irregular forcing were conducted in oscillatory flow tunnels [*Horikawa et al.*, 1982; *Ribberink and Al-Salem*, 1995; *Dibajnia and Watanabe*, 1998; *Dohmen-Janssen et al.*, 2001; *Ahmed and Sato*, 2003; *O'Donoghue and Wright*, 2004b; *Ribberink et al.*, 2008; *van der A et al.*, 2010; *Capart and Fraccarollo*, 2011; *Ruessink et al.*, 2011; *Dong et al.*, 2013]. These studies have established thresholds for the transition between the ripple regime and the sheet flow regime, and have provided the most detailed sediment concentration and velocity profiles in the sheet flow layer to date. Oscillatory flow tunnel studies also elucidated the relationship between velocity and acceleration asymmetry, phase lags between the free-stream velocity, bed shear stress and mobilized sediment, and the net sediment flux.

Studies in large-scale wave flumes provide a more realistic reproduction of the coastal environment and add the effects of free surface flow such as boundary layer streaming, which alters the net transport rate [*Dohmen-Janssen and Hanes*, 2002, 2005; *Schretlen et al.*, 2010]. Numerical models yield additional insights into the sheet flow process, but require validation by physical experiments [*Hsu et al.*, 2004; *Calantoni and Puleo*, 2006; *Amoudry et al.*, 2008; *Bakhtyar et al.*, 2009c; *Yu et al.*,

2010; *Chen et al.*, 2011]. Measurements of sheet flow under natural conditions have been scarce, mainly due to the difficulty of capturing the sheet flow layer near the sediment bed. *Bakker et al.* [1988] and *Yu et al.* [1990] provided the only known field measurements in the swash-zone sheet flow layer before this work, in contrast with the large number of swash-zone field studies that focused on suspended load [e.g., *Butt and Russell*, 1999; *Osborne and Rooker*, 1999; *Puleo et al.*, 2000; *Masselink et al.*, 2005; *Hughes et al.*, 2007; *Cáceres and Alsina*, 2012].

To summarize, sheet flow has been a crucial unknown in the study of swash-zone sediment transport. Numerical and laboratory studies have improved the understanding of the physics of sheet flow. The missing link is to obtain measurements of sheet flow in the swash zone under natural conditions but this requires a custom-designed measurement solution because existing sheet flow measurement techniques (discussed in Section 2.1) cannot be readily deployed in the field. The design of such a custom measurement solution, the Conductivity Concentration Profiler (CCP), is discussed in the following chapter.

Chapter 2

THE CONDUCTIVITY CONCENTRATION PROFILER

2.1 Introduction

The previous chapter described how sheet flow is an important sediment transport mode in the swash zone and measurements of sheet flow under realistic conditions are necessary to fully understand swash-zone sediment fluxes [*Masselink and Puleo*, 2006]. However, no instrument has been available that is capable of obtaining measurements of either velocity or sediment concentration in the sheet flow layer under field or large-scale laboratory conditions in the swash zone. This chapter describes the development of the Conductivity Concentration Profiler (CCP), which was developed specifically to measure sediment concentrations in the swash-zone sheet flow layer under field conditions.

Obtaining measurements of sediment concentration and/or velocity in the sheet flow layer is difficult, especially in field conditions, due to the small thickness of the sheet flow layer, large sediment concentrations, and the intermittent occurrence of sheet flow. Measurements are further complicated by rapid bed level fluctuations with amplitudes larger than the sheet flow layer thickness [*Puleo et al.*, 2014a] and by sharp concentration gradients where the sediment volume fraction may change by roughly 50 % over vertical distances on the order of 10 mm in a typical sheet flow layer. These gradients indicate the level of detail needed in sheet flow measurements where the vertical profile of both sediment concentration and velocity must be measured down to the stationary bed level to compute instantaneous sediment

transport rates. *Shook et al.* [1982] and *Pugh and Wilson* [1999] determined vertical sediment concentration profiles in pipelines under steady, unidirectional flow using the absorption of gamma rays and found a linear vertical concentration profile through most of the sheet flow layer and an exponentially decaying low-concentration tail in the upper portion of the sheet. The sheet thickness was proportional to the bed shear stress for a wide range of Shields numbers ($1 \leq \theta \leq 15$). Similarly, *Montreuil and Long* [2009] measured bedload transport using CT-scanning, and found that the bed porosity affects bedload transport quantities. Imaging techniques through a laboratory flume side-wall were performed by *Capart et al.* [2002] using Voronoï diagrams and by *Spinewine et al.* [2011] using the reflection of a laser sheet. Good agreement was found between the bulk sediment transport rates as measured by weighing the solids discharge at the flume outlet, and the transport rates obtained by vertically integrating the measured concentration and velocity profiles. However, the agreement was poorer for large transport rates due to wall effects in the measurement technique.

The methods described previously can only be used in scaled laboratory settings. To the author's knowledge, the only known method for quantifying sheet flow sediment concentration in prototype-scale wave flumes and natural coastal settings is to use electrical conductivity as a proxy for sediment concentration, a technique that was first used by *Horikawa et al.* [1982]. More recently, a conductivity concentration meter (CCM) developed by *Ribberink and Al-Salem* [1992] was used in a number of studies [*Bakker et al.*, 1988; *Dohmen-Janssen and Hanes*, 2002, 2005; *McLean et al.*, 2001; *O'Donoghue and Wright*, 2004a; *Ribberink et al.*, 2000; *Ribberink and Al-Salem*, 1995; *Sánchez-Arcilla et al.*, 2011; *Yu et al.*, 1990; *Hassan and Ribberink*, 2005; *Van der Zanden et al.*, 2013]. The CCM returns only a point

measurement, which is insufficient to instantaneously determine the vertical concentration profile in the sheet layer. *Bakker et al.* [1988] and *Yu et al.* [1990] partially circumvented this problem by simultaneously deploying three instruments with a known vertical offset. *O'Donoghue and Wright* [2004a] conducted experiments in an oscillatory flow tunnel with a single CCM, executing the same experiment multiple times with the CCM positioned at different elevations in order to re-create the vertical concentration profile. However, this approach is not possible in field settings or in laboratory settings with irregular wave trains. *Ribberink et al.* [2000] developed a remote-controlled "CCM tank" which allowed two CCM instruments to be repositioned in the vertical with sub-millimeter accuracy, enabling a more accurate repositioning of the sensor but experiments still had to be carried out multiple times in order to obtain a concentration profile [*McLean et al.*, 2001; *Dohmen-Janssen and Hanes*, 2002, 2005]. The two sensors in the CCM tank were positioned at the same vertical elevation with an offset in the streamwise direction, allowing the estimation of granular velocity using cross-correlation of the concentration signal [*McLean et al.*, 2001]. The CCM tank was recently improved with CCM probes that move up and down to follow a certain sediment concentration value using a real-time control system [*Van der Zanden et al.*, 2013]. *Dick and Sleath* [1991, 1992] developed a different configuration of conductivity measurements by using fifteen point electrodes mounted flush with the flume side-wall, all measuring with reference to a large common electrode. This geometry led to a sediment concentration profile and a smaller measurement volume compared to the four-electrode conductivity measurement technique used by the CCM since the measured resistance was solely determined by the volume around the small electrode as opposed

to the volume between the four electrodes. Also, it caused no flow interference since no object was placed in the flow. Wall effects, on the other hand, may have influenced concentration measurements and the concentration profile was relatively coarse since electrodes could not be placed near each other. *Zala Flores and Sleath* [1998] modified this concept by using pairs of electrodes flush with the flume side-wall spaced 10 mm apart in the horizontal to reduce radio interference. It is noted that the previous studies, with the exception of *Bakker et al.* [1988] and *Yu et al.* [1990], were all conducted in laboratory settings.

To achieve the goal of measuring the sediment concentration profile in the sheet flow layer under non-repeatable wave conditions in prototype-scale laboratory or field studies, an in-situ multi-point sensor is needed. A first prototype of a conductivity concentration profiler (CCP) was developed at the University of Delaware by *Puleo et al.* [2010] and used a two-electrode approach for conductivity measurement. The conductivity probe of this sensor, however, was relatively large, causing flow disturbance and unacceptable scour. Furthermore, the two-electrode approach and the associated circuitry returned accurate results in fresh water but not in salt water owing to higher conductivity. A second version of the CCP was developed by *Lanckriet et al.* [2013] from the ground up based on the lessons learned from the first prototype.

2.2 Sensor Design

The CCP consists of an internal electronic circuit contained within a PVC housing with an outer diameter of 48.3 mm and a detachable external conductivity probe (Figure 2.1). The total length of the sensor is 450 mm. The conductivity probe consists of a 6-layer FR-4 (woven fiberglass with an epoxy binder) printed circuit

board with dimensions 292.2 mm (length), 5.6 mm (width) and 1.6 mm (thickness). Two single arrays of 32 electrode plates spaced 1 mm in the vertical are located on both sides of the probe stem near the tip with dimensions 0.5 mm height and 3.1 mm width (Figure 2.1 inset). Electrode plates are coated with 76 nm of immersion gold for chemical passivation and abrasion resistance. The electrode plates on both sides of the probe at each elevation are internally connected so that each measurement is performed on the two sides of the probe reducing potential bias from probe deployments slightly oblique to the dominant flow direction. The PVC housing and probe stem are buried in the sand bed during deployment such that only a small section of the probe is proud of the sand-water interface. Video observations under laboratory and natural conditions have shown that the small cross-section of the exposed probe generates little flow disturbance for flows parallel to and slightly oblique to the sensor orientation. The electrode plates where conductivity measurements occur are located 131.7 mm above the PVC housing (Figure 2.1) so that the housing itself does not cause interference.

Abrasion by sand particles under wave action can damage the surface of the electrode plates, reducing the reliability of the signal. Therefore, the conductivity probe was designed as easily replaceable and expendable. The connection of the internal circuitry to the probe is implemented by inserting the bottom end of the conductivity probe into a PCI Express x1 edge connector on the internal electronic circuit board. Water tight conditions are maintained using a PVC collar around the probe neck just above the connector that is secured in place with an IP68 cable gland. During the BeST field study, the probes were replaced after being exposed to active sediment transport conditions spanning one high tide cycle.

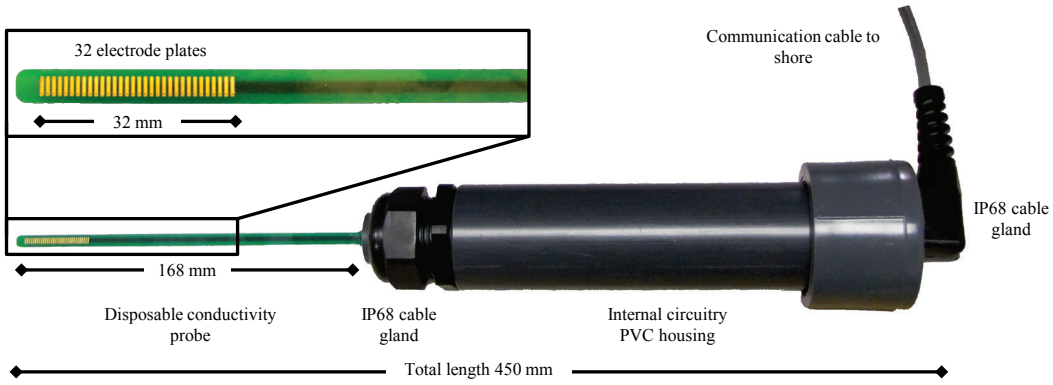

Figure 2.1: The CCP sensor. Inset: the 32 gold-plated electrodes used for the conductivity measurements.

The CCP electronic components are comprised of a microcontroller, serial data transceivers, conductance measurement circuit, and electrode selection multiplexers (Figure 2.2). Each conductivity measurement is performed using four neighboring electrode plates on the probe, named Force^{+}, Sense^{+}, Sense^{-} and Force^{-} respectively. The conductance-measurement process is initiated with the plate drive control circuit producing a plate drive voltage suiting the conductivity of the medium that may range from fresh water in laboratory settings to saline water in natural environments. The analog multiplexers then connect the four electrode plates to the conductance-measurement circuit and a measurement is taken using a 10 bit analog-to-digital (A/D) converter on the microcontroller. After the conductance measurement is completed, the multiplexers connect the next four electrodes to the measurement circuit and the measurement cycle is repeated. A profile of 29 conductivity measurements is generated by multiplexing through the array of 32 electrodes.

The conductance measurement circuit (Figure 2.3) is similar to *Li and Meijer* [2005] and consists of a pair of op-amps (U10a, U10b) that drive the outer force

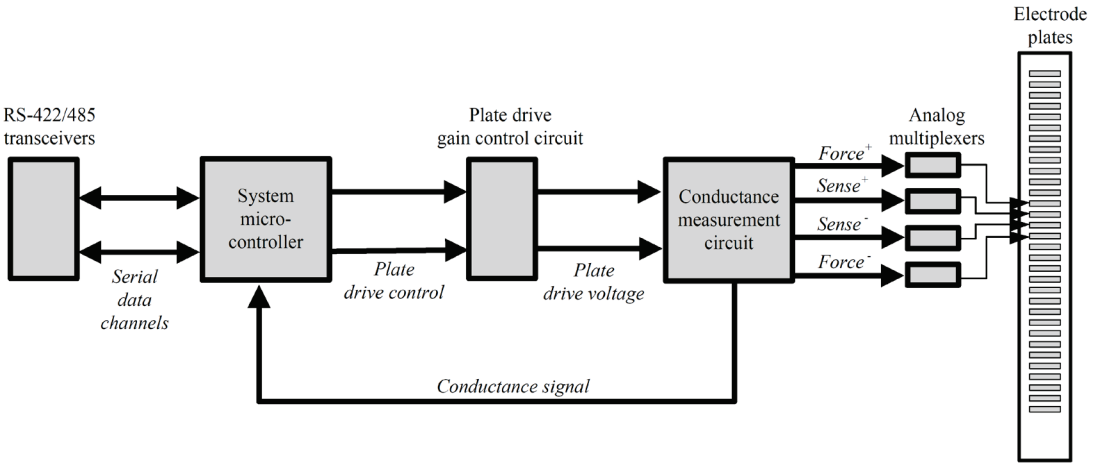

Figure 2.2: Schematic of the CCP measurement procedure.

electrodes ($Force^+$, $Force^-$) with sufficient voltage to cause the inner sense electrodes ($Sense^+$, $Sense^-$) to experience a voltage equal to the drive voltage ($Drive^+$, $Drive^-$). Electric current flowing as a result of the drive signal is detected as a voltage difference across the resistors R25 and R35 by instrumentation amplifiers U8a and U8b and summed by op-amp U11 to produce the detected conductance signal V_{sense}. The polarity of current detection is opposite between the U8a and U8b channels so spurious signals induced into both channels cancel when summed together to improve noise immunity. Low-pass filtering in the form of R4 + C10 and R3 + C4 assists in rejection of higher-frequency noise created by other instruments operating in the water nearby. The output V_{sense}, the conductivity signal related to sediment concentration (see section III.A), is connected to the A/D converter input on the microcontroller.

The actual measurement process is more complex than the preceding description due to baseline shifts in the detected conductance resulting from the use of probe board electrodes for both driving current and sensing voltage during the

multiplexing cycle. The forcing current through the electrodes builds up an electrochemical potential that would corrupt subsequent measurements using those same surfaces and must be neutralized by a reverse current flow. The microcontroller samples the detected conductance at four different times during each measurement cycle and calculates the baseline shift rate, removing it from the reported conductance to resolve this problem.

The calculated error is then fed into a proportional-integral digital controller, the output of which determines the polarity and duration of the compensatory reverse current used to remove the electrochemical potential from the electrodes. The duration of the measurement and potential-removal cycle is dependent on the error

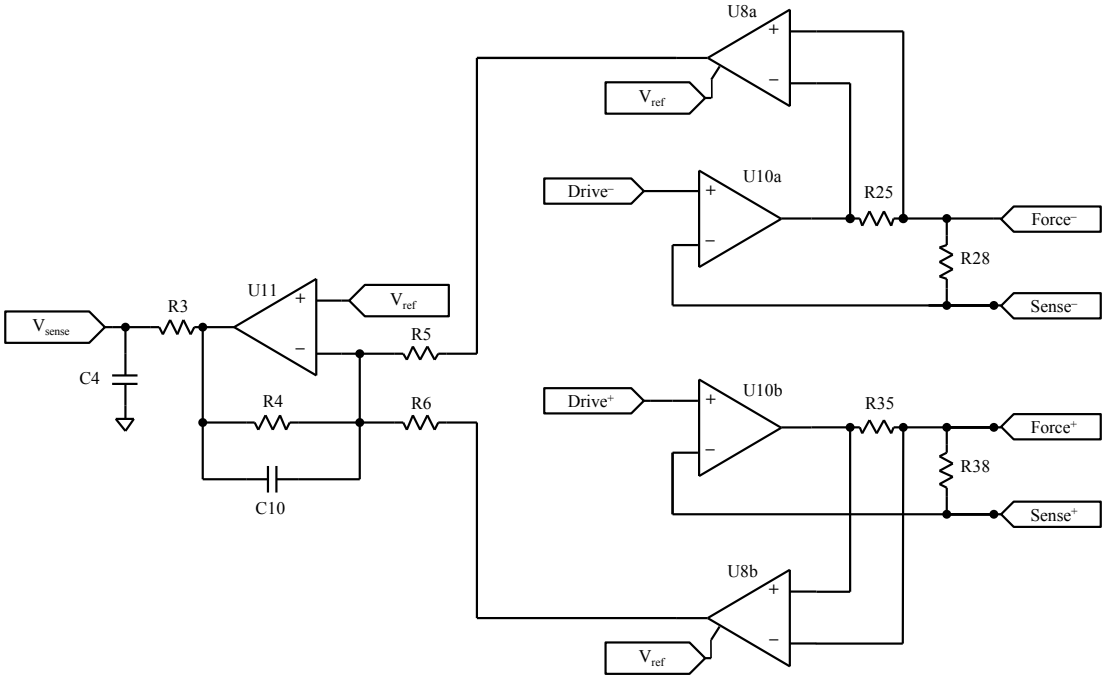

Figure 2.3: Circuit diagram of the CCP analog conductance measurement unit.

compensation by the proportional-integral controller and limits the fastest sampling rate of the current sensor configuration to 8 Hz.

Measured sensor output is transmitted in real time to a shore-based computer through a pair of RS-422 / RS-485 transceivers connected to a waterproof direct-burial Ethernet cable passing through the IP68 cable gland at the base of the housing (Figure 2.1). System operational parameters such as sampling rate, drive voltage, and digital controller coefficients can be adjusted through the shore-based computer prior to installation or on-the-fly during a deployment to ensure correct and stable operation.

2.3 Sensor Calibration and Measurement Characteristics

2.3.1 Calibration

2.3.1.1 Existing Relationships between Concentration and Conductivity

The rationale behind using conductivity as a proxy for sediment concentration is that both fresh and saline water have a high electric conductivity, while non-cohesive sediment grains are essentially non-conductive. The conductivity of any sediment-water mixture is thus a function of the volume fractions of the two phases, and it is expected that this effect is most significant when the sediment phase occupies a significant fraction of the measurement volume. The CCP was calibrated by measuring the conductivity of sediment-water mixtures with a known sediment concentration. Generating mixtures with high sediment concentrations of up to the packed bed limit, which typically have a solids fraction of 0.6-0.65, is difficult, except for the limiting cases of no sediment (zero volume fraction) and the packed sand bed itself. Previous efforts made measurements using a set of known sediment concentrations, either by adding a known mass of sediment to a vessel filled with a

liquid or by taking suction samples at the same location as the conductivity sensor [*Horikawa et al.*, 1982; *Bakker et al.*, 1988; *Dick*, 1989; *Ribberink and Al-Salem*, 1992; *Puleo et al.*, 2010]. Sediment suspension consisted of volume fractions less than 0.4 leaving a gap in the calibration curve for higher volume fractions. In addition, ensuring the homogeneity of the sediment suspension at these high volume fractions is difficult.

The previous studies, with the exception of *Dick* [1989], assumed a linear relationship between sediment volume fraction and conductivity of the form:

$$\mathrm{c} = \mathrm{k}\,(1 - \sigma_\mathrm{m}/\sigma_\mathrm{f}\,) \tag{2.4}$$

where c is the volume fraction of sediment, σ_m is the conductivity of the mixture, σ_f is the conductivity of the fluid and k is a calibration constant. The formulation (2.4) can be obtained from the theoretical development by *Landauer* [1952] for binary metallic mixtures where there is no correlation between the positions of the two phases, in the limiting case of zero conductivity for one of the two media

$$\sigma_\mathrm{m}/\sigma_\mathrm{f}\ = 1 - 3/2\ \mathrm{c} \tag{2.5}$$

by substituting the theoretical factor 2/3 by the calibration constant k [*Dick*, 1989]. Another commonly used formula for the conductivity of porous media is Archie's law [*Archie*, 1942]:

$$1/F = \sigma_\mathrm{m}/\sigma_\mathrm{f}\ = \phi^\mathrm{m} = (1 - \mathrm{c})^\mathrm{m} \tag{2.6}$$

where F is the formation factor, $\phi = (1 - c)$ is the porosity of the medium and m is a calibration factor.

The theoretical Bruggeman equation [*Bruggeman*, 1935] for insulating spheres of mixed sizes in a conductive medium is identical to Archie's law with $m = 1.5$. *De*

La Rue and Tobias [1959] measured the conductivity for glass spheres and sand in a zinc bromide suspension and found that Archie's law gave a good fit with $1.43 \leq m \leq 1.58$ (correlation coefficient squared, $r^2 > 0.998$), while *Archie* [1942] found $m = 1.3$ for clean sands. Similar results were found in additional numerical and experimental studies [*Lemaitre et al.*, 1988; *Küuntz et al.*, 2000]. *Jackson et al.* [1978] found that m depends on the grain shape, with $m = 1.2$ for spheres, $m = 1.85$ for shell fragments and $m = 1.39$-1.58 for marine sands. In summary, past theoretical and experimental work suggests $1.3 < m < 1.58$ for sands.

2.3.1.2 Experiments for CCP Calibration

Experiments were carried out with two natural sand samples: a fine silica sand (S1; $d_{50} = 0.12$ mm, $d_{16} = 0.08$ mm, $d_{84} = 0.17$ mm) and a coarse sand (S2; $d_{50} = 0.44$ mm, $d_{16} = 0.25$ mm, $d_{84} = 0.72$ mm), where d_n is the grain size for which n % is finer. The densities of the sand samples were 2.64 kg/m^3 for S1 and 2.63 kg/m^3 for S2. The calibration experiment was carried out using an aqueous solution of Lithium Metatungstate (LMT), a liquid with a nominal density of 2.95 kg/m^3. LMT was diluted using water to attain a density of 2.65 kg/m^3, creating a liquid in which the sand was approximately neutrally buoyant. The diluted LMT allowed sand-liquid mixtures with a known, homogeneous sediment concentration from zero to approximately 0.5 to be generated. For concentrations above 0.5 the mixture resembled a loosely packed sand bed and became increasingly heterogeneous, rendering measurements unreliable. The calibration experiments undertaken are similar to those by *De La Rue and Tobias* [1959] who used zinc bromide as the suspension liquid.

A set of 29 known masses of S1 sand (24 for S2) were individually added to the liquid and manually stirred with a glass stirring rod creating nominal concentrations ranging from 0 to 0.51 volume fraction (0 g/L to 1353 g/L) for S1, and 0 to 0.42 (0 g/L to 1161 g/L) for S2. Conductivity measurements using the CCP sensor were recorded at 4 Hz for 25 s for each concentration, yielding 100 samples. The mixture temperature was also recorded throughout the experiment using a mercury thermometer and was 22 +/- 0.5 °C. Only the inner 19 locations in the vertical concentration profile were retained to avoid edge effects from the probe being too close to either the free surface or the bottom of the vessel, leaving a total of 1900 conductivity estimates for each concentration. The 1900 data points were averaged to find a representative conductivity measurement for each sediment concentration and the standard deviation of the 1900 samples was calculated to provide an estimate of the temporal and spatial variability of the conductivity in the sample. For the fine sand S1, the grains were neutrally buoyant and the mixture appeared visually to be homogenous throughout the experiment. For the coarser sand S2, particles were observed to be slightly positively buoyant as the liquid density could not be matched exactly with the specific density of the sand. To alleviate this issue, only the first 5 s of each conductivity measurement for S2 were used to obtain a conductivity value, while still using the inner 19 measurement points in the vertical profile, leading to 380 data points used for each representative conductivity measurement as opposed to 1900. The buoyancy effect was most significant for small sediment concentrations, as the vertical rising of the grains was slowed down significantly due to hindered rising or increased viscosity of the slurry at higher sediment concentrations. No significant vertical motion of the grains was observed for sediment concentrations higher than

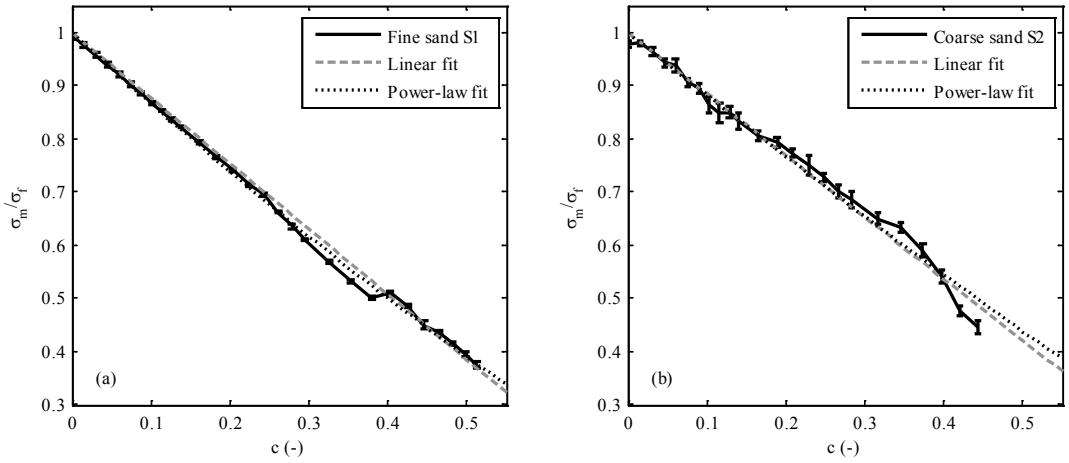

Figure 2.4: Conductivity calibration for fine sand S1 (a) and coarse sand S2 (b). Vertical bars represent 1 standard deviation on either side of the mean of the 1900 (a) or 380 (b) samples used for each of the representative conductivity measurements. The gray and black dashed lines are least squares fits using the linear law (2.4) and power law (2.6) respectively.

0.27. The CCP measurements indicate an obvious decreasing trend in conductivity as a function of sediment concentration for both the fine sand (Figure 2.4a) and coarse sand (Figure 2.4b). The small variability, indicated by the vertical bars at each concentration in Figure 2.4, signifies the homogeneity of the mixtures. No obvious trend in temporal variability was found in the time series of individual sensor

Table 2.1: Results of calibration experiments.

		Fine sand (S1)	Coarse sand (S2)
	d_{50} (mm)	0.12	0.44
Linear law (2.4)	k	0.81	0.86
	r^2	0.997	0.987
Power law (2.6)	m	1.36	1.19
	r^2	0.998	0.985

channels. Measurements show excellent correlation to both a linear relationship [equation (2.4)] and a power-law relationship [equation (2.6)], determined using a least-squares fit. The power law calibration constants *m* are 1.36 for S1 and 1.19 for S2, near the range of values reported in the literature (Table 2.1)

2.3.2 Measurement Volume Quantification

2.3.2.1 Theory

CCP measurements are influenced by the size of the measurement volume, which is mostly determined by the electric field emitted by the electrodes. Four electrodes are used for each conductivity point measurement. Due to the finite size of the rectangular electrode plates (Figure 2.1 inset), the voltage field around the probe is three dimensional and cannot be approximated by an analytic expression based on point electrodes. Instead, a finite differences model was used to study the voltage potential and current fields around the CCP probe, in an effort to estimate the horizontal extent of the measurement volume and the amount of smoothing that occurs when measuring a varying vertical conductivity profile.

During the design of the CCP sensor, oscilloscope measurements verified that the duration of each electric pulse emitted by the force electrodes is longer than the relaxation time of the surrounding environment to equilibrate to the forced voltages. Therefore, the electric field around the sensor can be calculated using the laws of stationary electromagnetism. The continuity equation for a stationary electric current is

$$\nabla \cdot \vec{J} = 0 \tag{2.7}$$

where $\vec{J}$ is the current density field. In a non-homogeneous medium $\vec{J}$ can be calculated as

$$\vec{J} = \sigma\vec{E} = -\sigma\nabla V \tag{2.8}$$

where $\vec{E}$ is the electric field, σ is the electric conductivity and V is the voltage potential. Combining (2.7) and (2.8) yields

$$\nabla \cdot (\sigma\nabla V) = 0 \tag{2.9}$$

Equation (2.9) reduces to the well-known Laplace equation for a homogeneous conductivity field. The following assumptions were made to model the current field:

1. The thickness of the CCP probe is negligible. As the probe has electrode plates on both sides that are internally connected, the entire geometry is symmetrical around the plane of the electrode plates.

2. To reduce computation time, individual sand grains were not resolved. Instead, the sand-water mixture was modeled as a single medium with a conductivity field that varies only on the scale of the sheet thickness as a function of the sediment concentration. Furthermore, the conductivity profile was assumed to vary only in the vertical direction: $\sigma = \sigma(z)$.

The axis orientation for the model is displayed in Figure 2.5a. Since the geometry is symmetrical around the *x*-*z* plane and the *y*-*z* plane, only 2 octants of the space around the probe were modeled and (2.9) was solved on a domain with 0 mm ≤ x ≤ 12.7 mm, 0 mm ≤ y ≤ 12.7 mm and -8.13 mm ≤ z ≤ 8.13 mm. Equations (2.4-6) are linear and only relative voltages are important. The Force$^+$ and Force$^-$ electrodes were modeled as boundary conditions with constant voltages of +1 V and -1 V respectively. Floating electrode plates such as the Sense$^+$ and Sense$^-$ electrodes and the nearby unused electrodes were additional model boundary conditions where the voltage on each floating electrode is constant since the electrode plates are far more conductive than the surrounding medium and there is no net current flux into the electrodes. The epoxy face of the probe was modeled as a no-flux boundary

condition. The outer edges of the domain were also modeled as no-flux boundary conditions and were far enough away from the active electrodes as to not influence the current field.

The voltage field $V(x,y,z)$ was discretized on a grid with a constant spacing $\Delta x, \Delta y, \Delta z$ and the conductivity field $\sigma(z)$ on a grid that is staggered by one half of the grid spacing in the z-direction, but collocated with the V grid in the x and y direction. Using Gauss-Seidel iteration with a stability criterion analogous to the classical Laplace equation, the solution was iterated as:

$$V_{i,j,k}^{new} = V_{i,j,k} + \omega \left\{ \frac{\sigma_{c,j}}{\sigma_{max}} \left(\frac{\Delta y^2 \Delta z^2}{2(\Delta x^2 \Delta y^2 + \Delta x^2 \Delta z^2 + \Delta y^2 \Delta z^2)} \left(V_{i-1,j,k} - 2V_{i,j,k} + V_{i+1,j,k} \right) + \frac{\Delta x^2 \Delta z^2}{2(\Delta x^2 \Delta y^2 + \Delta x^2 \Delta z^2 + \Delta y^2 \Delta z^2)} \left(V_{i,j-1,k} - 2V_{i,j,k} + V_{i,j+1,k} \right) \right) + \frac{\Delta x^2 \Delta y^2}{2(\Delta x^2 \Delta y^2 + \Delta x^2 \Delta z^2 + \Delta y^2 \Delta z^2)} \frac{\sigma_{s,j-1} V_{i,j,k-1} - (\sigma_{s,j-1} + \sigma_{s,j}) V_{i,j,k} + \sigma_{s,j} V_{i,j,k+1}}{\sigma_{max}} \right\} \quad (2.10)$$

where the index c stands for the collocated σ grid and s stands for staggered grid and $\omega = 1.3$ is an over-relaxation factor that accelerates convergence. The system was considered to have converged when

$$\epsilon = \frac{1}{\max(|V_{i,j,k}|)} \sum_{i,j,k} \left(V_{i,j,k}^{new} - V_{i,j,k} \right)^2 < 10^{-4} \quad (2.11)$$

and

$$\left| \left| \frac{I^+ - I^-}{I^-} \right| - 1 \right| < 0.05 \quad (2.12)$$

where ϵ is the relative error and I^+ and I^- are the magnitudes of the current through the Force$^+$ and Force$^-$ electrodes respectively and | | indicates magnitude. To further accelerate convergence, a multigrid approach was adopted where the model was solved subsequently on 6 increasingly finer grids (Table 2.2). The voltage field of the

Table 2.2: Grid spacings in the multigrid approach

Grid	Grid spacing	Nodes
Grid 0	$\Delta x = \Delta y = 1.046$ mm; $\Delta z = 0.508$ mm	6 468
Grid 1	$\Delta x = \Delta y = \Delta z = 0.508$ mm	22 308
Grid 2	$\Delta x = \Delta y = \Delta z = 0.254$ mm	171 666
Grid 3	$\Delta x = \Delta y = \Delta z = 0.169$ mm	560 272
Grid 4	$\Delta x = \Delta y = \Delta z = 0.127$ mm	1 326 130
Grid 5	$\Delta x = \Delta y = \Delta z = 0.102$ mm	2 556 036

next finer grid was initialized using a linear interpolation of the previous coarser grid. Grids 0 to 4 were only used to speed up the computation. Results from the finest grid, with spacing 0.102 mm in all directions, were used for subsequent analysis.

2.3.2.2 Lateral Extent of Current Field

When the CCP probe is deployed upright through the sand bottom, the lateral extent of the CCP measurement volume indicates how far away from the sensor the measurement is influenced in the plane normal to the stem of the probe. This is important for calculating the quantity of sand grains in the measurement volume. If the measurement volume only contained a small number of sand grains, the CCP would likely output a "binary signal": high conductivity when there is no sand present in the measurement volume, and low conductivity when a small number of sand grains are present. Additionally, the lateral extent of the measurement volume indicates how far a CCP sensor must be placed from any obstacles such as the side wall of a flume or other sensors, to avoid disturbing the conductivity measurement.

The electric field was calculated for a constant conductivity, σ, in the entire domain to determine the lateral extent of the measurement volume. The conductivity of the medium was set to 1 since the model equations (2.4-6) are linear and only relative currents were considered. Then the current density J_z oriented normal through the *x*-*y* plane was computed, half way between the Force$^+$ and Force$^-$ electrodes where

the lateral extent of the current field was the largest (Figure 2.5a). Figure 2.5b shows the J_z field normalized by the maximal current density in the plane. The current density decays away from the sensor with the bulk of the current occurring near the electrodes. The black curve in Figure 2.5 indicates where the current density has decayed to 1 % of its maximum value. By integrating the current density through the

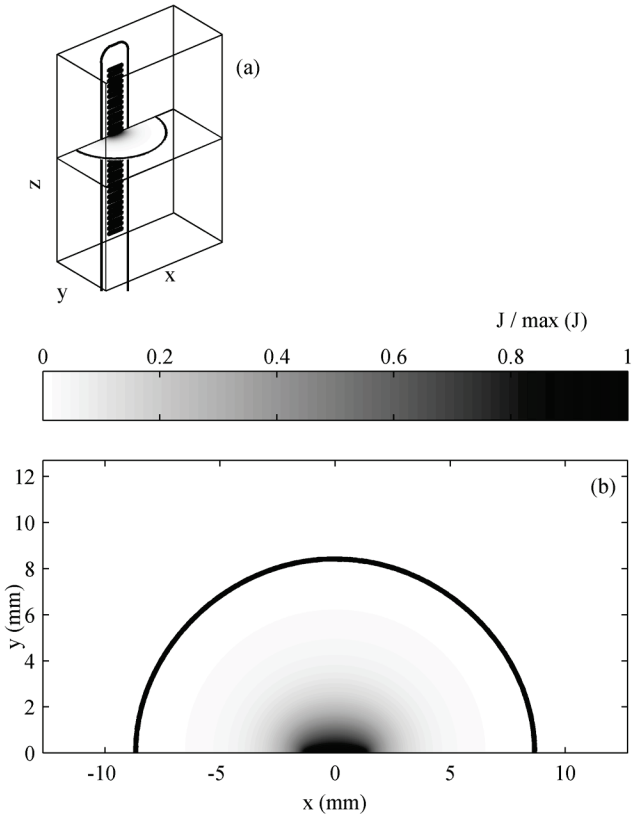

Figure 2.5: (a) Location of the *x-y* plane where the normalized current field is computed. (b) Normalized current field through *x-y* plane indicating lateral extent of the measurement volume. The black curve in (b) indicates where the current field is 1 % of its maximum value.

surface delineated by this 1 %-curve, 88 % of the total current passes through this surface. Therefore, the 1 %-curve is defined as the lateral extent of the measurement volume. The measurement volume extends from -8.7 mm $\leq x \leq$ 8.7 mm and -8.4 mm $\leq y \leq$ 8.4 mm. As the probe is 5.6 mm wide, the measurement volume extends approximately 1.5 probe widths away from the center line of the probe. However, this lateral extent of measurement volume estimate is conservative since most of the current flows much closer to the electrodes than the 1 % curve (Figure 2.5). The linearity of the model equations also means that the relative current density field, and thus the measurement volume, is independent of the absolute conductivity value. As a result, the measurement volume is identical for measurements in both high and low conductivity environments such as clear water and a packed sand bed.

2.3.2.3 Vertical Extent – Profile Smoothing

It is expected that measured sheet flow layer thicknesses will appear larger than the real sheet flow layer thickness through smoothing of the vertical concentration profile as a result of the finite extent of the measurement volume. The electric field was again simulated with the finite difference model, this time for a piecewise linear transition in concentration between a simulated "compacted sand" with a volumetric sediment concentration of 0.644 [*Bagnold*, 1966b], and "clear water" with a volumetric sediment concentration of 0. The piecewise linear concentration profile was chosen as a simplified, representative shape of the conductivity profile in the sheet layer, which may have an arbitrary shape. The corresponding conductivity field was computed using Archie's law (2.6) with m = 1.5. Since Archie's law yields an approximately linear relation between concentration

and conductivity, this corresponds to an approximately piecewise linear transition in the conductivity profile.

The conductivity profile was shifted vertically by increments of 0.5 mm through the computational domain and the virtual sensor output was calculated for each shift. Shifting the conductivity profile in the domain is equivalent to measuring a fixed conductivity profile with electrodes at different elevations, as would occur for actual CCP sensor measurements. Figure 2.6a shows an example conductivity profile with the thickness of the prescribed conductivity transition of 4.0 mm (dashed line).

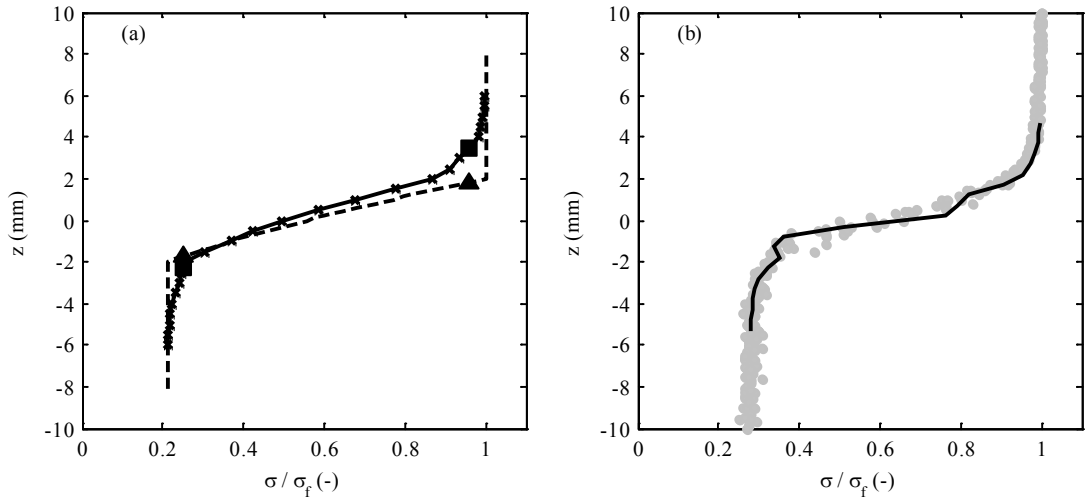

Figure 2.6: (a) Conductivity profile for a 4.0 mm prescribed conductivity transition. Dashed line is the prescribed conductivity profile of the medium; triangles indicate the 5 % and 95 % cutoff for the prescribed profile. The solid line is the simulated conductivity profile for the CCP; squares indicate the 5 % and 95 % cutoff for the simulated profile. (b) Comparison of simulated CCP results (solid black line) with experimental CCP measurements (gray dots) across a sand-water interface.

The profile as it would be measured by a simulated CCP sensor is smoothed (solid line) and the thickness of the transition layer is larger than the prescribed thickness.

Numerical simulations were validated using measurements across a sand-water interface. A CCP was placed in a vessel containing water. Coarse sand (S2) was added and allowed to settle under gravity until the sand-water interface was located at roughly the middle of the profiling region of the probe. Fifteen measurements were taken, each time raising the sensor by 0.2 mm between measurements using a manually-controlled stepper to analyze sensor smoothing at sub-millimeter resolution. Model simulations were performed with the conductivity in the fluid and in the sand bed equal to the measured values (Figure 2.6b). As it can be expected that the grain packing density near the top of the sand bed will be less than the packing deeper in the sand bed, the sand-water interface was modeled as a piecewise linear concentration profile in which the transition thickness from a fully packed bed to clear water was set to $2d_{50} = 0.88$ mm. The simulated CCP output was found to be relatively insensitive to this value due to its vertical smoothing. The shape of the simulated CCP measurements agrees well with the real measurements ($r^2 = 0.985$), illustrating the skill of the developed model (Figure 2.6b).

Similar simulations as in Figure 2.6a were conducted for conductivity transitions with varying prescribed thicknesses ranging from 0 mm to 14 mm. The top and bottom of the sheet flow layer were defined using a curve-fitting technique to find a 'shoulder' point in the concentration profile (indicative of the bottom of the sheet flow layer) that provided the best results for defining sheet flow layer thickness under field conditions (described in Section 4.3.1). For each simulated conductivity transition, the sheet flow layer thickness was determined using the curve-fitting

method for both the prescribed conductivity/concentration profile (before smoothing) and the conductivity/concentration profile as measured by the simulated CCP (including sensor smoothing). Sheet thicknesses determined after smoothing by a simulated CCP sensor (Figure 2.7, black line with triangles) and before smoothing (solid black line) co-vary but the profile smoothing causes an overprediction of simulated sheet thicknesses. For sheet thicknesses (not taking smoothing into account) of less than 5 mm (corresponding to an estimated sheet thickness of 5.5 mm including smoothing), the simulated sheet thickness is dominated by the smoothing effect and is insensitive to the prescribed sheet thickness. For sheet thicknesses exceeding 5 mm, the simulated CCP signal resembles the prescribed sheet thickness. A correction formula was developed that converts sheet thicknesses estimated from CCP measurements (including smoothing) to the correct sheet thicknesses:

$$\frac{\delta_{sens}}{\delta_{real}} = \frac{1}{713 \cdot 10^3 \delta_{sens}^2 - 6024\delta_{sens} + 21.9} + 1, \qquad (2.13)$$

with δ_{real} and δ_{sens} the real thickness and measured thickness by a CCP sensor, respectively, expressed in meters.

A conservative manner of interpreting sheet flow thicknesses from CCP laboratory or field experiments is to discard measurements with an uncorrected measured sheet thickness of less than 5.5 mm, which corresponds to a real sheet thickness of 5 mm according to the correction formula (2.13). Measurements with real sheet thicknesses of 5.0 mm or more (corresponding to uncorrected thicknesses of 5.5 mm or more) are reliable (see Discussion), and their actual thicknesses are corrected using (2.13). It is noted that the simulation displayed in Figure 2.6a is near the limit of reliable sheet thickness. This simulation is therefore near the worst case for the error in sheet thickness due to CCP smoothing.

Initial analysis of the sensor smoothing effect [*Lanckriet et al.*, 2013] defined the bottom of the sheet layer as the elevation where the conductivity exceeds the minimum conductivity plus 5 % of the difference in conductivity between the maximum and minimum conductivity, and the top of the smoothed transition layer as the elevation where the conductivity exceeds the minimum conductivity plus 95 % of this difference (Figure 2.6). Subtracting the 5 % level from the 95 % level then yields an alternate estimate of the measured sheet layer thickness (Figure 2.7, blue line). A

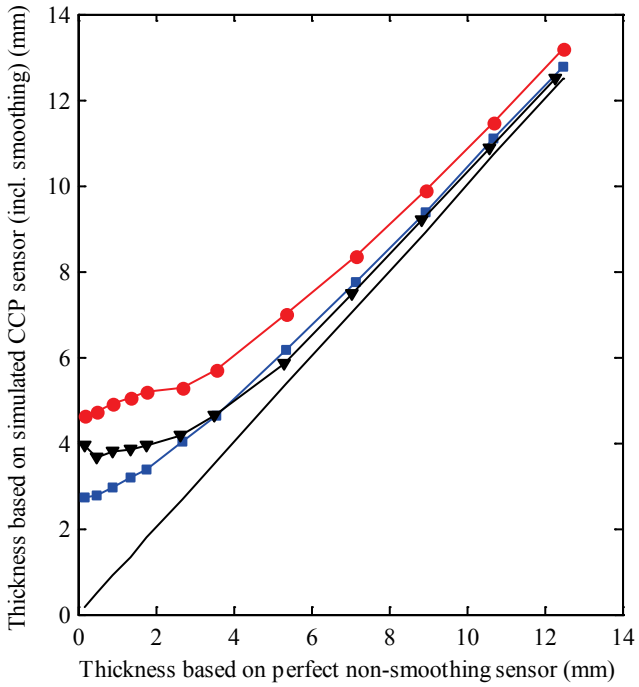

Figure 2.7: Sheet thickness as measured by a simulated CCP sensor compared to sheet flow layer thickness determined without sensor smoothing. Black line with triangles: sheet thickness determined using curve-fitting technique (Section 4.3.1). Red line with circles: sheet thickness determined via 5%-95% cutoff of conductivity profile. Blue line with squares: sheet thickness determined via 5%-95% cutoff of conductivity profile for miniaturized CCP sensor (Section 2.4.1). Black solid line is line of perfect agreement.

correction factor was also developed for this case and is mentioned here only for completeness:

$$\frac{\delta_{sens}}{\delta_{real}} = \frac{1}{127 \cdot 10^3 \delta_{sens}^2 - 94.1\delta_{sens} - 2.07} + 1 \tag{2.14}$$

Additionally, the sediment volume mobilized within the sheet flow layer, or volumetric sheet load, can be determined as

$$\Phi = \int_{z_e}^{z_t} c \, dz \tag{2.15}$$

where z_e and z_t are the elevation of the bottom and top of the sheet flow layer, respectively. The sediment mass mobilized in the sheet layer, or sheet load, is then defined as

$$\mathrm{C} = \rho_s \Phi, \tag{2.16}$$

where $\rho_s = 2650\ kg/m^3$ is the sediment mass density. A correction formula was also developed to correct the volumetric sheet load for the smoothing effect:

$$\frac{\Phi_{\mathrm{sens}}}{\Phi_{\mathrm{real}}} = \frac{1}{713 \cdot 10^3 \Phi_{sens}^2 - 6024\Phi_{sens} + 21.9} + 1 \tag{2.17}$$

where Φ_{real} and Φ_{sens} are the real volumetric sheet load and measured volumetric sheet load (including smoothing), respectively.

2.4 Discussion

2.4.1 Sensor Design

Several factors affected the design of the in situ probe, including the minimization of flow disturbance and scour around the probe, mechanical strength for field deployment, and an optimal size of the measurement volume. With cross section dimensions of only 1.6 mm x 5.6 mm, flow disturbance and bed scour was found to be minimal during initial testing in a wave flume and during deployments on a natural

beach for flow parallel to the sensor orientation. For flows oblique to the sensor, eddy shedding will occur causing flow disturbance behind the sensor meaning sensor orientation during deployment is critical. The mechanical strength of the probe, made of woven fiberglass with an epoxy binder, is considerable. Additionally the probe is supported through its burial in the sand bed with only the top 10 - 40 mm exposed. As a result, no probes have failed mechanically under wave action during the lab and field trials.

The optimal size of the measurement volume should be large enough to contain a sufficient number of sand grains in order to make a representative measurement of the sediment concentration, and small enough to minimize smoothing of the vertical concentration profile. The measurement volume can be approximated by an ellipsoid with semi-axes lengths x: 8.7 mm; y: 8.4 mm (as determined by the lateral extent of the measurement volume; section III.B.2); z: 3.5 mm (the smallest sheet thickness that is resolved by the sensor based on a 5% and 95% cutoff of the conductivity profile), giving a volume of 1071 mm^3. For volumetric concentrations between 0.08 to 0.51 and sand grains approximated as spheres with diameter of 0.33 mm (d_{50} of sand during the Beach Sand Transport experiment, Chapter 3), the measurement volume would contain $4.6 \cdot 10^3$ to $2.9 \cdot 10^4$ sand grains. This large number of sand grains is sufficient to provide a representative measurement of the sediment concentration. For comparison, an optical backscatter sensor (OBS) for suspended sediment concentration has a measurement volume of $1\text{-}20 \cdot 10^3$ mm^3 [*Downing*, 2006]. For volumetric sediment concentrations of 0.03 (100 g/L) in energetic surf zones, an order of magnitude smaller than the typical range of concentrations measured by the CCP, the OBS measurement volume contains $2 \cdot 10^3$ to

$4 \cdot 10^4$ sand grains, of the same order as the CCP measurement volume. In contrast, a fiber optic backscatter sensor (FOBS) has a measurement volume of only 25 mm^3, corresponding to 50 grains at a volumetric sediment concentration of 0.03. Thus, longer averaging times are needed to avoid noise at low concentrations when using a FOBS [*Downing*, 2006].

The vertical smoothing of the CCP measurements means the sensor cannot detect sheet flows less than 5 mm thick. A correction factor must be applied to analyze larger sheet thicknesses. Following the criterion of *Nielsen* [1992] for the onset of sheet flow ($\theta > 1.0$) and the estimate of sheet thickness under stationary flow [equation (1.3)], sand grains with $d_{50} = 0.35$ mm will form a sheet layer with thickness 3.5 mm at the onset of true sheet flow (absence of bed forms). Therefore, in flows where the hydrodynamic forcing exceeds the threshold for true sheet flow, the theory predicts a sheet flow layer with a thickness that can almost be resolved by the CCP. Near-bed sediment transport can also be dominated by granular interaction occurring at lower Shields numbers [*Horikawa et al.*, 1982]. Sheet layer thicknesses in these flows are not resolved by the CCP. Sheet thicknesses recorded during field observations (Section 4.2) routinely exceeded 10 mm during both uprush and backwash. At these thicknesses, the smoothing effect is small (Figure 2.7). In summary, the measurement volume of the CCP is large enough to contain a sufficient number of grains for a representative concentration measurement, and small enough to resolve sheet flow in most practical applications. Moreover, the detailed study of the smoothing effect using numerical simulations allows the user to address vertical smoothing using a correction factor, rather than assuming the inherent smoothing does not affect sheet thickness estimates.

Further miniaturizing the CCP probe could reduce the smoothing effect but this has to be weighed against increased manufacturing costs. As the sediment concentration in the sheet layer has a sharp gradient in the vertical but is approximately uniform in the horizontal, positioning the four electrodes needed for a conductivity measurement in a horizontal row would reduce the vertical extent of the measurement volume and thus the smoothing effect. On the other hand, each point measurement in the concentration profile would then require a separate row of four electrodes, increasing the number of electrodes and electrical routes in the probe by a factor of four. Measurement volume simulations were conducted for a probe believed to be near the limit of current manufacturing capabilities to estimate the maximum possible reduction of the measurement smoothing. The electrode plates on this idealized probe were modeled as squares with dimensions 0.5 mm (the width of the rectangular electrode plates on the current probe), placed in horizontal rows of four electrodes with a spacing of 1 mm. The vertical profile smoothing by this probe based on the 5% and 95% conductivity cutoff (blue line, Figure 2.7) would be smaller than the current probe and sheet thicknesses down to 1.5 mm could be resolved. An additional benefit of the horizontal lay-out is that electrodes would maintain their function as either Force or Sense electrodes during the multiplexing process using this lay-out, negating the build-up of electrochemical potential. As a result, the CCP could sample at higher frequencies without the need for an electrochemical potential removal step as described in section 2.2.

2.4.2 Sensor Calibration

A range of sediment volume fractions from 0 to 0.51 (0 to 0.44) was tested for fine sand S1 (coarse sand S2) during the calibration experiments. Over this range,

conductivity was reduced from the clear-water conductivity by a factor of 2.6 (2.2). Extrapolating this result using the power law [equation (2.6)], conductivity would be reduced by a factor 4.0 (3.1) if a measurement was made in a fully compacted bed with a volume fraction 0.644. This large reduction in conductivity and the correlation with calibration laws justify the use of conductivity as a measurement method for sediment concentration.

Many prior studies of sheet flow in coastal environments used a linear relationship between conductivity and sediment concentration [e.g., *Horikawa et al.*, 1982; *Bakker et al.*, 1988; *Ribberink and Al-Salem*, 1992; *McLean et al.*, 2001; *Dohmen-Janssen and Hanes*, 2002, 2005; *O'Donoghue and Wright*, 2004a]. Testing both the linear and power-law relationships in this study revealed that both are equally adept at describing the experimental data as determined by the square of the correlation coefficient. The assumptions underlying the theoretical *Bruggeman* [1935] equation, equivalent to the power law, are more suited to the case of sediment grains suspended in water than the assumptions underlying the derivation by *Landauer* [1952], equivalent to the linear law. In addition, there is more numerical and empirical evidence in the literature pointing toward a power-law relationship for the conductivity of sand-water mixtures [*Archie*, 1942; *De La Rue and Tobias*, 1959; *Jackson et al.*, 1978; *Lemaitre et al.*, 1988; *Küuntz et al.*, 2000]. Hence, a power-law relationship [equation (2.9)] is adopted as the method to calibrate the CCP sensor.

The calibration factor, m, for a power-law relationship between electrical conductivity and sediment concentration was found to be 1.36 and 1.19 for fine (S1) and coarse (S2) sediments respectively. The value for S1 falls within the range of those reported in previous studies (m = 1.3 - 1.6) while the value for S2 falls slightly

outside this range. A possible cause for the smaller m value for coarse sand is that the sand-liquid mixture may not have been perfectly homogenous. Additionally, fines were removed from the S2 sand sample using a woven polyester mesh with 0.025 mm opening size during a previous study. The lack of fines in the sand-liquid mixture may have altered the pore structure and the conductivity response. Nevertheless, CCP sensor data show a strong response to the sediment concentration for both samples and the calibration laws describe measurements accurately ($r^2 > 0.98$). Less guidance exists in the literature on the value of the calibration coefficient k in a linear fit model. *Ribberink and Al-Salem* [1992] obtained a value $k = 1.16$ for sand with $d_{50} = 0.21$ mm (median grain diameter between S1 and S2 in the present study), larger than the values found here ($k = 0.81$ and 0.86 for S1 and S2 respectively). Fitting a power law through the linear relationship used by *Ribberink and Al-Salem* [1992] yielded $m = 0.83$, in contrast with existing literature for the power-law relationship. A possible explanation is that the calibration by *Ribberink and Al-Salem* [1992] may have been influenced by their conductivity measurements in a non-moving sand bed, where a small error in the measured porosity values may have led to large differences in the calibration coefficient. *Dick* [1989] obtained $k = 1.0$ for acrylic particles with $d_{50} = 0.5$ mm and $\rho = 1.141$ kg/m3, in between the value obtained by *Ribberink and Al-Salem* [1992] and the values obtained in the present study. Their calibration value may have been affected by the shape of the acrylic particles which influences the calibration coefficient [*Jackson et al.*, 1978].

Laboratory calibration measurements were continued until approximately the loosely packed bed limit with a volume fraction of roughly 0.5. For higher sediment concentrations, the sediment-water mixture could no longer be kept homogeneous. In

practical situations, however, the CCP is used to make concentration measurements up to the packed bed limit with a volume fraction of 0.644. Since Archie's law has also been validated for consolidated sandstone materials with solids volume fractions of 0.7 – 0.9 [*Archie*, 1942; *Adler et al.*, 1992], it may be assumed that the calibration laws can be extrapolated to the bed packed limit.

To perform a sensor calibration in a practical case such as a field study, two coefficients in equation (2.6) need to be determined: the calibration factor m, which describes the reduction in conductivity by the presence of sediment, and the fluid conductivity σ_f. The factor m is solely determined by sediment characteristics such as shape and size of the sediment and is therefore usually constant during a field campaign. The fluid conductivity may vary throughout a field campaign due to variations in water temperature and salinity. Since m is independent of the fluid conductivity, calibration measurements using fresh water, saline water or LMT solution must yield the same m for the same sediment source.

Performing a full sensor calibration using a heavy liquid for every field site is difficult because of the cost of the heavy liquid. Instead, a reasonable field calibration scheme is as follows: the fluid conductivity σ_f is determined by taking measurements high in the water column, where no or negligible sediment is present, and must be updated frequently to account for variations in fluid conductivity. The calibration factor m is then determined by measuring the reduction in conductivity in a packed sediment bed with a known sediment volume fraction. Values for m obtained from measurements throughout the field campaign can then be averaged to yield a single, more robust value. This approach was used for the field results presented in Chapter

4, yielding a calibration factor *m* of 1.41, within the range of values presented in this study and in the literature.

2.5 Conclusions

A novel sensor was developed to measure the vertical profile of sediment concentration under sheet flow conditions. The sensor consists of a detachable probe with 32 plate electrodes spaced 1 mm in the vertical and an internal electronic circuit. The conductivity measurement is performed using a four-electrode approach, and a 29-point profile with 1 mm resolution is obtained by multiplexing through the electrode array. The conductivity response to sediment concentration was validated by measurements with known sediment masses in a Lithium Metatungstate (LMT) solution and agrees well with existing power-law (Archie's law) and linear relationships between electrical conductivity and sediment concentration. Since a power-law relationship is more supported by existing literature, this relationship was adopted as the calibration curve for the sensor and calibration coefficients $m = 1.36$ and 1.19 were found using a fine and coarse sand respectively.

The measurement volume of the sensor was studied using numerical simulations of the electric field around the conductivity probe. The horizontal extent of the measurement volume is estimated as extending 8.7 mm and 8.4 mm (1.5 times the sensor width) from the center of the sensor along the two principal horizontal axes. The vertical extent of the measurement volume causes a smoothing of the vertical concentration profile. Sediment concentration profiles with a sheet thickness of less than 5 mm are not resolved by the sensor. A correction factor was developed to account for the smoothing effect at larger sheet thicknesses.

Chapter 3

THE BEACH SAND TRANSPORT FIELD STUDY: EXPERIMENT CONDITIONS

Data presented in this work were collected during the Beach Sand Transport (BeST) field experiment, conducted in Perranporth, UK in October 2011. This study was conceived in response to the First International Workshop on Swash-Zone Processes, which identified comprehensive field measurements as a key need for future swash zone research [*Puleo and Butt*, 2006]. The experiment was conducted on October 9–15, 2011 as a collaboration between Plymouth University (UK), the University of New South Wales (Australia) and the University of Delaware (USA) with the aim of providing a comprehensive dataset of hydrodynamics, sediment transport and morphodynamics in the swash zone of a natural beach. A detailed overview of the study site, wave conditions and deployed instruments was also given by *Puleo et al.* [2014b].

3.1 Field Site

The field experiment was conducted on Perranporth beach, Cornwall, United Kingdom (Figure 3.1). Perranporth beach is a macrotidal, dissipative beach facing west-northwest and is enclosed between two headlands (Droskyn and Ligger Points) that are separated by approximately 3.5 km.

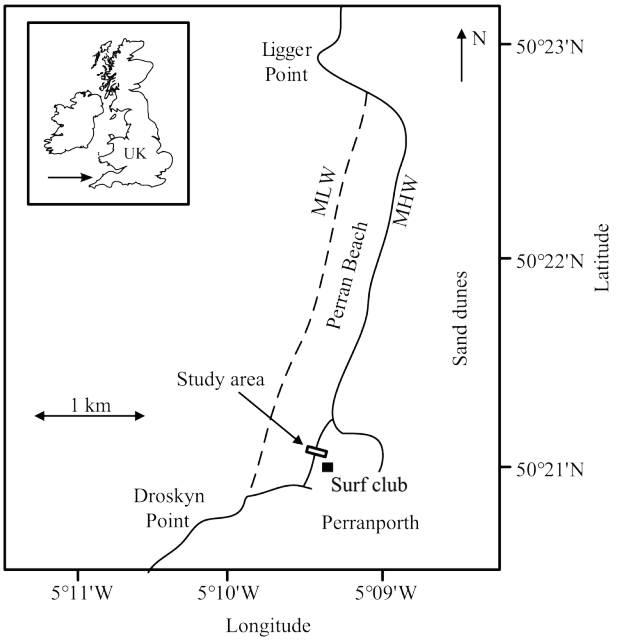

Figure 3.1: Location of the BeST field site in Perranporth.

Measurements were taken for approximately 3 hours around high tide for 10 consecutive tidal cycles around spring tide. Figure 3.2a and Table 3.1 show the predicted tidal level during this period. These particular tidal sequences, with a mean tide range of 5.43 m, were chosen because the high tides were all centered around 3 m Ordnance Datum Newlyn (ODN). The significant wave height (Figure 3.2b) and spectral peak period (Figure 3.2c) were measured in approximately 10 m water depth

Table 3.1: Offshore forcing conditions during the BeST field study.

Tide number	1	2	3	4	5	6	7	8	9	10
Date (day in October 2011)	10	11	11	12	12	13	13	14	14	15
H_s (m)	2.46	2.28	2.03	1.47	1.52	1.49	1.27	0.96	0.56	0.83
T_p (s)	9.9	11.7	11.0	10.2	15.2	13.0	11.0	10.5	9.4	10.6
Max. tide level (m Ordnance Datum Newlyn)	3.01	2.93	3.11	3.03	3.15	3.08	3.12	3.06	3.03	2.98

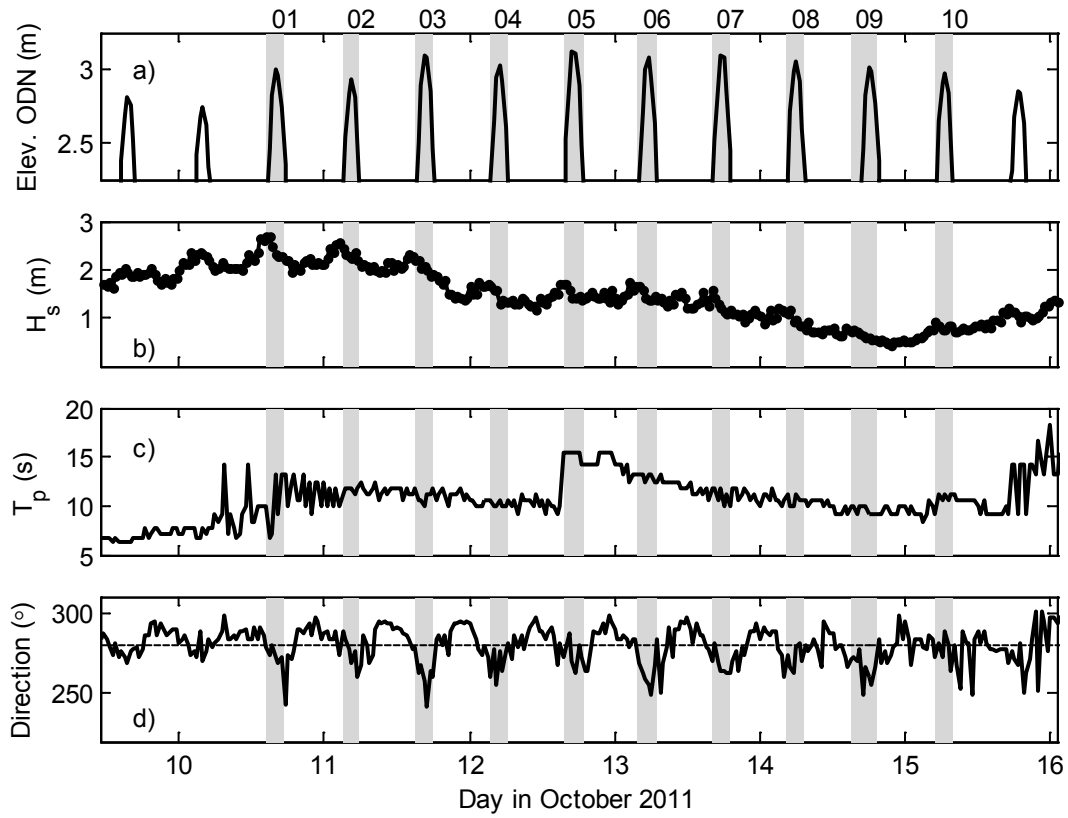

Figure 3.2: Offshore wave conditions for the BeST study. a) tide level. b) significant wave height. c) spectral peak period. d) wave direction. Horizontal dashed line is shore normal incidence. Gray shading in all plots indicates the sampling period.

by a Datawell Directional Waverider buoy (50°21′11.34″N, 5°10′30.11″W; Channel Coastal Observatory; www.channelcoast.org). Significant wave height at the beginning of the study exceeded 2.5 m and decreased over the remaining tidal cycles to around 0.5 m during the last high tide observed. The spectral peak period was approximately 10 s for the first four tidal cycles before increasing to 15 s before the fifth tidal cycle. The spectral peak period then decreased over the remainder of the experiment until it was again nearly 10 s during the last tidal cycle. The offshore peak

wave direction varied by up to 30° relative to shore normal (the dashed horizontal line in Figure 3.2d). Wave direction showed variability throughout the tidal cycle, implying that tidal effects at the location of the buoy played an important role in the depth influence on wave refraction. However, the wave obliquity in the surf and swash zones did not seem to exhibit this much spread about shore normal.

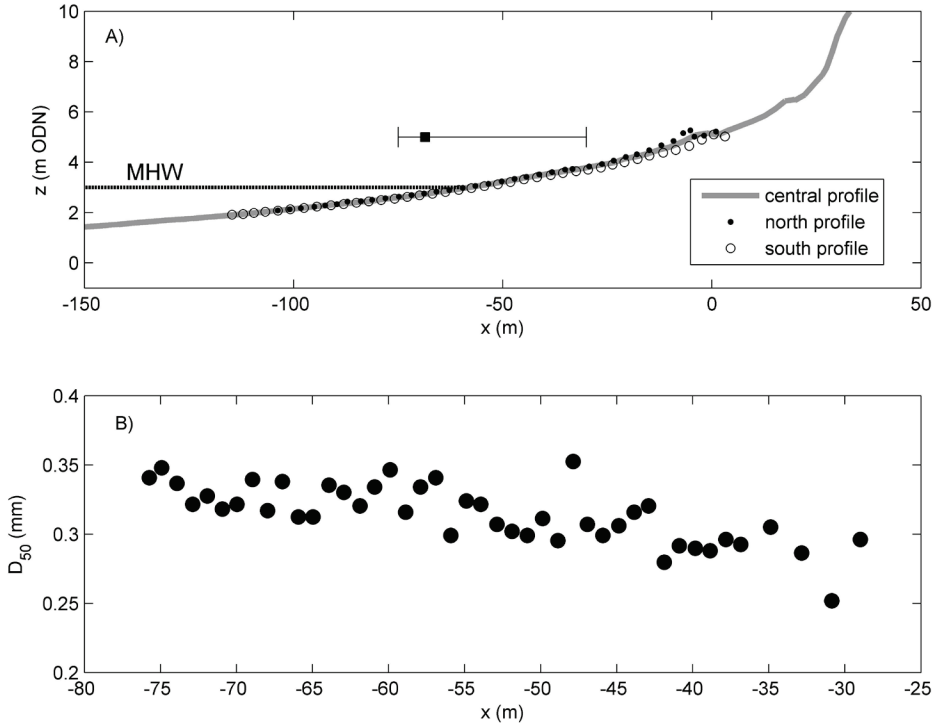

Figure 3.3: a) Beach profiles measured prior to high Tide 7 on October 13, 2011, along the central, north, and south transects: the horizontal dotted line identifies the mean high water level, the solid gray horizontal line indicates the cross-shore extent of the scaffold rig, and the black square the cross-shore location of the main instrument bar. b) median grain size within the extent of the scaffold rig as a function of cross-shore distance.

A 45-m-long scaffold frame was installed near the high tide line for mounting sensors (Section 3.2). A local right-handed coordinate system was established with cross-shore distance, x, increasing onshore and alongshore distance, y, increasing to the north. The beach profile down the center of the scaffold frame, and 25 m on either side of the frame, was surveyed using an electronic total station before and after each tide. Beach profiles measured prior to high tide 7 on October 13, 2011, are shown in Figure 3.3a. Beach profiles showed little alongshore variation and the slope near the mean high water line was roughly 1:45 for all three profiles. Surface sediment samples were collected along the central profile from $x = -75.7$ to -29.0 m at roughly 1 meter intervals. The median grain size, d_{50}, was determined using a settling tube. d_{50} near the main instrument bar was 0.33 mm, but showed a slight coarsening trend with increasing onshore distance (Figure 3.3b).

Repeated surveying of the beach profile showed a consistent steepening of the landward portion of the beach face throughout the experiment (Figure 3.4a). The cumulative elevation change indicated erosion of the order of 0.1 m seaward of the main instrument bar (the white dashed line in Figure 3.4a). Corresponding accretion of approximately 0.1 m was observed near the landward end of the scaffold frame where the landward and seaward ends of the scaffold frame are identified by the horizontal dashed black lines. Cross-sectional area changes based on pre- and posttide centerline cross-shore profile surveys were integrated across the profile and used to infer the net cumulative sediment flux per beach width required to cause the observed profile change. Cumulative sediment flux estimates varied from about 0.5 to 1.2 m^2 (Figure 3.4b). There was a flux increase in association with the increase in wave period around

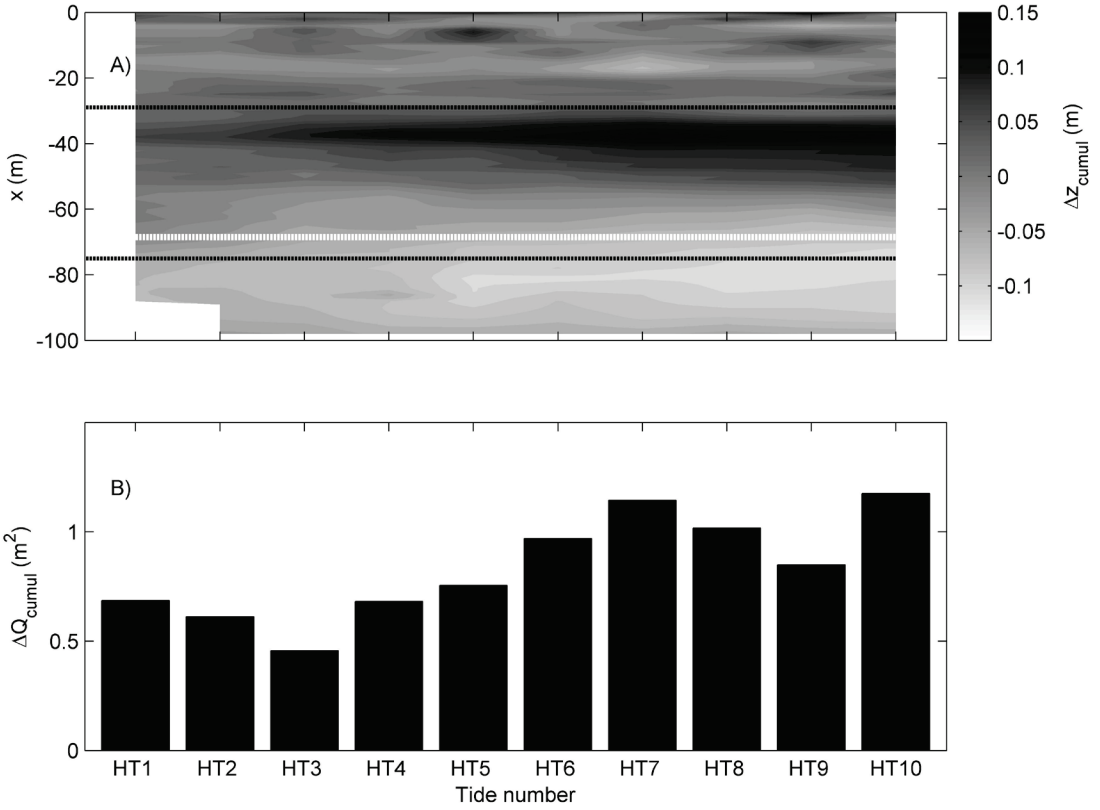

Figure 3.4: Morphological variability during the BEST field study. a) Cumulative elevation change for each tide: horizontal black lines denote seaward and landward edges of the scaffold frame and horizontal white line indicates the location of the main instrument bar. b) Cumulative volumetric flux required to cause measured elevation changes determined from pre- and post-tide beach profile surveys.

high tides 6 and 7 even though the significant wave height was smaller than earlier in the study period.

3.2 Instrumentation

Sensors were mounted on a 45-m-long scaffold frame installed near the high tide line (Figure 3.5a). Forty-five ultrasonic distance meters (UDMs; Massa M300/95) were installed at an elevation approximately 1 m above the bed at 1 m intervals

spanning the length of the frame. Each UDM measured the free surface when the area below it was immersed or the sand elevation when the area below it was exposed. Thus, the sensors can be used to obtain cross-shore time series of water depth and morphological change in the swash zone [*Turner et al.*, 2008]. UDMs were sampled at 4 Hz. A SICK lidar line scanner (SICK LMS511) was erected on a scaffold pole at an elevation of 5 m above the bed to obtain complimentary measurements to the ultrasonic distance meters [*Blenkinsopp et al.*, 2010a]. The line scanner was more highly resolved in the cross-shore than UDMs with an angular resolution of 0.25°, leading to a cross-shore spatial resolution of 0.025 m near the scanner and 0.2–0.4 m near the landward and seaward ends of the scaffold frame, respectively. The line scanner was sampled at 35 Hz. A near-bed pressure sensor (Druck PTX1830) for measuring forcing conditions was deployed 5 m seaward of the offshore end of the scaffold frame and sampled at 4 Hz.

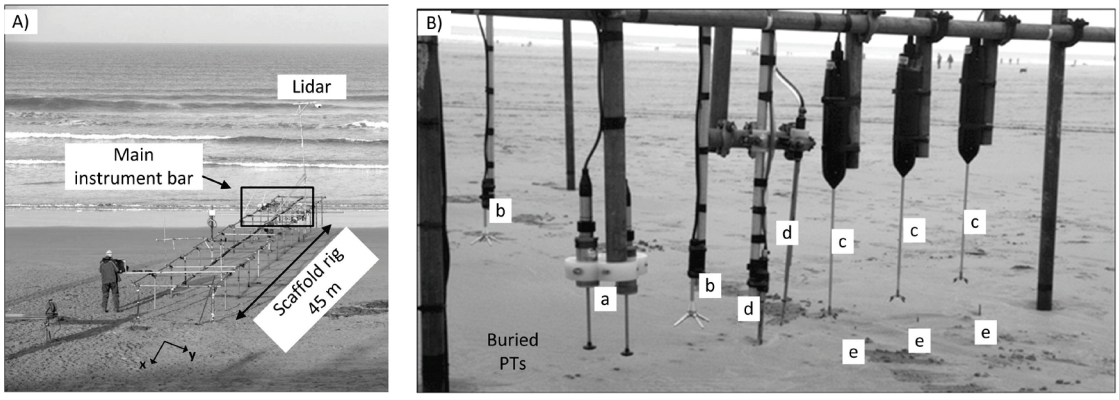

Figure 3.5: Images showing the (a) scaffold frame and (b) main instrument bar: sensors on the main instrument bar are (a) electromagnetic current meters; (b) Vectrino I velocimeters; (c) Vectrino II acoustic Doppler current profilers; (d) FOBS; (e) CCPs; the buried PTs are only identified by their name in the image.

Other swash-zone measurements were largely concentrated on a main instrument bar of the scaffold frame (Figure 3.5a), spanning 2 m in the alongshore (Figure 3.5b) and located near the mean high water line. Cross-shore and alongshore velocities (u and v, respectively) were recorded by two Valeport electromagnetic current meters (EMCMs) positioned nominally at 0.03 and 0.06 m above the bed (sensors denoted by a in Figure 3.5b). The cross-shore distribution of velocity and turbulence was recorded with three Nortek Vectrino I acoustic velocimeters (sensors denoted by b in Figure 3.5b). Each sensor measured the three velocity components (u, v, and w, where w is the vertical velocity) at nominally 0.05 m above the bed. One Vectrino I was located on the main instrument bar, with another located 1.5 m seaward and the other 1.5 m landward. Vectrino I sensors were sampled at 100 Hz. Highly resolved near-bed velocity profiles (u, v, and w) were recorded with three Vectrino II profiling velocimeters (PV; sensors denoted by c in Figure 3.5b). The PVs record the velocity profile at 0.001-m vertical bin spacing over a range of 0.03 m. The lowest PV was initially deployed so the lower 0.01 m of the profiling range was located within the bed. The additional PVs were deployed with alongshore offsets of 0.2 m and vertical offsets of 0.025 m. The PVs arrangement nominally provided the velocity profile from the bed level to around 0.07 m above the bed at 0.001-m increments. The PVs were sampled at 100 Hz. The main instrument bar contained a colocated UDM and also two buried pressure transducers (Figure 3.5b; Druck PTX1830). Buried pressure transducers were offset by 0.04 m in the vertical and the upper sensor was initially deployed 0.05 m below the bed. Pressure transducers were used to estimate infiltration rates and determine water depth, h, after accounting for the sensor distance below the bed.

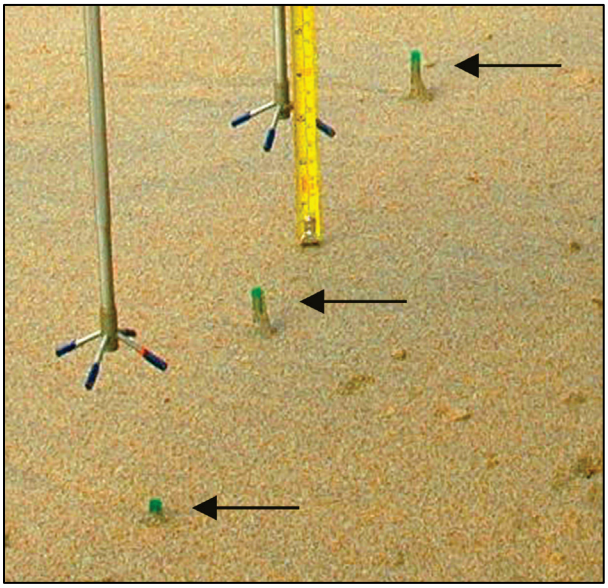

Figure 3.6: Sideways view of three buried CCPs, indicated by arrows. Down-hanging probes are Vectrino-II velocimeters. Yellow tape measure indicates scale.

Two different sensors were used to measure sediment concentration. Suspended sediment concentration was recorded using a newly constructed Fiber Optic Backscatter Sensor (FOBS). This version of the FOBS consisted of two separate probes (sensors denoted by d in Figure 3.5b). The lower probe contained 10 fiber optic send-receive pairs separated by 0.01 m in the vertical. The lower three pairs were initially buried to enable data capture under mildly erosive conditions. The upper 10 pairs had vertical spacing of 0.01, 0.02, 0.03, 0.03, 0.04, 0.05, 0.06, 0.06, 0.06, and 0.07 m. Only channels 1, 2, 4, 6, and 9 were functioning during the BeST study. The FOBS was sampled at 4 Hz. Sediment concentrations near the bed and in the sheet flow layer were measured using the Conductivity Concentration Profiler (Chapter 2). Three CCPs (sensors denoted by e in Figure 3.5b, also Figure 3.6) were deployed under the main instrument bar with alongshore separation of approximately

0.2 m and vertically separated to obtain a larger profile of the sediment concentration in the sheet flow layer. During deployment, sensors were aligned by eye such that the electrodes were parallel to the cross-shore direction to reduce wake effects and scour. CCPs were sampled at 4 Hz.

A 4-m aluminum tower was erected in the dunes landward of the scaffold frame to mount several cameras (denoted by A in Figure 3.7). A Sony DFW-X710 IEEE1394 protocol (firewire) visible-band, red-green-blue (RGB) camera with a 1024×768 pixel array sampled 5-min image sequences at 5 Hz every 15–30 min during daylight hours when the swash-zone sensors were actively recording. A FLIR thermal infrared camera with a 640×480 uncooled microbolometer sensitive in the 7- to 14-μm band sampled 5-min image sequences at 6.25 Hz every 15–30 min when the swash-zone sensors were actively recording during both daylight and darkness. Finally, a miniature, downward-looking, visible-band in situ bed camera (IBC) with a 720×576 pixel array was deployed from the instrument bar to identify (1) temporal phases of the swash cycle when bedload or sheet flow occurred, and (2) the instant when sediment mobility ceased during the bed settling process when only a thin sheet of water remained on the beach face at the end stages of backwash. Additionally, the IBC was used to confirm the correct cross-shore orientation of the CCP sensors and to confirm that the potential wake effects and scour caused by incorrect alignment were minimal. The IBC was sampled at 8 Hz.

All sensors were surveyed into the local coordinate system using an electronic total station. The main instrument bar was located near the mean high water line at a cross-shore location of x = -68.4 m (black square in Figure 3.3a). The scaffold frame

Figure 3.7: Overview of the BeST field location displaying camera tower (A), data logging cabins (B), instrumentation scaffolding (C).

extended from x = -74.8 m to x = -30.7 m (horizontal extent shown in Figure 3.3a). All sensors on the scaffold frame and the RGB and thermal cameras were cabled into a shore-based cabin for power, control, and data acquisition (B in Figure 3.7). The numerous sensors and cameras were recorded on individual laptop computers. Recorded data was synchronized in time but measurements were not triggered simultaneously across different sensors. Time synchronization between sensing systems was achieved using global positioning system (GPS) time standard (coordinated universal time, UTC) and network time protocol (NTP) software. One laptop computer served as the master time server with other laptops receiving the time code either via wired or wireless connection. Each laptop updated its internal clock every second with the master time server to avoid clock drift. The elevation above the

bed for sensors on the main instrument bar was measured before and following each tide. Vertical adjustments were made prior to the subsequent tide, as necessary, to return sensors to their planned elevations.

Chapter 4

SHEET FLOW SEDIMENT TRANSPORT DURING QUASI-STEADY BACKWASH

After a number of preliminary field tests at the Indian River Inlet south beach (Delaware) and on Wembury beach (UK), the BeST field study was the first formal deployment of the CCP. This chapter describes results from CCP measurements of sediment concentration in the sheet flow layer during the BeST study, focusing on the simplest form of sheet flow observed in the swash zone: quasi-steady backwash where flow accelerations, pressure gradients and bore turbulence were negligible and the sheet flow resembled stationary, unidirectional sheet flow. The dissipative beach at the BeST field site had an infragravity-dominated swash zone, generating many quasi-steady backwash events.

4.1 Measurements Quality Control

The first high tide measurement cycles during the BeST study were used to test the CCP instruments and optimize the sensor positioning. Only measurements from three high tides (tides 7-9), taken during 13 and 14 October, are discussed in this chapter. To ensure the quality of the sediment concentration profile measurements made by the CCP, measurements were discarded if any of the following conservative criteria were met:

- Sheet flow occurred with a sheet layer thickness smaller than 5 mm as this cannot be accurately resolved by the CCP.

- The angle of the flow velocity vector relative to shore normal exceeded 15°. Flow angle time series were determined using the lower EMCM velocity measurements. This criterion ensured that the flow was nearly shore-normal and thus roughly parallel to the CCP probe. As the probe is 1.6 mm thick and 5.6 mm wide, flow disturbance and scour will be insignificant when the flow is aligned with the sensor. Under oblique flow, eddy shedding and scour may occur near the sensor, altering the sheet flow layer near the sensor. When the water level was below the lowest current meter, no velocities and no flow angle could be determined. In this case, CCP measurements were discarded for lack of a reliable velocity signal even though it is believed that the CCP still accurately captures sheet flow sediment concentrations during these instances.

- The 15 minutes following the first bore arrival during rising tide were discarded to allow the sand bed to compact and fully saturate around the CCP probes.

- When two collocated CCPs both recorded the entire sheet layer within the profiling window and the calculated sheet thickness differed by more than 4 mm, the measured sheet thickness was discarded.

Over the three high tide measurement periods, CCP measurements were made for a total of 94765 sampling instances (6.5 hours). Sheet flow with a thickness of 5 mm or more was recorded for 25199 sampling instances (112 minutes). 69 % of these measurement instances occurred under oblique flow or when no current meter data were available, 3 % occurred during the first 15 minutes of each high tide cycle and CCP sheet thicknesses disagreed by more than 4 mm for 2 %. As a result, 7416 sampling instances (31 minutes) passed all quality control criteria. Two CCPs recorded the sheet flow layer simultaneously during many of these instances leaving 10082 sediment concentration profiles that passed the quality control criteria.

The least complex swash-zone sheet flow sediment transport conditions occur under quasi-steady backwash when effects from bore-generated turbulence, pressure

gradients and phase lags are negligible. Quasi-steady backwash conditions were defined when all of the following criteria were met:

- The velocity as measured by the lowest EMCM was offshore-directed.

- Fluid accelerations were small. A threshold for accelerations was defined as $\frac{dU}{dt} < 1.2\ g \sin\gamma = 0.27\ m/s^2$, where γ is the beach slope, g is gravitational acceleration, and U is the flow velocity magnitude measured by the lowest EMCM. Swash flow during the backwash initially accelerates under gravity and the acceleration decreases at the end of the swash cycle when the gravitational force is balanced by bottom friction [*Hughes and Baldock*, 2004]. Acceleration effects are assumed to be small when the flow accelerates under gravity on a low-sloping beach. The acceleration threshold used here is an order of magnitude smaller than peak accelerations in oscillatory flow tunnel studies (e.g., $\left(\frac{dU}{dt}\right)_{max} = 1.33 - 2.00$ in *O'Donoghue and Wright* [2004a]; $\left(\frac{dU}{dt}\right)_{max} = 1.47 - 1.87$ in *Ruessink et al.*[2011]) and corresponds to a modified Sleath number S [*Foster et al.*, 2006a]

$$S = \frac{\frac{dU}{dt}}{(s-1)g} = 0.017 \tag{4.1}$$

  where $s = 2.65$ is the relative density of the sediment. This Sleath number is an order of magnitude smaller than the limit for pressure gradient-induced sediment mobilization [*Sleath*, 1999; *Foster et al.*, 2006a].

- Abrupt water depth changes were occasionally recorded by the pressure transducer during the backwash when no acceleration was registered. This may either be caused by a small secondary wave propagating onshore during a backwash, or when a new bore arrived at the sensor location and initiated a new uprush event while the near-bed flow velocity was still offshore-directed. These events were excluded by discarding all measurements when $\frac{dh}{dt} > 0.05\ m/s$.

- If the acceleration and water depth thresholds were exceeded for a particular record, data from 0.75 s before until 0.25 s after the measurement were also removed from the time series since a sudden acceleration or bore may stir up sediment that stays mobilized during later times and to account for small timing differences between the different instruments.

5313 measurements were taken during backwash events (22 minutes). 22% of these measurements were rejected due to accelerations and 14% because of water depth changes. As a result, a total of 3863 measurements were taken during quasi-steady backwash (16 minutes). Again, the sheet layer was measured by two CCPs during some of these instances, resulting in a total of 5365 profiles.

4.2 Example Time Series

A first time series excerpt, collected during tide 9 (October 14, 2011 at 18:52 UTC) is shown in Figure 4.1. A single swash event is shown with a duration of 26 s, a maximum water depth of 0.11 m (Figure 4.1a), and maximum uprush and backwash velocities of 1.43 m/s and -1.15 m/s, respectively (Figure 4.1b). Two of the three CCPs (designated as CCP A and CCP B) deployed during tide 9 were located at approximately the same vertical elevation and at an alongshore separation of roughly 0.2 m and captured the same sheet flow events. This makes it possible to examine the repeatability of CCP measurements by comparing measurements by CCPs A and B. Figure 4.1c shows concentration time series measured by 6 channels separated by 2 mm from CCP A. Channels at -4.9 mm, -2.9 mm and -0.9 mm were below the initial bed level. The bed eroded by 3.5 mm upon bore arrival ($0 \text{ s} \leq t \leq 3 \text{ s}$) resulting in a reduction of sediment concentration at these elevations as sediment was carried higher into the water column and landward in the cross-shore direction. Channels at 3.1 mm and 5.1 mm were initially covered by a thin film of water from a previous swash

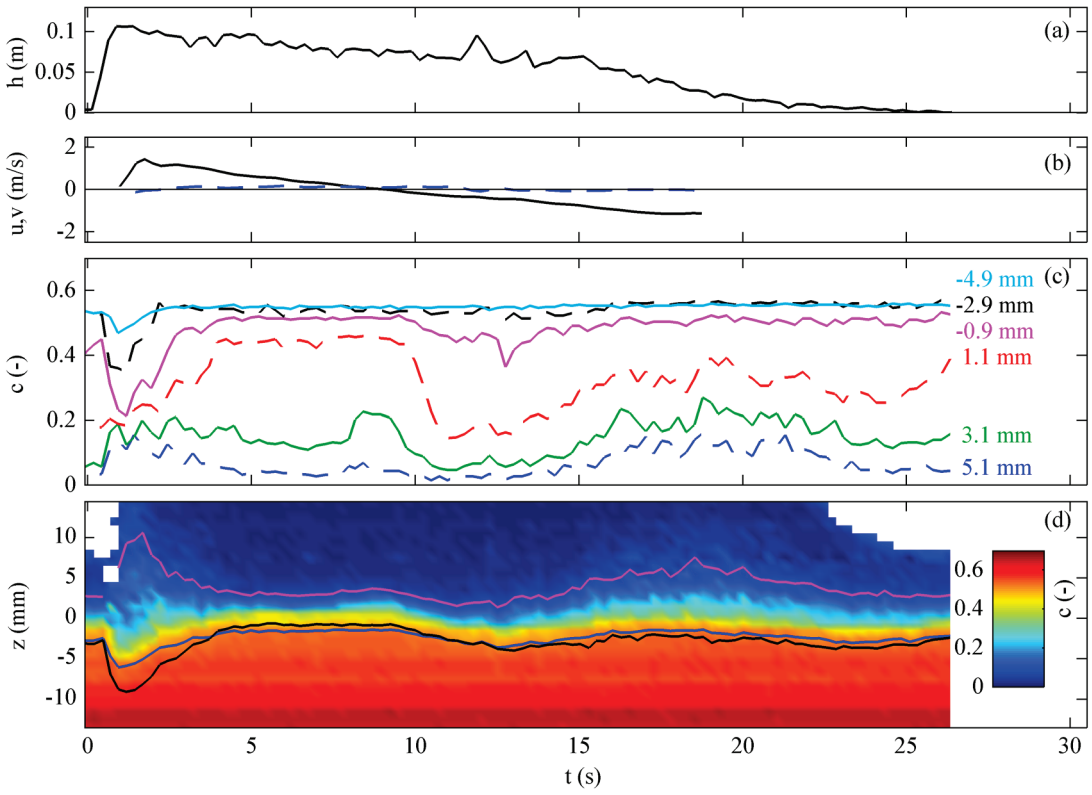

Figure 4.1: Time series excerpt of swash-zone measurements. (a) Water depth time series. (b) cross-shore (u, solid line) and alongshore (v, dashed line) velocity measured 0.03 m above the bed. (c) Time series of measured concentrations at 6 elevations from CCP A. (d) Contour time series of sediment concentrations from CCP B. Black line indicates bottom of the sheet flow layer according to the curve-fitting method described in section 4.3.1, blue line indicates bottom of sheet flow layer according to concentration cut-off (c = 0.51, see section 4.3.1), magenta line indicates top of sheet flow layer (c = 0.08).

event, and upon bore arrival recorded a large sediment concentration. Thus, concentrations above the initial bed level were in phase with the flow velocities and concentrations below the bed level were in anti-phase with flow velocities. These phase relationships correspond to the behavior of the upper sheet flow layer and the pick-up layer as described by *Ribberink and Al-Salem* [1995]. Before the arrival of

the bore, the channel at 1.1 mm was in the smoothed transition between the sand bed and water column and therefore few conclusions can be drawn from the time series from this channel. Between 10 s < t < 17 s, the measured concentration at 1.1 mm decreased as the general bed level temporarily eroded by roughly 3 mm and subsequently accreted. A similar behavior for the different channels occurred during backwash sheet flow, but was obscured by a background bed level change on the order of 2 mm during the backwash, which shifted the positions of the individual CCP channels with respect to the bottom. The effect of the bed level change on the concentration signal of an individual CCP channel was larger than the effect of a time-varying sheet flow layer. For example, the channel at -0.9 mm shows an increase in sediment concentration at 12.5 s < t < 18 s despite an increase in sheet thickness because there was concurrent accretion, moving the sensor channel from the sheet layer (lower concentration) toward the stationary bed (higher concentration). Sediment concentrations as a function of time and vertical elevation measured by CCP B are shown in Figure 4.1d. The evolution throughout the swash event is analogous to Figure 4.1c. Magenta and black lines indicate the top and bottom boundary of the sheet flow layer as defined in the Section 4.3.1. The blue line indicates an alternative definition of the bottom of the sheet layer as the contour of c = 0.51 (see also Section 4.3.1).

A second time series excerpt, also collected during tide 9 (October 14, 2011 at 17:30 UTC), is displayed in Figure 4.2. Multiple swash events occurred with gravity-timescale bores superimposed on infragravity-timescale swash cycles with a maximum depth of 0.22 m. The flow direction alternated multiple times between onshore (uprush) and offshore (backwash) within a single infragravity swash cycle in

conjunction with the gravity-timescale bores. Cross-shore and alongshore velocities are displayed in Figure 4.2b, with the cross-shore velocity displayed as a thick black

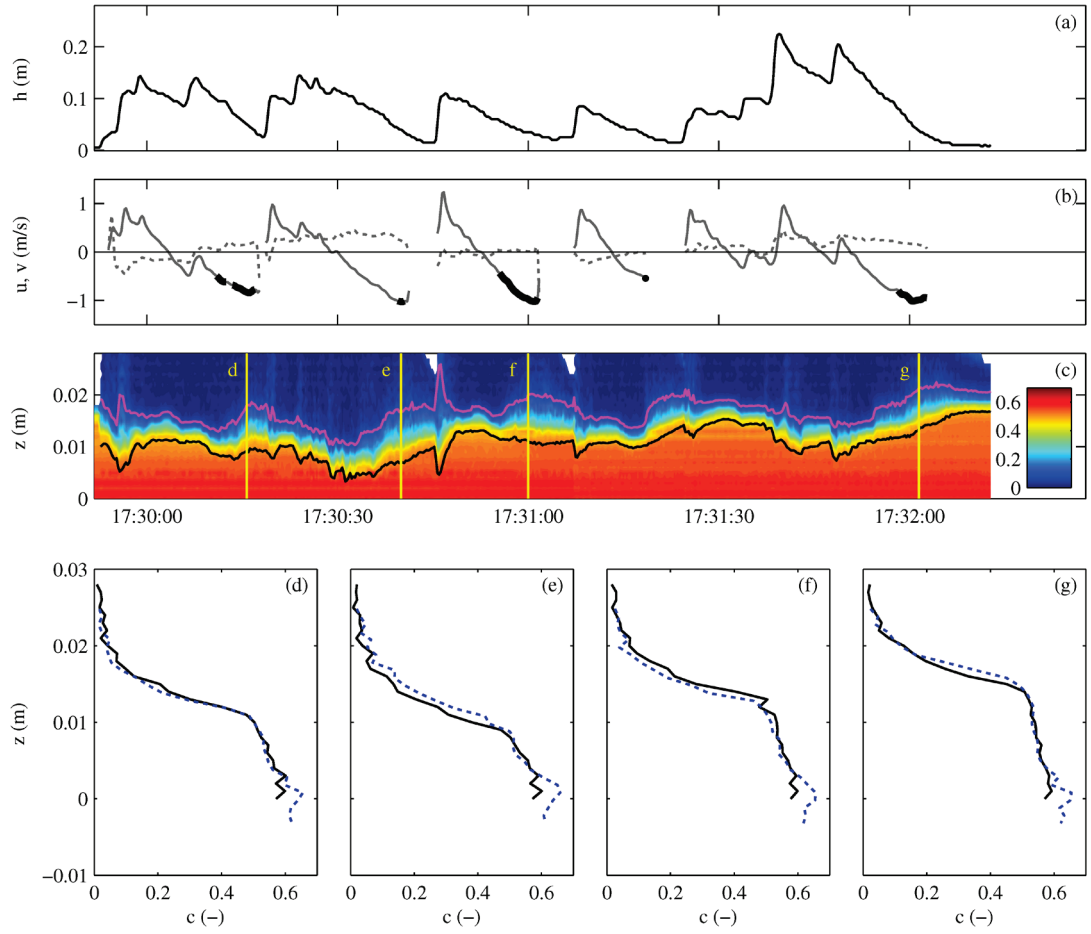

Figure 4.2: Time series excerpt of swash-zone measurements. (a) Water depth. (b) Cross-shore (solid line) and alongshore (dotted line) velocity. Thick black line indicates when quasi-steady backwash sheet flow occurred that complied with all quality-control criteria. (c) Sediment volume fraction measured by CCP. Magenta (black) line indicates top (bottom) of sheet layer, yellow vertical lines indicate times when instantaneous profiles are displayed in panels d-g. (d-g) Instantaneous sediment volume fraction profiles measured by two collocated CCPs (CCP A and CCP B) during four instances of the event, indicated by yellow lines in panel c.

curve for times when quasi-steady sheet flow occurred that met all quality control criteria. Sediment concentration measurements (Figure 4.2c) demonstrate that the sediment bed was active throughout most of the swash event, with the immobile bed level (black line) nearly continuously changing as a result of local hydrodynamic forcing and cross-shore and alongshore sediment transport gradients. Black and magenta lines again indicate the bottom and top boundary of the sheet flow layer as defined in the section 4.3.1. Smoothing of the sediment concentration profile by the CCP instrument (see section 2.3.2.3) causes the top and bottom boundary to appear to be separated by approximately 4-5 mm when the bed is at rest and no sheet flow layer is present, which was the case during gradual flow reversals (e.g., at 17:30:03 UTC and 17:30:52 UTC).

When the top and bottom boundaries of the sheet flow layer (black and magenta lines in Figure 4.2c) are separated by more than 5 mm, sediment is considered to be mobilized as sheet flow. Sheet flow under quasi-steady backwash conditions occurred for 5 quality-controlled backwash events during this time segment, highlighted by thick black lines in Figure 4.2b. Some backwash flows, e.g., at 17:30:30-17:30:41 UTC, contained a strong alongshore component, resulting in flows oblique to the CCP probe and sheet thicknesses were discarded during these instances. During other instances, such as at 17:31:01-17:31:06 UTC, the backwash flow was too shallow to be recorded by the lowest current meter, meaning that flow angle could not be determined. Instantaneous sediment concentration profiles are displayed in Figure 4.2d-g for 4 backwash sheet flow events indicated by yellow vertical lines in Figure 4.2c. The agreement between sediment concentration profiles

measured by CCP A and CCP B (black solid line and blue dotted line in Figure 4.2d-g) indicates repeatability of the measurements.

4.3 Concentration Profile

4.3.1 Top and Bottom Boundary of the Sheet Layer

The top boundary of the sheet flow layer is typically defined as the location where grains become (on average) separated enough so that intergranular forces become negligible. *Bagnold* [1956] defines the top boundary at the volume fraction where the mean radial separation distance between grains equals one grain diameter, $\lambda = 1$, equivalent to a sediment volume fraction c of 0.08. Therefore, c = 0.08 was chosen as the cut-off concentration for the top of the sheet flow layer, similar to previous sheet flow sediment transport studies (Figure 4.1d and Figure 4.2c, magenta line) [*Dohmen-Janssen and Hanes*, 2002; *O'Donoghue and Wright*, 2004a].

The bottom boundary of the sheet flow layer, the boundary between the sheet flow layer and the non-moving sediment bed, is more difficult to define since the concentration of the non-moving sediment bed varies over time under field conditions. Sediment that is packed at the closest packing limit, around c = 0.644 for natural sands [*Bagnold*, 1966b], is immobile by definition. Sediment that is packed at a concentration between the closest packing limit and the loosest packing limit may be mobile or immobile since it is packed densely enough to support itself statically, but loosely enough to allow sediment motion. Moreover, the loose packing fraction is difficult to determine experimentally and is not as well-established as the random close-packing limit. The loose packing limit is approximately c = 0.55 for uniform spheres [*Song et al.*, 2008], but may be less for natural sands. *Bagnold* [1966b] found

$c = 0.51$ for beach sand, and *Baker and Kudrolli* [2010] found $c = 0.50$-0.54 for platonic solids which, like natural sand, are angular, lowering the random loose packing limit. A simple approach to defining the bottom of the sheet flow layer was applied in a preliminary analysis of the BeST field measurements where the bottom was defined as the location where the smoothed measured concentration profile exceeds the loose packing limit, $c = 0.51$ [*Lanckriet et al.*, 2013] (Figure 4.1, blue line). Although this approach yielded satisfying results for the event displayed in Figure 4.1, it produced many erroneous estimates for the bottom of the sheet layer in other locations of the dataset. A more sophisticated method for determining the bottom of the sheet flow layer is therefore required.

Yu et al. [2012] divided the sheet flow layer into two parts: an upper layer of 'rapid sediment flow' with $c_l < c < c_t$ and a lower layer with $c_c < c < c_l$, where $c_t = 0.08, c_l = 0.57$ and $c_c = 0.635$ are the concentration at the top of the sheet layer, the random loose packing concentration and the random close packing concentration, respectively. In the lower layer, grains are in enduring contact and the flow behaves like a glassy solid. Experimental results by *Capart and Fraccarollo* [2011] display a similar division of the sheet flow layer into two sublayers. Results from a 1DV, two-phase numerical model based on this division show that the total sediment transport in the lower layer is smaller [O(10%)] than in the upper layer for unidirectional, sinusoidal and skewed oscillatory flow, and that there is a sharp 'shoulder' transition in the concentration profile between the two layers [*Amoudry et al.*, 2008; *Yu et al.*, 2010]. This shoulder is also observed in measured sheet flow sediment concentration profiles [*O'Donoghue and Wright*, 2004a; *Dohmen-Janssen and Hanes*, 2005]. Since the shoulder is also observed in sediment concentration profiles measured by the CCP,

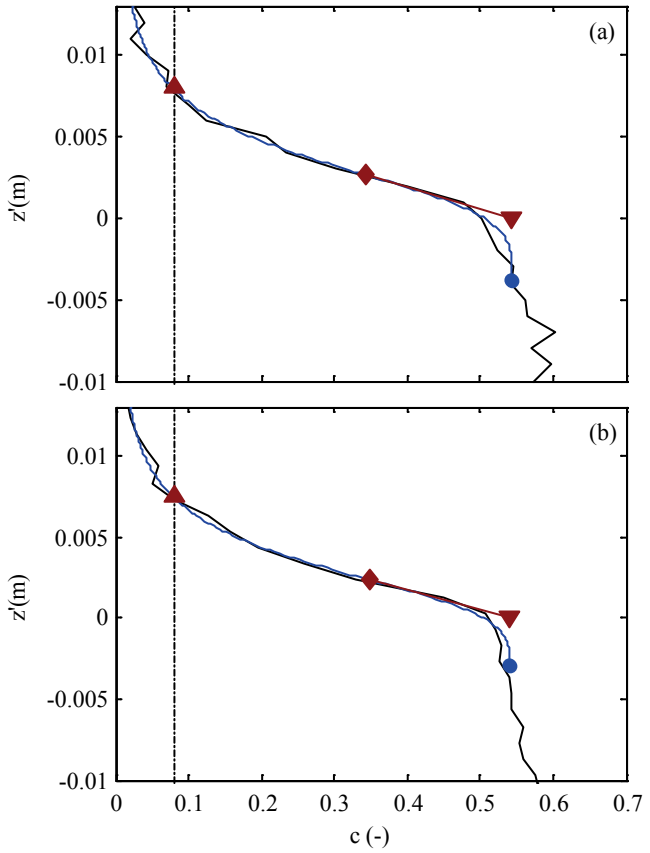

Figure 4.3: Instantaneous sediment concentration profiles recorded during quasi-steady backwash events at (a) 17:30:15.75 UTC (Figure 4.2d) and (b) 17:32:1.50 UTC (Figure 4.2g). Black line indicates the measured concentration profile. Blue line indicates curve fit of the form of equation 4.3. Red diamond indicates inflection point in curve. Red upward facing triangle and red downward-facing triangle indicate the top and bottom of the sheet layer, $\boldsymbol{z_t}$ and $\boldsymbol{z_e}$, respectively.

it was used to define the bottom of the sheet layer using a technique similar to *O'Donoghue and Wright* [2004a]. This means that the glassy lower region of the sheet flow layer, and the small fraction of the total sheet flow transport that may take place in this layer, was ignored.

Instantaneous concentration profiles for two of the backwash sheet flow events discussed earlier are displayed in Figure 4.3 to illustrate the method to determine the top and bottom boundaries of the sheet flow layer. To determine the top boundary of the sheet flow layer, the instantaneous profile (Figure 4.3, black lines) was smoothed spatially using a boxcar average with a width of 3 mm (3 points in the profile) and the top of the sheet layer was defined as the elevation where the smoothed concentration profile equals 0.08 (red upward-facing triangles in Figure 4.3).

The sharp shoulder transition in the sheet flow concentration profiles was observed in both profiles at volume fractions between 0.51 and 0.55 (Figure 4.3). The method used to define the bottom boundary of the sheet flow layer is based on *O'Donoghue and Wright* [2004a] who fitted a curve to the sheet flow sediment concentration profile of the form:

$$\check{c}(z) = \frac{\beta^{\alpha}}{\beta^{\alpha}+[z-z_1]^{\alpha}} \tag{4.2}$$

where $\check{c}(z)$ is the instantaneous sediment concentration profile normalized by the sediment concentration in the packed bed, z_1 is the first estimate of the bottom of the sheet flow layer, and α and β are fitted shape parameters. Since the concentration in the packed bed varies under field conditions, a curve of the following form is used instead (referred to hereafter as the ODW curve):

$$c(z) = c_b \frac{\beta^{\alpha}}{\beta^{\alpha}+[z-z_1]^{\alpha}} \tag{4.3}$$

where c_b is the concentration in the bed, determined by fitting (4.3) to each of the instantaneous concentration profiles with α, β, c_b and z_1 as free parameters. *O'Donoghue and Wright* [2004a] found that due to the shape of this curve, the estimated bottom of the sheet layer z_1 is sometimes too low and this is also seen in the

curves in Figure 4.3(blue circles). Therefore, they extended a straight line through the inflection point of the curve (red diamond in Figure 4.3) and defined an improved estimate of the bottom of the sheet layer, z_e, as the intersection of the straight line with the bed concentration c_b (down-facing triangle). For the profiles displayed in Figure 4.3, the elevation z_e of the new estimate for the bottom of the sheet layer agrees well with the location of the shoulder in the profile and z_e was therefore chosen as the bottom of the sheet flow layer and is displayed as a black line in Figure 4.1d and Figure 4.2c. The bottom of the sheet defined by the $c = 0.51$ contour (blue line, Figure 4.1d) and the curve-fitting method (black line, Figure 4.1d) are in good agreement for the event shown in Figure 4.1. Throughout the entire dataset, the curve-fitting method appeared to be more reliable with less erroneous detections of the bed level. Defining the bottom of the sheet flow layer by extending the linear portion of the sheet flow concentration profile is similar to the method used by *Pugh and Wilson* [1999]. The sheet flow layer thickness δ_s was defined for each individual profile as the vertical distance between the top and bottom boundary of the sheet flow layer. The measured sheet flow layer thickness was then corrected for the smoothing effect using equation (2.13) (Section 2.3.2.3).

4.3.2 Ensemble-averaged Sediment Concentration Profiles

Sediment concentration profiles under quasi-steady backwash conditions were grouped according to the measured sheet thickness in 1 mm bins. Individual profiles were centered around the elevation where the concentration of the smoothed individual profile (using a 3-point boxcar average) equals 0.30 to align profiles in the vertical. Other methods, such as centering profiles around the top or bottom of the sheet layer, or the mean elevation of the top and bottom, resulted in a larger spread of

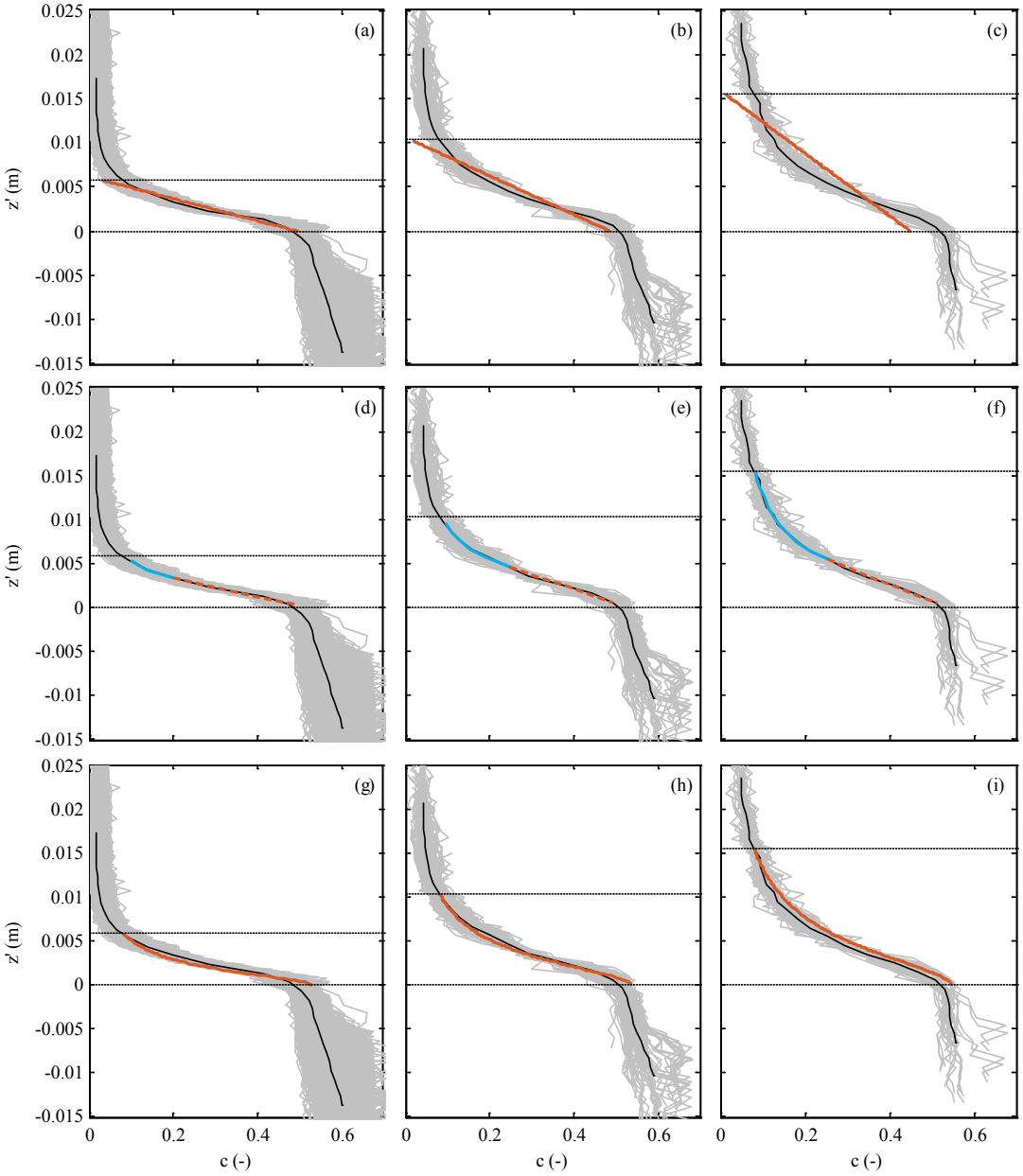

Figure 4.4: Ensemble-averaged sediment concentration profiles for sheet thicknesses of 6 mm (left column), 11 mm (middle column) and 16 mm (right column). Gray lines indicate individual profiles; dotted black line indicates ensemble-averaged profile. Horizontal lines indicate top and bottom of sheet layer. Top row: Orange solid line indicates linear fit. Middle row: blue solid line and orange dashed line indicate power law and linear law components of the composite curve fit. Bottom row: orange solid line indicates ODW curve with $\alpha = 1.73$ fixed.

the individual profiles. Using the centered, non-smoothed individual profiles, an ensemble-averaged profile was calculated for each sheet flow layer thickness. The average concentration at a particular elevation of the ensemble-averaged profile was only retained if at least one third of all individual profiles had a valid concentration measurement at that elevation. Ensemble-averaged profiles for sheet thicknesses of 6 mm, 11 mm and 16 mm are displayed in the left, middle and right columns of Figure 4.4 respectively.

Qualitatively, the bin-averaged profiles appear linear in the lower part of the sheet flow layer and have a power-law tail toward the top of the sheet flow layer, particularly for larger sheet thicknesses (Figure 4.4 c,f,i), in agreement with past studies [*Sumer et al.*, 1996; *Pugh and Wilson*, 1999]. The measured sediment concentration in the non-moving sediment bed ($z\text{-}z_e < 0$) shows variability of $O(0.10)$. Laboratory measurements in a packed sediment bed demonstrated that instrument measurement accuracy is on the order of 0.03 (Figure 2.6). The variability observed in Figure 4.4 is therefore likely because the upper layer of the non-moving bed was deposited by natural wave-induced sediment transport and was constantly reworked by shear, erosion and deposition throughout the high tide measurement cycle. For sheet thicknesses of 6 mm and 11 mm, the concentration appears to increase monotonically in the bed. This is likely due to the fact that the sand was initially deposited loosely and was subsequently packed down by the weight of sediment deposited above. As with the individual concentration profiles, the top of the sheet layer z_t was again determined as the elevation where the ensemble-averaged concentration profile, smoothed using a 3-point boxcar average, equaled 0.08. The bottom of the sheet layer z_e and the concentration in the bed c_b were first determined by fitting a curve of the

form (4.3) to the bin-averaged profile and extending the curve from the inflection point to the bed concentration to determine the bottom of the sheet layer z_e, as was done for the individual concentration profiles. This determined the top and bottom of the sheet flow layer, the sheet flow layer thickness and the concentration in the bed.

Past work has suggested different shapes for the sediment concentration profile in the sheet layer. Several of these shapes, along with newly proposed shapes, were compared to the ensemble-averaged measured profiles. First, a linear profile has been proposed [*Hanes and Bowen*, 1985; *Wilson*, 1987]

$$c(z) = a_1 z + a_2, \tag{4.4}$$

where a_1 and a_2 are fitting parameters. Secondly, a power law has also been proposed as a shape for the concentration profile in the sheet layer [*Ribberink and Al-Salem*, 1994]

$$c(z) = b_1 (z')^{b_2}, \tag{4.5}$$

where b_1 and b_2 are fitting parameters and $z' = z - z_e$ is the elevation above the bottom of the sheet layer. Third, *Sumer et al.* [1996] and *Pugh and Wilson* [1999] stated that the profile had a linear shape in the lower section of the layer and a power law tail at the upper section, defined here as a composite profile:

$$c(z) = \begin{cases} d_1(z' - z_{transition}) + c_{transition} & , z' \le z_{transition} \\ c_{transition}\left(\frac{z'}{z_{transition}}\right)^{d_2} & , z' > z_{transition} \end{cases} \tag{4.6}$$

where d_1 and d_2 are fitting parameters, $z_{transition}$ is the elevation above the bottom of the sheet layer where the profile transitions from a linear to a power law shape and $c_{transition}$ is the concentration at $z_{transition}$.

Fourth, *O'Donoghue and Wright* [2004a] proposed a curve of the form (4.2). The ODW curve can be rewritten in terms of the sheet thickness δ_s instead of a generic length scale β:

$$c = c_b \frac{1}{1+\left(\frac{z'}{\delta_s}\right)^{\alpha}\frac{c_b-c_t}{c_t}}, \tag{4.7}$$

where $c_t = 0.08$ is the concentration at the top of the sheet layer. Each of these curves was fitted between the top and bottom boundary of the sheet flow layer. For each shape, the goodness of fit was evaluated using the coefficient of determination R^2, defined as

$$R^2 = 1 - \frac{\sum_i (c_i - \bar{c})^2}{\sum_i (c_i - \hat{c_i})^2}, \tag{4.8}$$

where c_i are the discrete concentration values in the ensemble-averaged profile, $\bar{c}$ is the mean of all concentration values c_i in the ensemble-averaged profile, and $\hat{c_i}$ are the values predicted by the curve fit. Results for all fitted shapes are summarized in Table 4.1.

Table 4.1: Summary of fitting results for ensemble-averaged profiles.

Sheet thickness (mm)	6	7	8	9	10	11	12	13	14	15	16	17	18
# profiles	1574	903	651	418	204	130	97	84	68	64	44	41	42
R^2: linear	0.97	0.96	0.96	0.97	0.96	0.96	0.94	0.92	0.92	0.90	0.89	0.87	0.87
R^2: power law	0.78	0.85	0.90	0.61	0.76	0.83	0.88	0.88	0.69	0.74	0.80	0.81	0.88
R^2: composite	0.99	1.00	1.00	1.00	1.00	1.00	1.00	1.00	1.00	1.00	1.00	1.00	1.00
$c_{transition}$	0.20	0.21	0.22	0.23	0.24	0.24	0.24	0.24	0.25	0.25	0.25	0.29	0.30
$z_{transition}/\delta_s$	0.57	0.54	0.51	0.48	0.46	0.44	0.43	0.39	0.38	0.36	0.35	0.27	0.28
R^2: ODW (α free)	0.98	0.99	0.99	0.99	0.99	0.99	1.00	1.00	1.00	1.00	1.00	1.00	1.00
α: ODW	2.03	1.99	1.94	1.89	1.86	1.82	1.80	1.65	1.61	1.56	1.53	1.44	1.51
R^2: ODW ($\alpha = 1.73$)	0.95	0.97	0.97	0.98	0.99	0.99	1.00	0.99	0.99	0.98	0.98	0.94	0.96

The linear fit (red dotted line, Figure 4.4a,b,c) describes the sheet layer relatively well for small sheet thicknesses. For larger sheet layers, however, the discrepancy between the concentration profile and the linear fit increases as the power-law tail at the top of the sheet layer becomes more prominent. The coefficient of determination R^2 thus decreases from 0.97 for small sheet layer thicknesses to 0.87 for large thicknesses. The power law is not a satisfactory description for the sheet layer down to the non-moving bed ($0.61 \leq R^2 \leq 0.90$) because the concentration diverges to infinity as $z' \rightarrow 0$ for a concentration profile that decays away from the bed (exponent $b < 0$).

The composite profile (Figure 4.4d,e,f) provides a near-perfect fit for all sheet layer thicknesses ($R^2 > 0.99$). The transition point between the linear and power-law segment was chosen so that the overall composite profile had the maximum coefficient of determination R^2, making it possible to determine where the profile transitions from a linear to a power-law shape. The concentration profile transitions to a power-law shape at concentrations in the range 0.20 – 0.30 and at elevations of 0.27 δ_s - 0.57 δ_s (Table 4.1). The results are not sensitive to the location of the transition point so the elevation of the transition point (and the associated concentration) can be changed by several millimeters without significantly reducing the goodness of fit.

The ODW curve expressed as equation (4.7) was fitted to the data with the sheet thickness δ_s and the concentrations at the top and bottom of the sheet layer, c_b and $c_{t,}$ all held fixed, and with the shape parameter α as the only free parameter, resulting in an excellent fit to the ensemble-averaged concentration profiles ($R^2 \geq$ 0.98). The shape parameter α varied between 1.44 and 2.03, in good agreement with the range of values for α = 1.1-1.9 found by *O'Donoghue and Wright* [2004a] for

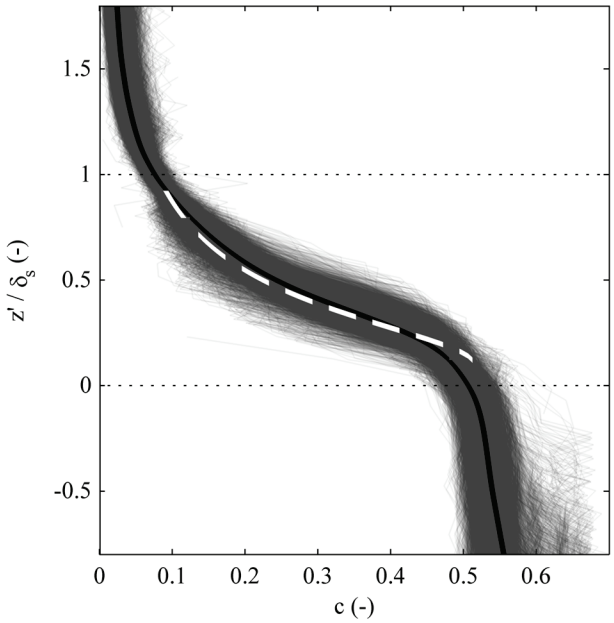

Figure 4.5: Individual sheet flow sediment concentration profiles normalized by sheet thickness. Black line indicates ensemble average of all normalized profiles, white dotted line indicates ODW curve with $\alpha = 1.73$.

time-averaged profiles in oscillatory flows. The small range of values for α indicates a high level of similarity between ensemble-averaged sediment concentration profiles of varying thickness. Therefore, a second ODW curve was compared to the data with α held constant at 1.73, the mean value across all sheet thicknesses. This curve again agreed well with the ensemble-averaged profiles ($R^2 \geq 0.94$; red dotted line in Figure 4.4g,h,i).

The ODW shape is similar to the composite linear-power law profile because the ODW curve has an inflection point, making the curve locally linear in the lower section of the sediment concentration profile, and it reduces to a power law for $z \rightarrow \infty$. The only difference with the composite profile is that the transition between linear and power-law behavior occurs smoothly in the case of the ODW curve. The finding that

α varies relatively little in the ODW curves with α as a fitting parameter indicates that there is a high level of self-similarity between sheet flow sediment concentration profiles of varying sheet thickness. This self-similarity is demonstrated in Figure 4.5, in which all 5365 individual profiles are displayed, scaled by their sheet thickness so that the vertical coordinates equal 0 and 1 at the bottom and top of the sheet flow layer, respectively. The solid black curve indicates the ensemble average of all normalized profiles.

4.4 Sheet Thickness and Sheet Load

Hydrodynamic forcing for unidirectional sheet flow is typically described using the Shields number θ:

$$\theta = \frac{\tau_b}{\rho_f (s-1) g d} \tag{4.9}$$

or the mobility number ψ:

$$\psi = \frac{U^2}{(s-1) g d}, \tag{4.10}$$

where τ_b is the bed shear stress, ρ_f is the fluid density and d is a representative grain diameter which is typically defined as the median grain diameter d_{50}. *Wilson* [1987] proposed a linear relationship between the sheet thickness δ_s and the Shields number:

$$\frac{\delta_s}{d} = \Lambda \theta. \tag{4.11}$$

For stationary flow, *Wilson* [1987] proposed $\Lambda = 10$ whereas *Sumer et al.* [1996] found $\Lambda = 11.8$. Different values for the peak sheet layer thickness under oscillatory flow were proposed ranging from 13 to 35. [e.g., *Dohmen-Janssen et al.*, 2001; *Dong et al.*, 2013].

The bed shear stress τ_b is commonly expressed by a quadratic drag law:

$$\tau_b = \frac{1}{2} f \rho_f U^2, \tag{4.12}$$

where f is a friction factor. The bed shear stress is difficult to determine directly in the swash zone and large uncertainties exist on the value of the friction factor [*Hughes*, 1995; *Puleo and Holland*, 2001; *Conley and Griffin Jr*, 2004; *Raubenheimer et al.*, 2004; *Puleo et al.*, 2012]. Since the mobility number does not depend on the friction factor, it was chosen to represent the hydrodynamic forcing for this section.

The correlation was calculated between mobilized sediment, represented by sheet thickness and sheet load (equation 2.16), and hydrodynamic forcing, represented by the mobility number ψ. Sheet thickness was scaled by d_{50}, similar to previous predictions of sheet thickness as a function of hydrodynamic forcing (equation 4.11), and sheet load was scaled by $d_{50}\rho_s$. During sampling instances when more than one

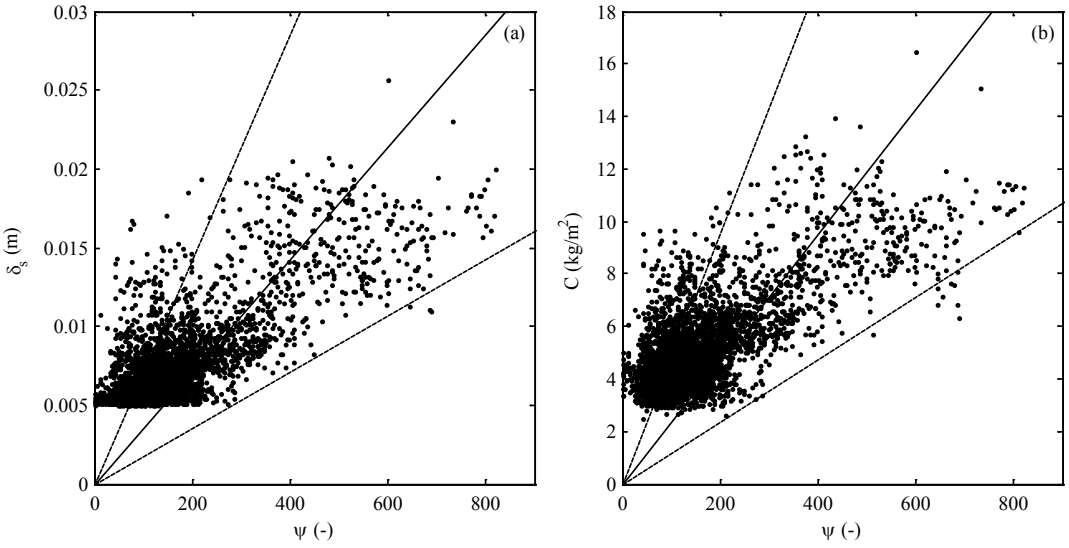

Figure 4.6: (a) Sheet flow thickness δ_s as a function of mobility number ψ, (b) Sheet load C as a function of mobility number ψ. Solid line indicates best fit through origin; dashed lines indicate factor two range. No measurements are displayed with sheet layer thicknesses less than 5 mm as they cannot be resolved by the CCP.

CCP captured the sheet flow layer, the mean of the sheet thicknesses and sheet load measurements from both instruments was used so that a single sampling instance was only counted once in the correlation. Scatter plots displayed in Figure 4.6 show the sheet thickness (a) and sheet load (b) as a function of the mobility number.

The square of the Pearson correlation coefficient r^2 between sheet thickness and mobility number is 0.60, and the correlation coefficient between sheet load and mobility number is 0.53. The relationship between sheet thickness or sheet load and the mobility number was also assessed using a linear fit through the origin (solid line) similar to the linear relation between sheet thickness and Shields number (equation 4.11) proposed by *Wilson* [1987]. The resulting linear fits were:

$$\frac{\delta_s}{d_{50}} = 0.108\,\psi \tag{4.13}$$

$$\frac{C}{d_{50}\rho_s} = 0.0272\,\psi\,. \tag{4.14}$$

The root mean square errors of the linear fits through the origin were 10.2 for the sheet thickness and 2.81 for the sheet load. 73% of all profile measurements were within a factor of two of the fit through the origin (dashed lines) for the sheet thickness and 69% of all profile measurements for the sheet load. The agreements between sheet thickness and mobility number and sheet load and mobility number were similar, because the sheet thickness determined the integration limits for the calculation of the sheet load, and thus calculated sheet thickness and sheet load were highly correlated ($r^2 = 0.96$).

Figure 4.7 reprises the same time series excerpt as in Figure 4.2 and shows time series of the measured mobility number, sheet thickness and sheet load. Sheet layer thickness exceeded 5 mm for five backwash events. Sheet thickness and sheet

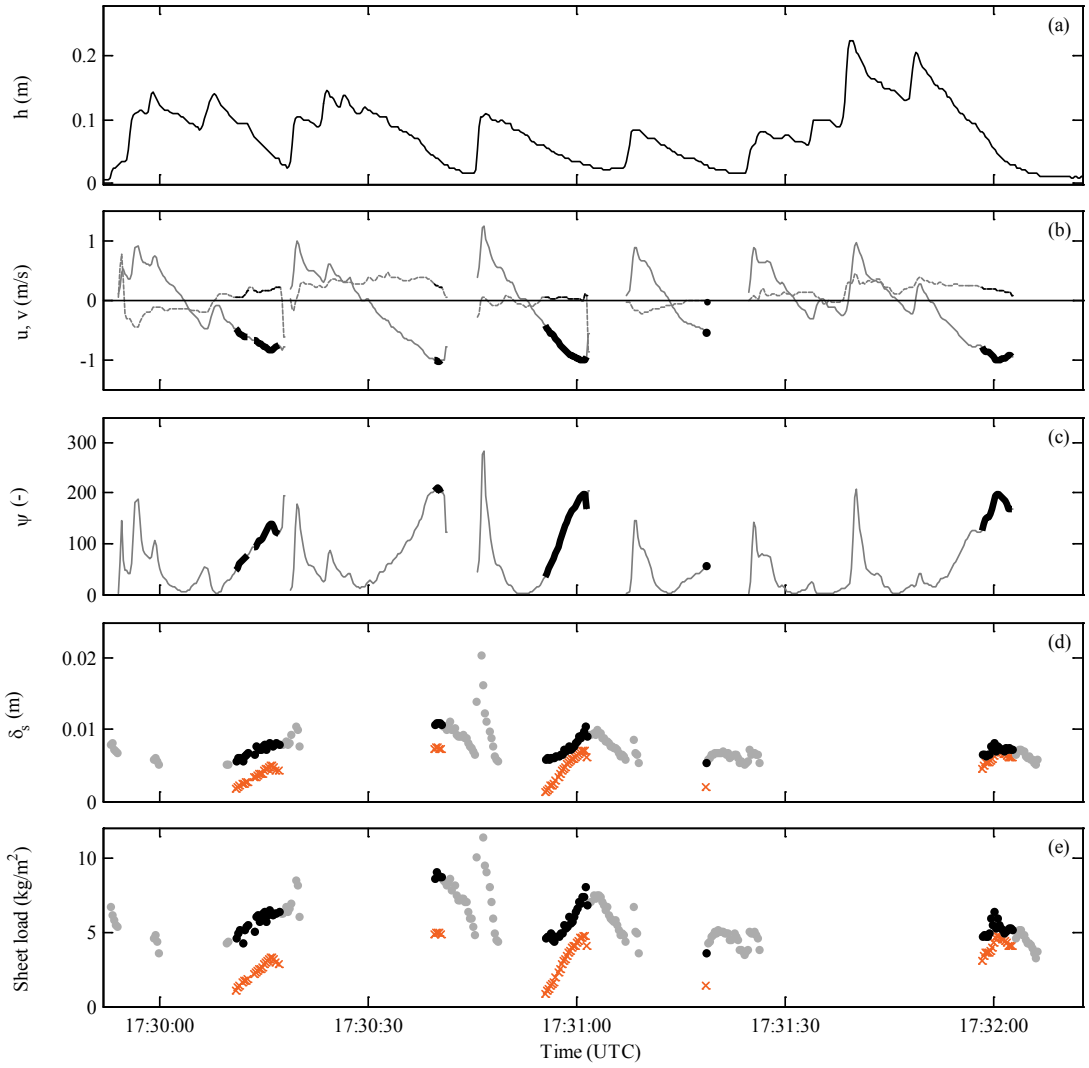

Figure 4.7: Time series excerpt of swash zone measurements. (a) Water depth. (b) Cross-shore (solid line) and alongshore (dashed line) velocity. (c) Mobility number. Thick black lines in panels b and c indicate times when quasi-steady backwash sheet flow occurred. (d) Sheet thickness and (e) sheet load. Black dots indicate measurements during quasi-steady backwash, gray dots indicate measurements during uprush sheet flow events that met quality control criteria and during backwash sheet flow events when no current meter data was available. Orange crosses indicate predictions by fits through origin (equations 4.18-19).

load typically increased monotonically during the backwash as the backwash velocity increased. Measurements at the end of backwash events when the flow depths became smaller than the elevation of the current meter indicate that the sheet thickness decreased at the end of the backwash, when flow velocities also decreased as bottom friction became dominant (e.g., at 17:31:01-17:31:07 UTC). In addition, uprush sheet flow events were also observed, e.g., at 17:30:47 UTC.

Sheet thickness and sheet load were also predicted by the linear fits (4.13-14). These values (orange crosses in Figure 4.7d-e) show that a prediction based on the mobility number alone reproduced the trend of increasing sheet thickness with increasing shear stress. The linear models generally underpredicted measured sheet thickness and sheet load in the time excerpt shown. This is due to the fact that the linear fits were prescribed to intersect with the origin, and because sheet flows with a thickness less than 5 mm are not resolved by the CCP, as seen in the scatter plots in Figure 4.6. Most measurements with $\delta_s \leq 11\ mm$ were underpredicted by the model (Figure 4.6a), as sheet thickness measurements that were overpredicted would likely not be resolved by the CCP. Still, the linear fit through the origin provides the most adequate model for sheet thickness and sheet load because sheet flow layer thickness is zero when no hydrodynamic forcing is present and because it is supported by previous literature [*Wilson*, 1987; *Sumer et al.*, 1996]. With root mean square errors of 8.93 for the sheet thickness and 3.14 for the sheet load for the time series excerpt displayed in Figure 4.7, the agreement with the linear fit is representative for the entire dataset.

4.5 Discussion

The dataset presented here consists of 5365 individual sediment concentration profile measurements from a total of 423 sheet flow events, taken during three high tide cycles. Quality-controlled sheet flow with a sheet layer thickness exceeding 5 mm was recorded during 32 minutes out of 6.5 hours of measurements, meaning that a significant sheet flow layer was present for at least 8 % of the time and probably more, since sheet flow almost certainly also occurred during oblique flows and flows with a free surface level below the current meter that did not meet quality control criteria. This result demonstrates that significant sheet flow frequently occurs in the swash zone.

Backwash flows were deemed quasi-stationary when the measured flow acceleration was below a threshold of $1.2\ g \sin\gamma = 0.27\ m/s^2$. The analysis was repeated with an acceleration threshold reduced by a factor of four to $0.3\ g \sin\gamma = 0.07\ m/s^2$ to verify that flow accelerations below this threshold still had a negligible effect on the sheet flow. This lower threshold reduced the number of measurements that passed quality-control criteria from 3863 to 413. Fitting coefficients in the linear models for sheet thickness and sheet load (equation 4.13-4.14) changed by less than 2%, while the rmse errors for the fits decreased by 5% and 6% respectively. The small variations demonstrate that flow acceleration effects were indeed negligible for the original threshold of $0.27\ m/s^2$.

Backwash sheet flow when the water level was below the elevation of the lowest current meter could have been included in the analysis by estimating the depth-averaged velocity using a continuity technique [*Blenkinsopp et al.*, 2010a, 2010b]. A lidar scanner and an array of ultrasonic distance meters (UDMs) that are capable of generating an estimate of the depth-averaged velocity were deployed during the field

study. However, only velocity measurements by the electromagnetic current meters were used in this chapter because combining velocity measurements from different instruments could provide an additional source of variability in the dataset, and this may obfuscate the relationship between the sheet flow layer thickness and hydrodynamic forcing.

Besides during the backwash, sheet flow was also observed during the uprush, e.g., at 17:30:46 - 17:30:48 UTC in Figure 4.7. Sheet flow during uprush is more difficult to analyze than quasi-steady backwash sheet flow since it is influenced by additional forcing mechanisms such as bore-generated turbulence, pressure gradients and phase lags. For this reason, this chapter focused on sheet flow during quasi-steady backwash conditions.

The sheet flow sediment concentration profile had a linear shape in the lower section of the sheet layer and a power law shape in the upper section of the sheet layer, with the transition between the two shapes occurring at sediment concentrations of 0.20-0.30. The profile was also self-similar for different sheet layer thicknesses. A linear shape, assumed by some sheet flow sediment transport models such as *Hanes and Bowen* [1985] and *Wilson* [1987], was in poor agreement with measured concentration profiles. A curve that incorporates the linear and power law, such as a composite profile or the empirical curve by *O'Donoghue and Wright* [2004a], was in excellent agreement with the field observations.

Adopting a curve such as the combined linear and power law or the empirical curve by *O'Donoghue and Wright* [2004a] can lead to improved sheet flow sediment transport models. For example, *Wilson* [1987] provided an analytical derivation of the sheet thickness by assuming that the bed shear stress τ_b at the bottom of the sheet

layer is balanced by an intergranular shear stress, expressed as a Coulomb failure criterion:

$$\tau_b = \sigma_s \tan\phi' , \tag{4.15}$$

where $\phi'$is the dynamic friction angle of the solids and σ_s is the intergranular normal stress:

$$\sigma_s = \int_{z_e}^{z_t} \rho_f g(s-1)c(z)dz . \tag{4.16}$$

Wilson [1987] assumed a linear concentration profile $c(z)$ in the sheet layer and a sediment concentration of zero at the top of the sheet layer, yielding:

$$\sigma_s = \rho_f g(s-1)\frac{\delta_s}{2} c_b . \tag{4.17}$$

Combining (4.15) and (4.17) yields

$$\frac{\delta_s}{d} = \frac{2}{c_b \tan\phi'} \frac{\tau_b}{\rho_f g(s-1)d} = \frac{2}{c_b \tan\phi'}\theta = \Lambda\theta . \tag{4.18}$$

Wilson [1987] assumed $c_b = 0.625$ and $\tan\phi' = 0.32$, leading to $\Lambda = 10$. Assuming a linear law with a power-law tail at the top of the sheet flow layer instead leads to higher values for Λ. For example, evaluating σ_s using the ODW curve with α =1.73 (equation 4.7) and assuming $c_t = 0.08$ at the top of the sheet layer leads to $\Lambda = 11.8$, the same value as found by Sumer *et al.* [1996]. The exact value of Λ is also influenced by assumptions on the sediment concentration in the bed c_b and the dynamic friction angle ϕ', but the improved description of the shape of the concentration profile nevertheless leads to sheet thickness estimates that are in better agreement with previous measurements.

Sheet thickness has previously been predicted as a linear function of the Shields number (equation 4.11). Because of the difficulty in determining the bottom shear stress in the swash zone, sheet thicknesses and sheet load were related to the

mobility number ψ in this study. The mobility number ψ can be related to the Shields number θ when a constant friction factor is assumed:

$$\theta = \frac{1}{2} f \psi \,, \tag{4.19}$$

By using equation (4.19), the linear fit between mobility number and the sheet flow layer thickness based on the dataset analyzed in this study is equivalent to the linear law for steady flow based on the Shields number (equation 4.11) with $\Lambda = 11.8$ [*Sumer et al.*, 1996] when a friction factor $f = 0.018$ is assumed. Velocity profile measurements in the bottom boundary layer during high tide 7, assuming a logarithmic velocity profile, yielded $f = 0.021 \pm 0.012$ during backwash flows [*Puleo et al.*, 2014b]. The small difference between the friction factor estimates indicates that the sheet thickness measurements found here are in good agreement with past predictions based on the Shields number. This result, however, does not contravene the fact that there is still significant scatter associated with field measurements of bed shear stress, friction factors and sheet flow layer thicknesses in the swash zone, as illustrated by the scatter in Figure 4.6 for sheet layer thickness and the standard deviation in the friction factor estimate based on velocity measurements. Additionally, sheet thickness values may vary between different studies because they were based on different measurement techniques, e.g. concentration measurements [e.g. *Sumer et al.*, 1996; *Dohmen-Janssen and Hanes*, 2005, this study] or visual methods [e.g. *Dong et al.*, 2013] or because they were based on different definitions for the top and bottom boundary of the sheet flow layer.

Laboratory measurements have shown that sheet flow initiates above a threshold Shields number of 0.5 – 1.0 [*Nielsen*, 1992; *Asano*, 1995] or a threshold mobility number of approximately 240 [*Dingler and Inman*, 1976]. Including a

threshold value in the linear models (equations 4.13 - 4.14), similar to the threshold value in the bedload transport formula by *Meyer-Peter and Müller* [1948], could therefore yield a more accurate representation of the relationship between sheet thickness, sheet load and the mobility number. A threshold value was not included in the linear models (equations 4.13 - 4.14) to facilitate comparison with existing relationships between sheet thickness and bed shear stress that also do not include a threshold value, such as the relationships proposed by *Wilson* [1987] and *Sumer et al.* [1996]. In addition, accurately resolving a threshold value would require measurements of small sheet thicknesses near the threshold but these were not resolved by the sensor.

Sheet load magnitudes of up to 14 kg/m^2 were frequently observed during quasi-steady backwash events. Suspended loads of up to 4 kg/m^2 were observed in a preliminary analysis of fiber-optic backscatter sensor (FOBS) measurements during high tide 7 and were typically O(1-10) times smaller than concurrent sheet load magnitudes [*Puleo et al.*, 2014b], indicating that near-bed sediment loads are not negligible in the swash zone.

4.6 Conclusions

Sediment concentration profiles in the sheet flow layer were measured in the swash zone of a dissipative beach using three conductivity concentration profilers, providing the first detailed measurements of sheet flow under field conditions. This chapter focused on sheet flow during quasi-steady backwash conditions when the effects of surface-generated turbulence, phase lags and pressure gradients on the sheet flow layer were negligible, simplifying the hydrodynamic forcing for the sheet flow. From 6.5 hours of measurements spanning three high tides, 16 minutes of sheet flow

was recorded during quality controlled, quasi-steady backwash conditions, providing a dataset of 5365 instantaneous sediment concentration profiles.

The concentration profiles were grouped according to sheet flow layer thickness and ensemble-averaged. The sheet flow sediment concentration profile had a linear shape in the lower section and a power-law shape in the upper section, with the transition between the two shapes occurring at sediment volume fractions of 0.20-0.30. The profile shape was self-similar for sediment concentration profiles of varying sheet thicknesses ranging from 6 mm to 18 mm and can be described by a curve based on *O'Donoghue and Wright* [2004a]. Adopting this curve as the sediment concentration profile provides an improvement to the analytical model for sheet flow layer thickness developed by *Wilson* [1987]. This linear-power law curve shape also has significance toward future models of nearbed sediment transport where the sediment concentration profile in the sheet flow layer requires parameterization.

The sheet flow layer thickness and sheet load were well-correlated to the hydrodynamic forcing represented by the mobility number ψ, with $r^2 = 0.60$ for the sheet layer thickness and $r^2 = 0.53$ for the sheet load. A simple model with the nondimensional sheet thickness and sheet load proportional to the mobility number provided a good prediction of a time series of sheet thickness and sheet load.

Chapter 5

TURBULENCE DISSIPATION

Turbulence is a key factor in swash-zone hydrodynamics and sediment transport: the balance between uprush (onshore-directed) and backwash (offshore-directed) transport may not be explained without accounting for bore turbulence [*Puleo et al.*, 2000; *Butt et al.*, 2004; *Aagaard and Hughes*, 2006]. Highly-resolved velocity profile measurements were collected during the BeST field study (Chapter 3). The purpose of this chapter is to estimate the turbulence dissipation rate based on these velocity measurements using the structure function, in order to investigate 1) temporal variability of the turbulence dissipation rate and its relationship to image-based observations of wave breaking, 2) the decay of turbulence dissipation following bores, 3) the structure of the vertical dissipation profile and its implications toward turbulence generation mechanisms, 4) the dependence of the turbulence dissipation rate on forcing parameters such as (tidally modulated) local water depth and offshore wave height and 5) the relative importance of turbulence dissipation and density stratification in the TKE budget.

5.1 Introduction

Few field measurements of the turbulence dissipation rate ϵ have been performed in the swash zone because of measurement difficulties [*Flick and George*, 1990; *Rodriguez et al.*, 1999; *Raubenheimer et al.*, 2004] and most of the present knowledge on swash zone turbulence stems from laboratory [e.g. *Petti and Longo*,

2001; *Cowen et al.*, 2003; *O'Donoghue et al.*, 2010; *Sou et al.*, 2010] and numerical [e.g. *Zhang and Liu*, 2008; *Torres-Freyermuth et al.*, 2013] studies. More field measurements of the dissipation rate are available in the surf zone, where velocimeters are continuously submerged. Measured surf zone dissipation rates may provide an indication of the expected range of dissipation rates in the swash zone. Dissipation rates obtained from field experiments in the surf and swash zones ranged from $O(10^{-7}m^2/s^3)$ to $O(10^{-1}m^2/s^3)$ (Table 5.1). Measured dissipation rates follow a lognormal distribution [*George et al.*, 1994] and can vary by up to 3 orders of magnitude within a single field study, highlighting the variability of turbulence dissipation.

Turbulence in the swash zone is generated locally by bores (broken waves) and by bed shear. Turbulence generated by breaking waves in the surf zone is also advected into the swash zone, meaning that swash-zone turbulence dissipation exceeds local production and the swash zone acts as a sink for surf-zone turbulence [*Sou et al.*, 2010]. The relative importance of breaking-wave and bed-generated turbulence can be assessed from the vertical dissipation profile. Seaward of the surf zone, *Feddersen et al.* [2007] observed that the dissipation profile had a maximum near the surface (due

Table 5.1: Surf and swash zone dissipation estimates.

Source	$\epsilon(m^2/s^3)$	H_s (m)		Bottom slope	Location
Flick and George [1990]	$1 \cdot 10^{-2} - 4 \cdot 10^{-2}$	Unspecified		Unspecified	Surf
George et al. [1994]	$5 \cdot 10^{-5} - 5 \cdot 10^{-2}$	0.50-1.20	(offshore)	0.025	Surf
Veron and Melville [1999]	$1 \cdot 10^{-3}$	0.7-1.8	(offshore)	0.03	Surf
Trowbridge and Elgar [2001]	$1 \cdot 10^{-5} - 2 \cdot 10^{-4}$	0.50-2.6	(offshore)	0.01	Surf
Bryan et al. [2003]	$3 \cdot 10^{-7} - 3 \cdot 10^{-3}$	0.10-0.62	(local)	0.01-0.06	Surf
Grasso et al. [2012]	$2 \cdot 10^{-4} - 6 \cdot 10^{-3}$	1.0-8.0	(offshore)	0.025	Surf
Feddersen et al. [2012a]	$1 \cdot 10^{-4} - 1 \cdot 10^{-3}$	0.02 - 0.95	(local)	0.01	Surf
Feddersen et al.[2012b]	$1 \cdot 10^{-4} - 2 \cdot 10^{-3}$	0.5 - 1.7	(local)	0.02-0.05	Surf
Raubenheimer et al. [2004]	$4 \cdot 10^{-2} - 1 \cdot 10^{-1}$	0.55-1.0	(offshore)	0.02	Swash

to whitecapping) and a secondary maximum near the bed (due to bed shear). In the surf zone, dissipation is largest near the surface, indicating that wave breaking is dominant [*George et al.*, 1994; *Huang et al.*, 2009; *Grasso et al.*, 2012]. In the swash zone, bed-generated turbulence is dominant during the backwash phase. During the uprush phase, (advected) surface-generated turbulence is dominant, though bed-generated turbulence may still be significant [*Petti and Longo*, 2001; *Sou et al.*, 2010]. As expected, bed-generated turbulence is more pronounced in swash experiments over rough beds than over smooth beds [*O'Donoghue et al.*, 2010].

Bryan et al. [2003] and *Raubenheimer et al.* [2004] observed that turbulence dissipation decreases with increasing mean water depth in the surf and the swash zones. *Bryan et al.* [2003] also found that ϵ is negatively correlated to $h\gamma/H_s$ where h is the mean water depth, H_s is significant wave height and γ is an empirical wave breaking parameter, $\gamma = (H_s/h)_{breaking}$. Conversely, *Grasso et al.* [2012] did not detect a significant depth dependence for ϵ in the surf zone, but did find ϵ to be dependent on wave skewness, asymmetry, and on H_{tot}/h, where H_{tot} is the total significant wave height including infragravity waves. *Cowen et al.* [2003] showed that for both spilling and plunging monochromatic breakers, Eulerian measurements of turbulence dissipation decay rapidly after bore arrival following a $t^{-2.3}$ decay rate, the same rate as freely decaying isotropic grid turbulence. In the case of grid turbulence, the turbulent kinetic energy (TKE) decays as $t^{-1.3}$ and ϵ decays as $t^{-2.3}$ since the turbulent kinetic energy budget reduces to $\epsilon = -\frac{d(TKE)}{dt}$ [*Pope*, 2000]. In a numerical study of swash flows, *Zhang and Liu* [2008] confirmed that the TKE decays as $t^{-1.3}$ for strong bores, but that it decays slower, as $t^{-0.65}$, for weak bores. For deep-water breaking waves, *Rapp and Melville* [1990] estimated a dissipation decay rate as $t^{-2.5}$

whereas *Veron and Melville* [1999] observed a rate of t^{-n} with n ranging between 1 and 1.25.

5.2 Methodology

5.2.1 Existing Analysis Methods

The turbulence dissipation rate can be calculated directly from the fluctuating strain rate tensor when the velocity field is quantified in two dimensions, e.g. using Particle Image Velocimetry (PIV) in the laboratory [*Cowen et al.*, 2003; *Sou et al.*, 2010]. Other methods, such as those based on the wavenumber spectrum, the structure function and the frequency spectrum employ the Kolmogorov hypotheses to estimate the dissipation rate from the structure of the velocity field. *Veron and Melville* [1999] collected one-dimensional velocity profiles using a pulse-to-pulse coherent acoustic Doppler velocity profiler (ADVP) and estimated the dissipation rate based on the one-dimensional wavenumber spectrum, which takes the form

$$E(k) = \alpha \epsilon^{2/3} k^{-5/3}\,, \tag{5.1}$$

in the inertial subrange, where k is the wavenumber and $\alpha = 1.5$ is an empirical coefficient [*Pope*, 2000]. Another approach based on one-dimensional velocity profiles is the structure function [*Kolmogorov*, 1991]. For the vertical velocity component w, the second-order longitudinal structure function D is defined as

$$D(z,r,t) = \langle \left(w'(z+r,t) - w'(z,t)\right)^2 \rangle \tag{5.2}$$

where r is the separation distance, t is time and $\langle ... \rangle$ denotes time averaging. The structure function takes the form

$$D(z,r,t) = C\ \epsilon(z,t)^{2/3} r^{2/3} \tag{5.3}$$

in the inertial subrange, where $C = 2.0$ is an empirical constant [*Pope*, 2000]. The structure function has thus far only been applied to oceanic environments in water depths greater than several meters such as tidal channels, river mouths and dense bottom plumes [*Wiles et al.*, 2006; *Mohrholz et al.*, 2008; *Whipple and Luettich*, 2009].

Many field studies of nearshore hydrodynamics collect only one or a small number of point measurements of the velocity field and employ Taylor's frozen turbulence hypothesis to obtain a dissipation estimate from the (temporal) frequency spectrum. For a stationary current,

$$P_{ww}(f) = \frac{24}{55}(2\pi)^{-2/3}\alpha\epsilon^{2/3}V^{2/3}f^{-5/3} \tag{5.4}$$

in the inertial subrange, where $P_{ww}(f)$ is the frequency spectral density of the vertical velocity, f is frequency, and V is the advection velocity (similar expressions exist for the other velocity components). *Lumley and Terray* [1983] extended Taylor's hypothesis to the case of nearshore turbulence advected by wave orbital motions and a stationary current [extended further by *Trowbridge and Elgar*, 2001; *Bryan et al.*, 2003; *Feddersen et al.*, 2007; *Gerbi et al.*, 2009]. Estimating turbulence dissipation based on frequency spectra has a number of limitations compared to estimates based on spatial velocity measurements. For example, *Veron and Melville* [1999] found that the dissipation rate calculated using the frequency spectrum and Taylor's hypothesis was overestimated by a factor of 4 compared to the dissipation rate calculated from the same dataset using the wavenumber spectrum. Secondly, frequency spectra are typically estimated using velocity time series with a duration on the order of minutes, precluding analysis of the temporal variability of ϵ on a wave time scale [O(10 s)]. Velocity time series in the swash zone are discontinuous due to the intermittent flow

coverage, meaning that a frequency spectrum based on a long-duration time series cannot be readily generated. Moreover, swash flows on dissipative beaches are often dominated by infragravity motion, making it difficult to separate mean and orbital flow velocities. *George et al.* [1994] avoided this problem by computing frequency spectra over short time intervals with a duration of 0.125 s. Dissipation estimates by *George et al.* [1994] may have been overestimated because they did not account for the bias introduced by using a small number of points in the spectral estimate [*Bryan et al.*, 2003].

5.2.2 Laboratory Validation

The wavenumber spectrum, frequency spectrum and structure function are illustrated and compared using an idealized laboratory test case under a stationary flow. The test was conducted in a recirculating flume with a test section width of 0.40 m and depth of 0.46 m. A single layer of rock with a diameter of approximately 0.04 m was placed over a length of 1.6 m of the flume bottom to increase bottom roughness and enhance turbulence production. Velocity profiles were collected by a pulse-coherent acoustic Doppler profiling velocimeter of the same type as used in the BeST field study [Nortek Vectrino-II Profiler; *Craig et al.*, 2011]. The velocimeter measured a vertical profile of all three velocity components (*u, v, w)* over a range of 0.030 m with a profile resolution of 0.001 m (31 points) using a central acoustic emitting transducer and four receiving transducers, and was deployed with the velocity profiling section located 0.12 m – 0.15 m above the flume bottom (~ 0.08 m – 0.11 m above the roughness elements). A velocity record of 1393 s (23.2 minutes) was collected at a sampling rate of 100 Hz. Mean streamwise flow velocities varied from

Table 5.2: Turbulence dissipation rate estimates for stationary flow laboratory test.

ϵ $(10^{-4}\ m^2\ s^{-3})$	Structure function	Wavenumber spectrum	Frequency spectrum	Frequency spectrum (95% high)	Frequency spectrum (95% low)
w_1	2.04	2.07	1.95	2.74	1.44
w_2	2.10	1.85	1.77	2.49	1.31

0.62 – 0.68 m/s across the sampled section of the boundary layer. Resulting turbulence dissipation estimates are summarized in Table 5.2.

For similar acoustic velocimeters with three receiving transducers in a downward-facing setup, noise levels of the measured horizontal velocity components are approximately 31 times higher than the vertical velocity component due to the transformation of the along-beam velocity components to the velocity components in a Cartesian coordinate system [*Voulgaris and Trowbridge*, 1998]. Based on the velocity transformation matrix for a Vectrino-II probe geometry with four receiving transducers, the ratio of horizontal velocity noise levels to vertical velocity noise levels ranges from 10 to 16 along the measured velocity profile. Having lower noise levels, vertical velocity measurements were used for turbulence estimates in this study [see also *Huang et al.*, 2012]. Two independent estimates of the vertical velocity, w_1 and w_2, were derived from the four receiving transducers: w_1 was estimated from transducers located on prongs of the velocimeter that were oriented perpendicular to the flow and w_2 from transducers on prongs that were aligned with the flow. The difference between w_1 and w_2 was used to assess the instrument accuracy.

To calculate the dissipation rate based on the structure function, vertical velocity fluctuations w' were computed by subtracting the time-averaged vertical velocity from the vertical velocity time series

$$w'(z,t) = w(z,t) - \langle w(z,t) \rangle \tag{5.5}$$

For each elevation bin z_i in the velocity profile and each separation distance r_j, the velocity differences in the structure function were implemented using the central differences method:

$$D(z_i, r_j, t) = \langle \{ w'(z_i + r_j/2\,, t) - w'(z_i - r_j/2\,, t) \}^2 \rangle\,. \tag{5.6}$$

$D(z_i, r_j, t)$ was then fitted to

$$D(z_i, r_j, t) = N + A r_j^{\frac{2}{3}}\,. \tag{5.7}$$

where N and A are fitting parameters. A is indicative of the rate at which the velocity field decorrelates with separation distance due to turbulence and N is indicative of measurement (Doppler) noise [*Wiles et al.*, 2006]. Following *Wiles et al.* [2006], ϵ was obtained from equation (5.7) as

$$\epsilon = \left(\frac{A}{C}\right)^{3/2}. \tag{5.8}$$

For the laboratory test, the structure function $D(z, r)$ was calculated for the center bin of the vertical velocity profile and the time averages in equations (5.5-6) were calculated over the entire 23.2-minute velocity record (Figure 5.1a). The structure function followed an $r^{2/3}$ law for separation distances r up to 0.023 m ($R^2 = 0.96$); velocity records for larger separation distances were rejected by velocimeter quality control criteria (Section 5.3). Deviations from the $r^{2/3}$ law were larger for w_2 than for w_1.

The wavenumber spectrum $E(k)$ was calculated for the top 30 bins in the velocity profile (since an even number of points was needed for the Fourier transform) for each of the 139264 instantaneous profiles. Individual profiles were detrended but not tapered or band averaged. Instantaneous wavenumber spectra were then time-averaged to obtain a smooth wavenumber spectrum (Figure 5.1b). The wavenumber

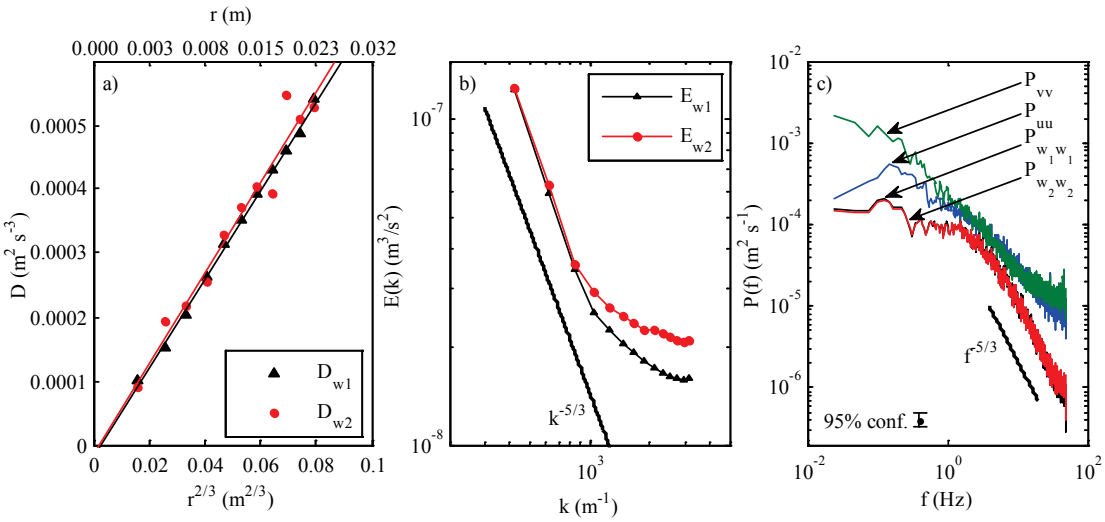

Figure 5.1: a) Structure function D for vertical velocity estimates w_1(triangles) and w_2 (circles). Solid lines indicate fits of equation (7). b) Wavenumber spectrum averaged over 24-minute record. c) Temporal frequency spectrum. Error bar indicates 95% confidence band of spectral estimate.

spectrum displays a $k^{-5/3}$ slope, indicative of the inertial subrange, and a noise floor. A larger noise level is again observed for w_2. The noise floor was estimated as the spectral energy level at the largest resolved wavenumber. ϵ was then calculated from equation (5.1) by averaging $(E(k) - \text{noisefloor})k^{5/3}$ over the inertial subrange $(300 \leq k \leq 1100)$.

The one-sided frequency spectrum was calculated for all three velocity components at the center bin of the vertical velocity profile using Welch's method, by dividing the velocity records into 67 detrended segments with 50% overlap, tapered using a Hamming window (169 degrees of freedom; Figure 5.1c). The frequency spectra of both vertical velocity estimates are in good agreement. The inertial subrange, with a frequency decay of $f^{-5/3}$, was observed over a large range of frequencies in the vertical velocity components, but was obscured in the horizontal

velocity components by the higher noise level. The turbulence dissipation rate was calculated from the measured frequency spectrum using the frozen turbulence hypothesis. The noise floor was calculated as the average spectral energy level for $f \geq 47\ Hz$ and ϵ was calculated from equation (5.4) by averaging $(P_{ww}(f) - \text{noisefloor})f^{5/3}$ over the inertial subrange ($4 \leq f \leq 20$) [similar method as *Trowbridge and Elgar*, 2001 and *Raubenheimer et al.*, 2004]. The noise floor of the horizontal velocity components was 12 times larger than the noise floor of the vertical components, in agreement with estimates based on the transformation matrix of the velocimeter. The dissipation rate was also calculated for the high and low limits of the 95% confidence band of the frequency spectrum (Table 5.2).

The larger deviations in the structure function for w_2 and the higher noise floor in the wavenumber spectrum are both indications that vertical velocity measurements w_2 (derived from transducers located on prongs that were aligned with the flow) had a higher noise level than w_1 (derived from transducers located on prongs that were perpendicular to the flow). Despite the higher noise level, dissipation estimates derived from w_1 and w_2 are in good agreement for all three methods. The difference between dissipation rates estimated from the three methods is on the same order of magnitude as the difference between dissipation rates estimated from the two independent estimates of the vertical velocity, w_1 and w_2, indicative of the instrument accuracy (Table 5.2). Dissipation estimates based on the structure function and wavenumber spectrum approaches also fell within the dissipation estimates based on the 95% confidence interval of the frequency spectrum. The agreement between the three methods in the controlled laboratory experiment indicates that the structure

function is a valid method to estimate the turbulence dissipation rate from the field measurements using this velocimeter.

5.2.3 Field Experiment and Data Processing

Velocity measurements were collected during the BeST field study (see Chapter 3 for a full description of the field site) using three Nortek Vectrino-II pulse-coherent acoustic Doppler profiling velocimeters of the same type as used in the laboratory validation (Section 5.2.2). As in the laboratory test case, the velocimeters collected vertical profiles of all three velocity components over a range of 0.030 m with a resolution of 0.001 m. A coordinate system was defined with the x-axis in the cross-shore direction with values increasing onshore, the y-axis in the alongshore direction with values increasing to the north and the z-axis in the vertical direction with values increasing upwards. A local vertical datum $z = 0$ m was defined at the bed level below the velocimeters at the beginning of each high-tide measurement cycle. Flows occurred at elevations lower than $z = 0$ m since the bed frequently eroded below this level over the course of a measurement cycle.

The three velocimeters were deployed at the same cross-shore location with alongshore offsets of approximately 0.20 m (Figure 5.2). The elevation of the sensors was chosen so that the profiling section of the three velocimeters was positioned at nominally -0.01 m $\leq z \leq$ 0.02 m, 0.015 m $\leq z \leq$ 0.045 m and 0.04 m $\leq z \leq$ 0.07 m respectively at the beginning of each tide. Velocities were sampled at 100 Hz with measurements synchronized across all velocimeters. The water level at the velocimeter location was recorded at 4 Hz with a Druck PTX1830 pressure transducer buried 0.05 m below the bed. The bed became continuously inundated as the water

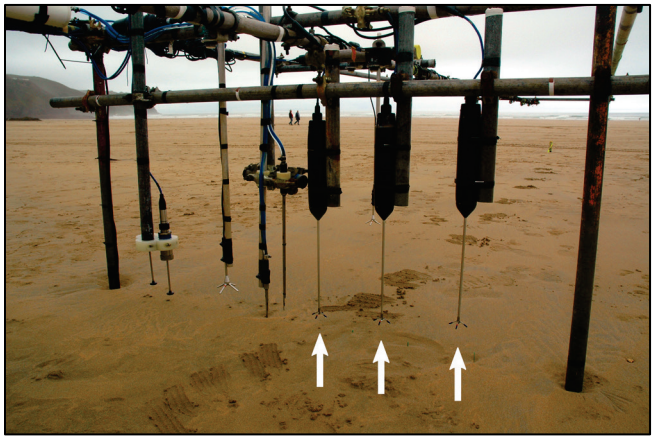

Figure 5.2: Main instrument rig with three profiling velocimeters indicated by white arrows.

level approached its maximum at high tide, meaning that both swash zone and inner surf zone conditions are contained in the dataset.

Bed level changes of up to 0.03 m were observed at minute timescales near the instrument array during the field study. Frequently updated estimates of the bed level were therefore necessary to correctly situate velocity measurements with respect to the bottom boundary. The lowest velocimeter performed a bottom scan based on the reflected amplitude of an acoustic pulse transmitted and received by the center transducer of the velocimeter at a sampling rate of 2 Hz (interleaved with velocity measurements). The reflected amplitude was acquired at $1 \cdot 10^{-3}$m resolution for elevations of $-3 \cdot 10^{-2}$ m $\leq z \leq 3 \cdot 10^{-2}$ m. The bed eroded below the scanning range during several tidal cycles. Dissipation estimates when the bed level was below the scanning range were not retained in the analysis of the vertical dissipation rate profile (section 5.3.3). Bed levels estimated using the center beam reflection showed

good overall agreement with bed levels estimated from the velocity profile, which approaches zero at the non-moving bed due to the no-slip condition.

Velocity records were quality-controlled by rejecting samples with a reflected beam amplitude below -40 dB or an instrument correlation score below 50%, or when the water level measured by the pressure transducer was below the velocimeter probe. Spikes were then removed from the velocity record using the phase-space despiking method [*Goring and Nikora*, 2002; *Wahl*, 2003]. Quality control based on a combination of a correlation score cut-off and phase-space despiking was chosen because turbulence statistics are better preserved by a phase-space despiking method [*Mori et al.*, 2007]. However, the phase-space despiking method alone was not sufficient to remove all spikes from the velocity record since it was developed for quasi-stationary flows that are less variable and less prone to bubble contamination than swash flows. Gaps of up to 10 samples (0.1 s) in the quality-controlled velocity record were closed using linear interpolation [*Elgar et al.*, 2005]. An extensive discussion of quality-control of ADV data for calculating turbulence dissipation is given by *Feddersen et al.* [2010]. The quality-control criteria proposed by *Feddersen et al.* [2010] are specific to the frequency spectrum method and were therefore not used here.

The structure function $D(z_i, r_j, t)$ and the fit to equation (5.7) were calculated at time intervals of 1.25 s for each of the two independent measurements of vertical velocity w_1 and w_2. Time averaging in equations (5.5-6) was performed over a 2.5 s window, leaving a 50% overlap in the time averaging segments. Velocity profiles from the three velocimeters were not combined into a single profile to calculate $D(z_i, r_j, t)$ since velocity differences between sensors due to the alongshore offset

artificially increase $D(z_i, r_j, t)$. Instead, fits of equation (5.7) were made for velocity profiles from each velocimeter individually. Dissipation estimates were rejected when the structure function was determined for less than 5 values of r_j (in order to make a robust fit of equation 5.7), if more than 20% of the velocity values in the 2.5 s time average did not meet quality control criteria, or if the goodness-of-fit of equation (5.7), characterized by the coefficient of determination R^2, was less than 0.70. For an elevation bin z_i, the central differences technique then required at least 5 velocity time series from elevation bins above and below z_i. Therefore, $D(z_i, r_j, t)$ was only calculated for the central 21 bins of each 31-bin velocity profile. As a result, ϵ was estimated at elevations down to $5 \cdot 10^{-3}$ m above the bed level and there was a $5 \cdot 10^{-3}$ m gap between the vertical dissipation profiles from the different velocimeters. R^2-values for the structure function fit (equation 5.7) exceeded 0.70 for 89% of all dissipation estimates in the entire dataset, indicating that the $D \sim r^{2/3}$ structure function scaling [equation (5.3)] was generally valid under field conditions. A single time-series of the vertical-averaged dissipation rate $\bar{\epsilon}$ was defined as the average of all available ϵ values in the vertical dissipation profile measured by the three velocimeters. $\bar{\epsilon}$ does not equal the depth-averaged dissipation rate (defined over the entire water column) since the velocimeters captured only the lower 0.065 m (nominally) of the water column.

A Sony DFW-X710 IEEE1394 visible-band camera with a 1024 x 768 pixel array was deployed on a 4 m tower on the dune ridge. During tide 5, the camera recorded 5-minute image sequences at 5 frames per second every 15 minutes during daylight hours, for a total of 25 minutes of video. Video collection was only

Figure 5.3: Example image of the video collection, including location of pixel intensity time series points and timestack transect. Image brightness and contrast was enhanced compared to raw image for increased visibility.

successful during tide 5 due to limited daylight hours and unfavorable weather conditions during other tidal cycles. Images were converted to grayscale and geo-referenced using surveyed ground control points [*Holland et al.*, 1997]. Each image sequence was geo-referenced to the vertical elevation of the mean water level during the 5-minute sequence to account for rising water levels during the 1.25 hours when imagery was collected. The brightness variability in the image set due to varying cloud cover was compensated by histogram equalization of each image to a constant reference image. Two products were derived from the image set: a pixel intensity time series, calculated as the mean pixel intensity of 5 pixels at the cross-shore location of the velocimeters and a cross-shore pixel intensity timestack, defined as the pixel

intensity on a shore-normal transect (Figure 5.3). Pixels where the instrumentation scaffolding blocked the view of the water surface were removed from the transect. Pixel intensities were normalized from 0 (zero intensity; black) to 1 (maximum intensity; white).

5.3 Results

5.3.1 Time Series Excerpt

A time series excerpt of measurements collected during tide 5 is displayed in Figure 5.4, showing an infragravity-timescale swash event with a duration of 117 s. The bed level (black line in panels d and e) varied from $z = -0.01$ m to $z = -0.015$ m. As in the entire dataset, high goodness-of-fit values were found for the structure function fit (Figure 5.4d). Poorer agreements between the measured structure function and the $D \sim r^{2/3}$ scaling were mostly confined near the bed. Several cycles of uprush (onshore-directed motion) and backwash (offshore-directed motion) with durations between 10 s and 25 s occurred during the excerpt, superimposed on infragravity motion that reached a maximum free surface elevation η = 0.50 m (Figure 5.4a,b). Velocity and dissipation rate measurements were frequently interrupted upon bore arrival (flow reversal from negative to positive velocity) due to air bubbles entrained by the bores, potentially obscuring large turbulence dissipation rates (gaps in Figure 5.4b-e). The dissipation rate was typically largest following bore arrival (e.g. at t = 52 s; 85 s), then decayed rapidly (see Section 5.3.2), and increased again during the backwash (e.g. t = 16 s; 66 s; 100 s). Measured turbulence dissipation rates in the excerpt varied between $4 \cdot 10^{-5}$ m^2/s^3 and $6 \cdot 10^{-3}$ m^2/s^3. In the entire dataset, 99% of the dissipation rate measurements fell between $6 \cdot 10^{-5}$ m^2/s^3 and $8 \cdot$

10^{-3} m^2/s^3. Little variability was observed between mean dissipation estimates from the three velocimeters, deployed with 0.025 m vertical offsets, indicating that the turbulence was well-mixed over this small vertical range (Figure 5.4c,e). No

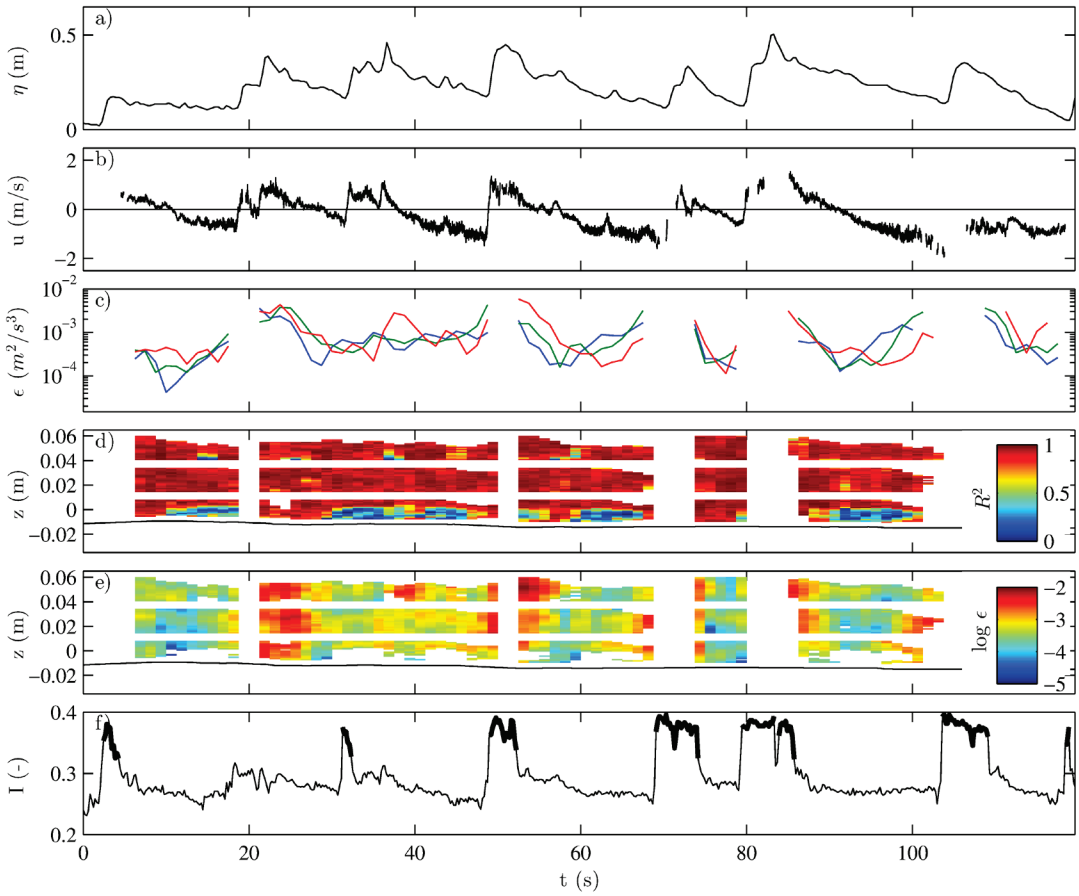

Figure 5.4: Time series excerpt of measurements taken during tide 5 at 16:33:10 – 16:35:10 UTC on 12 October 2011. a) Free surface elevation η. b) Cross-shore velocity at z = 0.02 m. c) Turbulence dissipation estimates averaged across the vertical for lower (blue line), middle (red line) upper (green line) velocimeter. d) Coefficient of determination R^2 of equation (5.7) fit. e) Base-10 logarithm of turbulence dissipation ϵ. Black line in panels d and e indicates bed level estimate from velocimeter bed level scan. f) Normalized pixel intensity from video camera. Thick black lines indicate high pixel intensity events.

distinguishable trend was observed in the dissipation rate on infragravity timescales. Figure 5.4f displays the normalized pixel intensity time series I obtained from the video imagery. Inspection of the grayscale images showed that the baseline pixel intensity ($I \approx 0.27$) in the time series corresponded with the sea surface when no breaking occurred. High pixel intensity events, defined as instances when the pixel intensity exceeded a threshold value of $I = 0.32$, were indicative of aerated wave breaking or remnant foam (thick black lines in Figure 5.4f) [*Aarninkhof and Ruessink*, 2004; *Haller and Catalán*, 2009]. Several high pixel intensity events occurred during the excerpt ($t \approx 3\text{ s}, 33\text{ s}, 50\text{ s}, 71\text{ s}, 83\text{ s}, 107\text{ s}$), often coinciding with interruptions in the velocity measurements (since air bubbles both caused high pixel intensities in the video observations and disrupted the acoustic velocity measurements). The surface signature of bores is also visible in the pixel intensity timestack corresponding to the time series excerpt (Figure 5.5). Shoreward-propagating bores are seen as high pixel intensity (white) diagonal streaks in the timestack. High pixel intensity events in the pixel time series (Figure 5.4f and black transect line in Figure 5.5) were associated with bores that propagated over tens of meters and generated a rapid increase in the free surface elevation time series (Figure 5.4f). Another peak in the dissipation rate time series occurred at $t = 21\ s$. Free surface and cross-shore velocity time series (Figure 5.4a,b) indicate that this dissipation event was associated with a propagating wave but the surface signature of the wave is not visible in the local pixel intensity time series (Figure 5.4f). The timestack shows that a broken wave indeed propagated onshore, but lost most of its surface signature before it reached the location of the velocimeters. This illustrates that broken waves may still carry significant turbulence dissipation even after the pixel-intensity surface signature has disappeared.

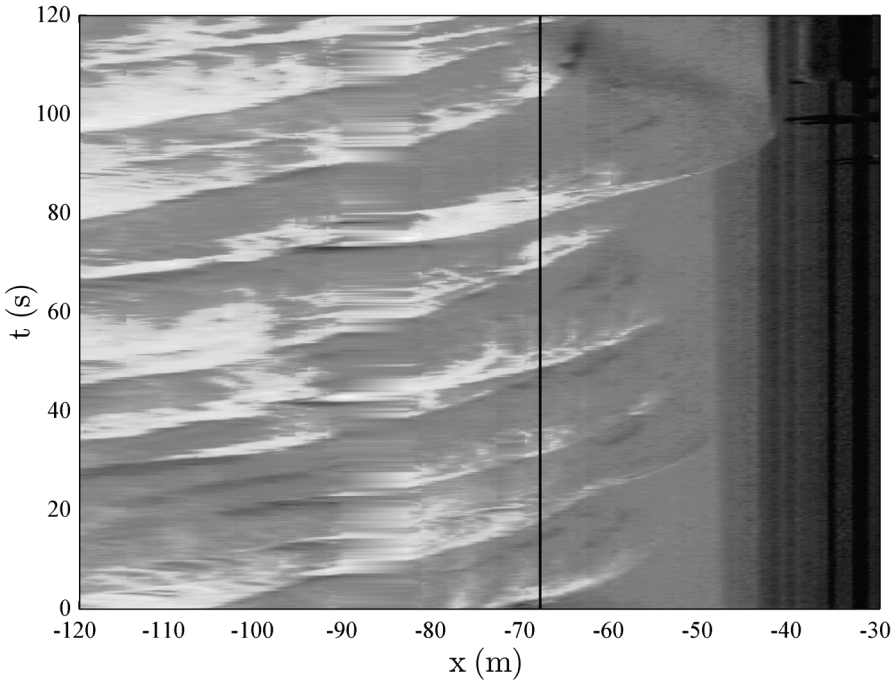

Figure 5.5: Pixel intensity timestack. Black line indicates cross-shore position of the velocimeters.

Despite the interruptions in the dissipation time series due to bubbles, the relationship between in situ-measured dissipation rates and remotely-sensed pixel intensities is still demonstrable. During the 25 minutes when video imagery was recorded, vertically-averaged in-situ dissipation rates $\bar{\epsilon}$ that occurred during a high pixel intensity event or up to 0.5 s after a high pixel intensity event were 1.8 times larger than dissipation rates occurring outside of high pixel intensity events, a significant difference at the 99% level. Conversely, of the 5% highest $\bar{\epsilon}$ values measured during video collection, 57% occurred during, or up to 0.5 s after, a high pixel intensity event.

5.3.2 Dissipation Decay Rates

Turbulence dissipation following swash-zone bores has been shown to decay at a rate similar to grid turbulence [*Cowen et al.*, 2003; *Zhang and Liu*, 2008]. Grid turbulence is characterized by unidirectional flow passing through a grid obstacle that produces a large amount of turbulence. Beyond the grid, there is no additional turbulence production and the turbulence in the center of the flow decays freely, without interacting with the flow boundaries. The analogous case in the swash zone is turbulence decaying freely after being generated by a bore. Several factors may complicate the decay behavior of bore-generated turbulence in natural conditions with irregular wave forcing. Bores and non-breaking waves with various heights propagate shoreward at different time intervals and may interact with each other, and bed shear may cause additional turbulence production. Still, turbulence dissipation rates were observed to decay rapidly after bore arrival (e.g. t = 24 s, 52 s, 85 s, 110 s in Figure 5.4).

Isolated bore events were selected to study the simplest case of the decay of turbulence dissipation. An isolated bore event consists of a rapid water level increase (bore arrival), followed by a gradual water level decrease (backwash) with no interaction with secondary bores. Figure 5.6 displays a 180 s time series excerpt that included 3 isolated bore events (Figure 5.6a). Even in the swash zone, incident-band wave events do not necessarily start or end with a dry bed (zero water depth) since bores propagate superimposed on infragravity motions. An isolated bore event was identified when a rise in free surface elevation of more than 0.08 m was detected in a timespan of two seconds or less (bore arrival). The event start time t_0 was defined at the center of the water level increase (Figure 5.6a, dots). The bore event was retained until a new increase was observed in the free surface elevation time series, i.e. when

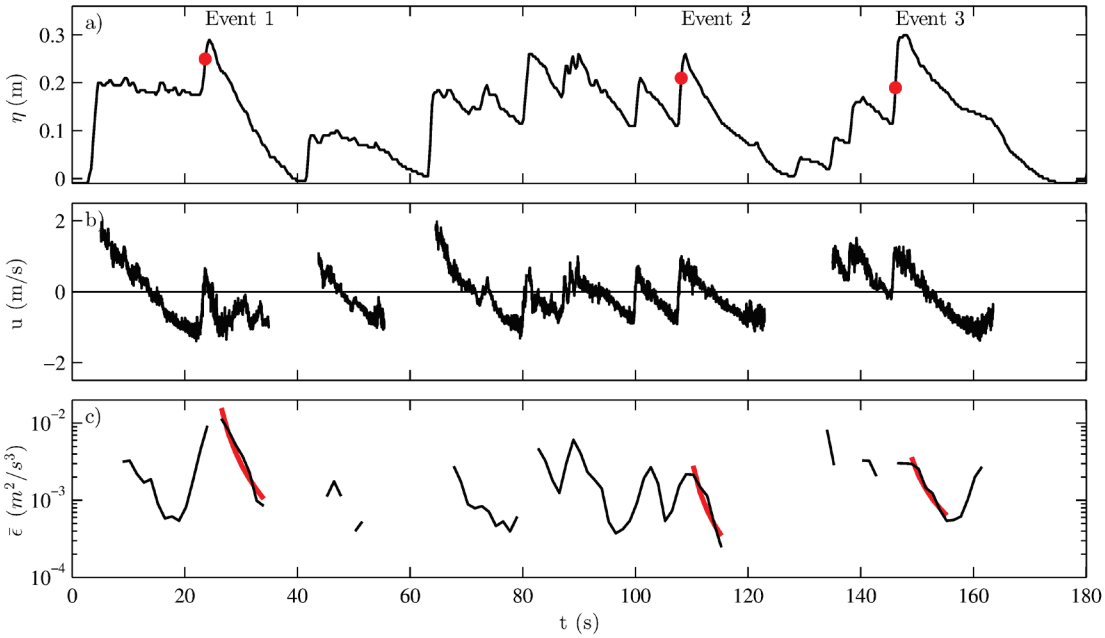

Figure 5.6: Time series excerpt of turbulence dissipation decay rates, recorded during tide 8 at 06:28:56 – 06:31:58 UTC on 14 October 2011. a) Free surface elevation η. Dots indicate start times t_0 for three bore-dissipation events. b) Cross-shore velocity measured at 0.02 m above the bed. c) Measured vertically-averaged dissipation rate $\bar{\epsilon}$ and fitted decay rates according to equation (5.9). R^2 goodness-of-fit was 0.92, 0.87 and 0.94 for the three events, respectively.

$\frac{dh}{dt} > 0.01$ m/s (indicative of a secondary bore or wave which may alter the free turbulence dissipation decay). Bore events with a duration of less than 7 s seconds were not utilized in the analysis so that a minimum of 5 $\bar{\epsilon}$ estimates were made during the bore decay. The selection criteria for simple bore events were based only on the water level time series so that no a priori assumptions on the velocity or turbulence field were made. A total of 468 simple bore events were retained from the 10 tidal cycles.

The decay of turbulence dissipation starts once the bore has passed the sensor location (no more turbulence production due to the bore) and the turbulence is vertically distributed across the water column. The depth-averaged dissipation rate $\bar{\epsilon}$ was therefore analyzed for each of the isolated bore events from 2 seconds after the start time of the event until the minimum dissipation rate was reached (end of the decay). A power-law decay curve similar to grid turbulence decay was fit to the vertical-averaged dissipation rate:

$$\bar{\epsilon}(t) = \bar{\epsilon}_0 \left(\frac{t}{t_0}\right)^n \tag{5.9}$$

where $\bar{\epsilon}_0$ and n are free fitting parameters. The grid-dissipation law showed excellent agreement to the measured dissipation rate $\bar{\epsilon}$ for the three bore events displayed in Figure 5.6 ($R^2 = 0.92, 0.87$ and 0.94, respectively). The decay exponent *n* for event 1, 2 and 3 was -0.78, -2.00 and -1.76 respectively. Event 2 and 3 display a clear uprush and backwash phase in the cross-shore velocity time series (Figure 5.6b). In contrast, the velocity during event 1 was almost exclusively negative (offshore-directed) meaning that event 1 consisted of a bore propagating shoreward against an infragravity-timescale backwash. This explains why the value of *n* for event 1 was strongly different from event 2 and 3 and from the value for grid turbulence (*n = -2.3).* During event 3, the dissipation rate began to increase again toward the end of the backwash ($t \approx 160\ s$), which was likely due to bed-generated turbulence. The mean R^2 for all 468 events was 0.81, with 70% of all bore events exhibiting a good fit to the decay model ($R^2 > 0.80$). The mean decay exponent n was -1.94 (standard deviation 0.44) for events with $R^2 > 0.80$.

5.3.3 Vertical Dissipation Rate Profiles

The vertical dissipation profile provides an indication of the dominant turbulence production mechanisms. However, instantaneous dissipation profiles are prone to noise and an appropriate averaging mechanism is needed to generate characteristic turbulence dissipation profiles. Unlike laboratory studies of swash flows generated by regular wavetrains or dambreaks, the velocity and free surface elevation time series in the field study were irregular and strongly influenced by infragravity-timescale motions. It was therefore difficult to combine swash events for ensemble-averaging. Instead, the vertical structure of the turbulence dissipation field was analyzed by phase space averaging (PSA) [*Puleo et al.*, 2003; *Foster et al.*, 2006b]. Eulerian velocity measurements of a purely sinusoidal wave follow an elliptical trajectory in the two-dimensional phase space of cross-shore velocity and acceleration. Binning dissipation measurements under an irregular wave train according to the measured velocity and acceleration is analogous to wave phase-averaging. The cross-shore velocity time series at the center bin of the velocity profile measured by the top velocimeter profile (nominally at z = 0.055 m) was smoothed by convolution in time with a Tukey window with a width of 101 samples (1.01 seconds) and a shape factor of 0.5 in order to create a free-stream velocity time series $u_\infty(t)$ and an acceleration time series $\frac{du_\infty(t)}{dt}$. Measured vertical profiles were grouped in velocity bins with bin widths of 0.5 m/s and centers at -1.5 m/s; -1.0 m/s; -0.5 m/s; 0.0 m/s; 0.5 m/s and 1.0 m/s and acceleration bins with bin widths of 0.5 m/s^2 and centers at -0.75 m/s^2; -0.25 m/s^2; 0.25 m/s^2; and 0.75 m/s^2 (Figure 5.7). All vertical dissipation profiles were referenced with respect to the elevation above the instantaneous bed level z' at the time of the dissipation measurement, $z' = z - z_{bed}(t)$. Dissipation profiles were not included when the bed level could not be determined or when no dissipation rates

were available for the lowest 0.01 m of the water column. Fluctuations in the bed level z_{bed} meant that gaps between turbulence dissipation profiles from the three velocimeters (Figure 5.4e) occurred at different elevations above the bed, so that no gaps occurred in the combined profiles after phase-space averaging. The average number of dissipation measurements *N* for each phase space-averaged vertical profile is displayed in each panel. Points were not included in the profile when less than 50 individual dissipation estimates were combined in the average.

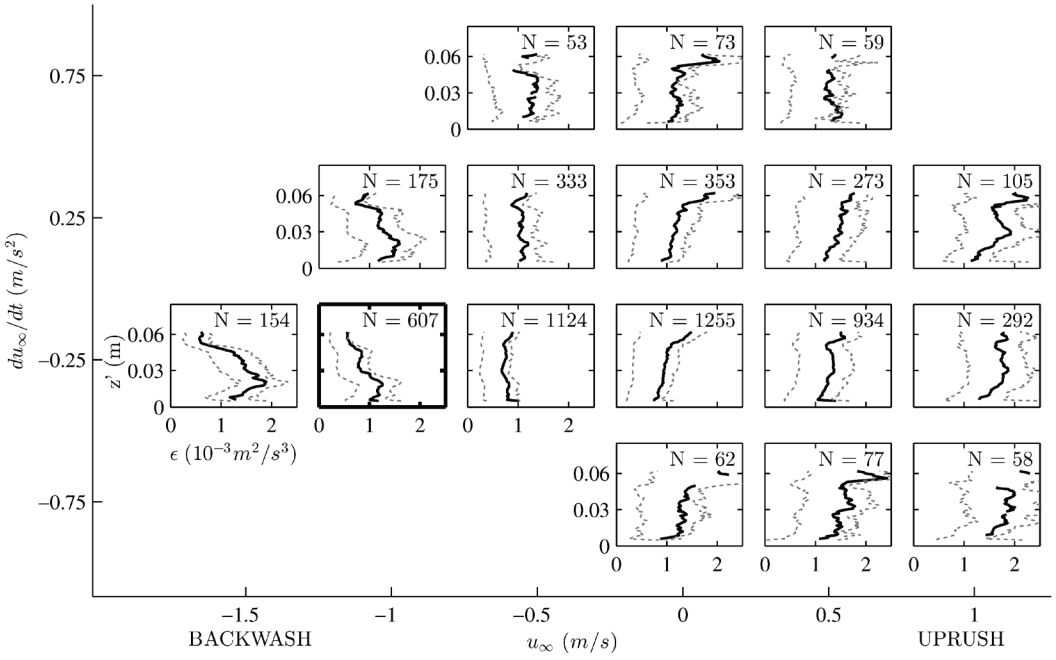

Figure 5.7: Phase space averaged vertical dissipation profiles (black solid line) and 25% and 75% percentiles of averaged profiles (gray dotted lines). Axes labels and scales are identical for all panels. Downslope gravitational acceleration corresponds to $\frac{du_\infty(t)}{dt} = -0.22\ \mathrm{m/s^2}$. N-values indicate average number of dissipation rates used in the vertical profile. Panel indicated by bold frame was compared against log-layer scaling (Section 5.4.4).

Swash-zone velocity time series typically display a sawtooth shape with a roughly constant acceleration equal to the downslope gravitational acceleration. The downslope gravitational acceleration $-g \sin\beta$ was $-0.22\ \mathrm{m/s^2}$ with the beach slope β of 1:45 around the velocimeters and the gravitational acceleration $g = 9.81\ \mathrm{m/s^2}$. As a result, the largest number of measurements in the dataset occurred in the acceleration bin $\frac{du_\infty(t)}{dt} \approx -0.25\ \mathrm{m/s^2}$ (third row in Figure 5.7). Dissipation rates were higher during the uprush than during the backwash by 6%-106% for equivalent acceleration and velocity bins. For example, dissipation rates in the uprush bin $\left(u_\infty \approx 0.50\ \mathrm{m/s}\ , \frac{du_\infty}{dt} \approx -0.25\ \mathrm{m/s^2}\right)$, were 70% larger than in the corresponding backwash bin $\left(u_\infty \approx -0.50\ \mathrm{m/s}\ , \frac{du_\infty}{dt} \approx -0.25\ \mathrm{m/s^2}\right)$. Dissipation rates increased upwards during the uprush ($u_\infty > 0\ \mathrm{m/s}$), indicative of surface-generated turbulence. Conversely, dissipation rates during strong backwash conditions ($u_\infty \leq -1\ \mathrm{m/s}$) decreased upwards, indicative of bed-generated turbulence. The transition from surface-dominated dissipation to bed-dominated dissipation occurred when $u \approx -0.5$ m/s, indicating that the early stages of backwash were still dominated by surface processes. It is noted that only near-bed ($0\ \mathrm{m} \leq z' \leq 0.06\ \mathrm{m}$) dissipation rates were measured. Dissipation rates higher in the water column, and particularly above the wave trough level, may have been larger than the near-bed dissipation rates. For this reason, no attempt was made to compare the near-surface turbulence dissipation rate profile to surf-zone scalings such as proposed by *Feddersen et al.* [2012b].

5.3.4 Wave Height and Water Depth Dependence

Wave height and the (tidally modulated) local water depth are two potentially influential factors to the average turbulence dissipation rate. Offshore significant wave heights decreased from 2.46 m to 0.56 m over the course of the study

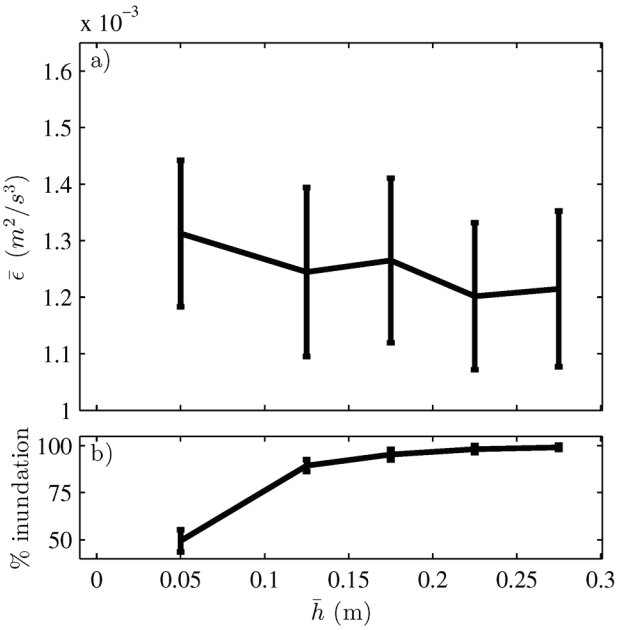

Figure 5.8: a) Turbulence dissipation as a function of local water depth. b) Inundation percentage. Error bars show variability (1 standard deviation) between results from 10 tide measurement cycles.

(Table 3.1). However, the turbulence dissipation rate, averaged over both the vertical profile and in time over each high tide measurement cycle was not significantly correlated with the mean offshore wave height (Pearson correlation coefficient r = 0.15). Similarly, no significant correlation was found between the tidally-averaged turbulence dissipation rate and the offshore wave energy, represented by H_{rms}^2 (r = 0.05). The study site was a dissipative beach where wave breaking occurred over several wavelengths, indicating a saturated surf zone (Figure 5.3). Wave energy in the gravity-wave band (wave period less than 20 s) in a saturated surf zone is depth-limited and roughly independent of offshore wave forcing [*Thornton and Guza*, 1982].

The local water depth $\bar{h}$, defined as the 30-minute running average of the water depth recorded by the pressure transducer, varied over the course of the rising and

falling tide and peaked at 0.23-0.42 m during the different tides. Vertically-averaged turbulence dissipation values were binned according to depth with bin widths of 0.05 m. Measurements for the two smallest depth bins, $\bar{h} < 0.1$ m, were combined because of the small number of valid measurements. Turbulence dissipation rates (Figure 5.8) remained roughly constant in the inner surf zone ($\bar{h} > 0.20$ m) and increased with decreasing water depth in the swash zone ($\bar{h} < 0.20$ m). However, there was considerable variability among the 10 tidal cycles as demonstrated by the error bars (1 standard deviation). Distributions of vertically-averaged dissipation rates for the different depth bins show that dissipation rates followed a lognormal distribution for all depths with a similar shape among the different tidal cycles (Figure 5.9). Within each depth bin, $\bar{\epsilon}$ varied by approximately 2 orders of magnitude, consistent with earlier studies (Table 5.1).

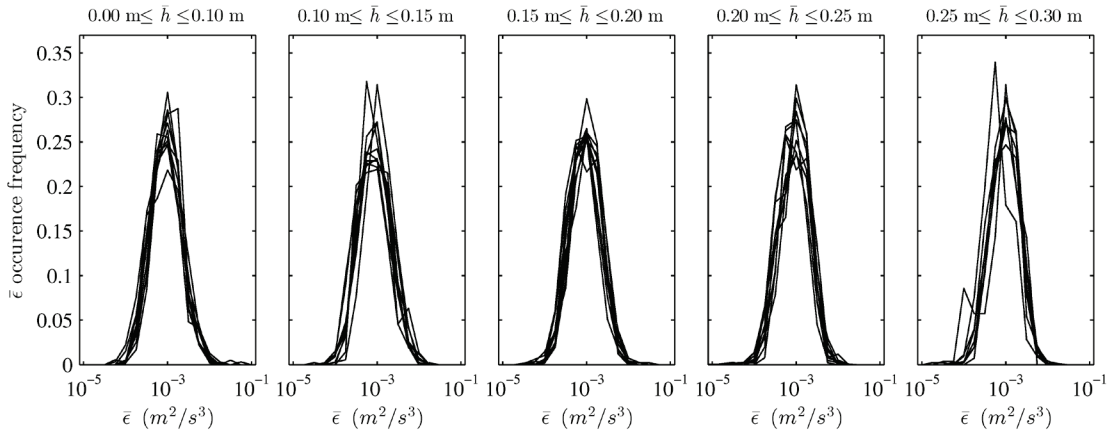

Figure 5.9: Distributions of turbulence dissipation rates binned according to local water depth. Different curves display results from the 10 tide measurement cycles.

5.4 Discussion

5.4.1 Analysis Methods

Turbulence dissipation rates calculated from the structure function, the wavenumber spectrum, and the frequency spectrum showed excellent agreement in an idealized laboratory test case. The structure function was chosen to analyze the field data for several reasons. Estimating the dissipation rate based on the frequency spectrum invokes the frozen turbulence hypothesis, which has a number of disadvantages (see Section 5.1). In the laboratory test case, the wavenumber spectrum displayed the inertial subrange for only 4 points and over less than one order of magnitude of $E(k)$ before flattening to a noise floor (Figure 5.1). In contrast, the structure function followed the inertial subrange over 11 data points, meaning that a more robust fit can be performed to estimate ϵ. Furthermore, the structure function $D(z_i, r_j, t)$ can be calculated at different elevations z_i to estimate the vertical dissipation profile, while the wavenumber spectrum cannot be calculated at different elevations unless the number of points used to calculated the spectrum is halved to 16 (leaving only 8 points in the one-sided wavenumber spectrum). Lastly, calculating either the wavenumber or the frequency spectrum introduces spectral leakage, whereas the structure function is calculated directly from the measured vertical velocity profile.

The time averaging window of 2.5 s, used in equations (5.5-6) to calculate *D*, was chosen as a compromise between achieving a robust estimate of the time-averaged quantities and maintaining sufficient resolution to resolve the temporal evolution of ϵ (e.g. the rapid decay of bore-generated turbulence). The sensitivity to the choice of time averaging window length was examined by repeating the analysis with a larger (3.5 s) and smaller (1.5 s) averaging window for tide 5 (Figure 5.10).

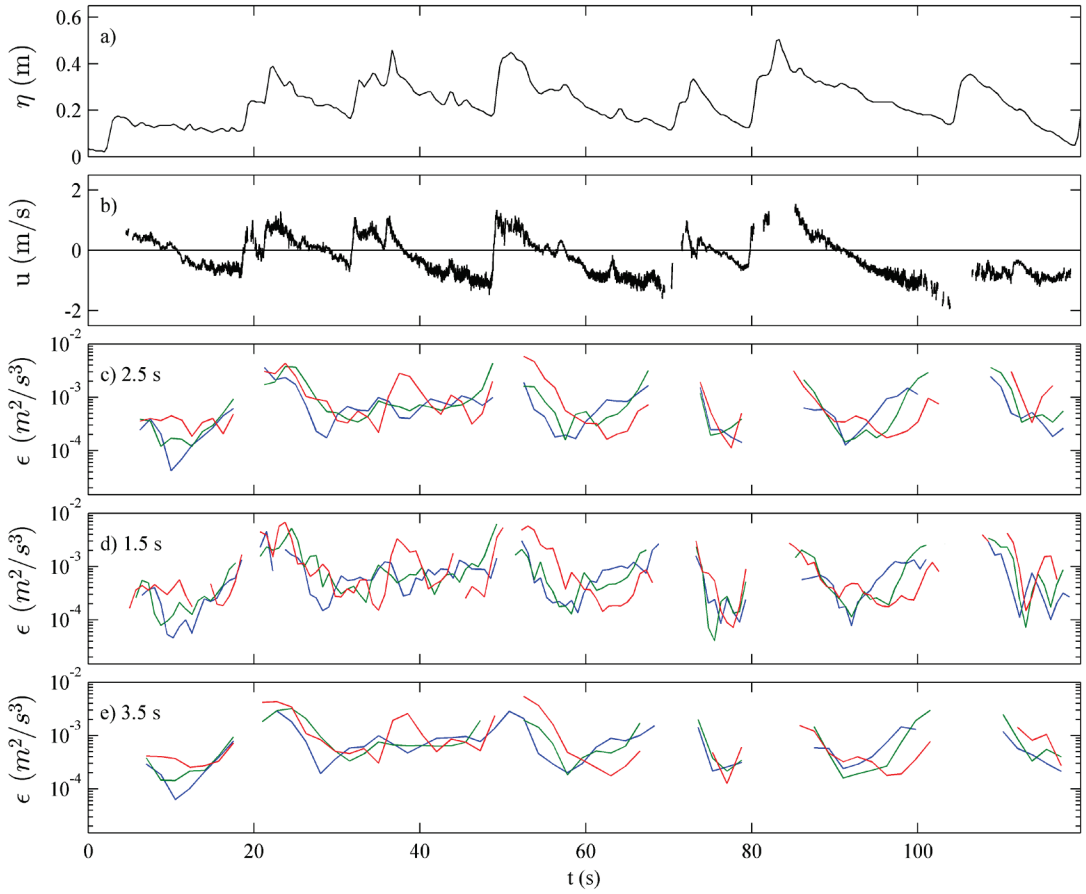

Figure 5.10: Repeat of time series excerpt displayed in Figure 5.4. Time series excerpt of measurements taken during tide 5 at 16:33:10 – 16:35:10 UTC on 12 October 2011. a) Free surface elevation η. b) Cross-shore velocity at z = 0.02 m. c-e) Turbulence dissipation estimates calculated using an averaging window of 2.5 s (c), 1.5 s (d) and 3.5 s (e) averaged across the vertical for lower (blue line), middle (red line) upper (green line) velocimeter.

Calculating D and ϵ with a 3.5 s averaging window led to reduced noise in the ϵ timeseries but certain features in the timeseries were smoothed out due to the reduced temporal resolution. Conversely, reducing the averaging window to 1.5 s improved the temporal resolution but increased the noise in the dissipation rate time series. The

overall effect of varying the averaging window between 1.5 s and 3.5 s was small and general trends in the ϵ timeseries were identical, meaning that dissipation rate estimates were not overly sensitive to the choice of the averaging window length. Mean vertical velocities in the swash zone are small so the effect of subtracting the mean velocity (equation 5.6) is likely to be small as well [*Aagaard and Hughes*, 2006].

The $D \propto \epsilon^{2/3} r^{2/3}$ scaling for the structure function (equation 5.3) is only valid in the inertial subrange, defined by $l_k \ll r \ll l_e$ where l_k is the Kolmogorov length scale and l_e is the length scale of the largest eddies. The separation distance *r* used to calculate *D* (equation 5.6) ranged between $2 \cdot 10^{-3}$ m and $3 \cdot 10^{-2}$ m and dissipation rates between $6 \cdot 10^{-5}$ $\mathrm{m^2/s^3}$ and $8 \cdot 10^{-3}$ $\mathrm{m^2/s^3}$ were found. The Kolmogorov length scale, defined as $l_k = \sqrt[4]{\frac{\nu^3}{\epsilon}}$ [*Pope*, 2000] (with $\nu = 1.15 \cdot 10^{-6}$ $\mathrm{m^2/s}$ as the kinematic viscosity of water at 15 °C), ranged between $1.18 \cdot 10^{-4}$ m and $4.0 \cdot 10^{-4}$ m, an order of magnitude smaller than r. The length scale of the largest eddies has been estimated in the swash zone as the distance between the measurement location and the bed [*Flick and George*, 1990] and as 0.4 times the local water depth [*Sou et al.*, 2010]. The dissipation rate was measured at elevations from 0.005 m up to roughly 0.065 m above the bed and when local water depths were between 0.07 m and 0.85 m. The separation distance r was therefore always smaller than the largest eddy length scale l_e. As a result, the calculated structure function fell within the inertial subrange meaning that the application of equation (5.3) was valid, as is demonstrated by the high R^2 values (Figure 5.4). The separation distances for ϵ estimates near the bed were of the same size as the largest eddy length scale, which may explain the occasionally lower R^2 values near the bed.

5.4.2 Dissipation Rate Magnitude

Observed instantaneous dissipation rates ranged between $6 \cdot 10^{-5}$ m^2/s^3 and $8 \cdot 10^{-3}$ m^2/s^3 with a mean dissipation rate of $1.2 \cdot 10^{-3}$ m^2/s^3 to $1.3 \cdot 10^{-3}$ m^2/s^3 depending on local water depth. Turbulence dissipation rates were measured in the swash zone and in the inner surf zone in both the BeST field study and in the field study by *Raubenheimer et al.* [2004]. Dissipation rates observed during the BeST field study were an order of magnitude smaller than swash-zone dissipation rates reported by *Raubenheimer et al.* [2004]. However, inner surf zone dissipation rates observed in the BeST study are of same order of magnitude as rates observed throughout the surf zone in other studies, whereas those observed by *Raubenheimer et al.* [2004] are higher than most previously reported values (Table 5.1). The differences in observed dissipation values in different studies are likely due to differences in the field site morphologies (e.g. beach slope), offshore wave forcing, sensor position in the water column and due to the different methods used to estimate ϵ.

5.4.3 Vertical Dissipation Profile

The dissipation rate increased upwards during the uprush, indicating that bore-generated turbulence was likely the dominant mechanism, and decreased upwards during backwash, indicating that bed-generated turbulence was dominant. In a laboratory study, *Sou et al.* [2010] observed that dissipation profiles decreased upwards during both the uprush and the backwash in the swash zone, but the near-bed dissipation profile increased upwards during the uprush in the inner surf zone, near the boundary with the swash zone. Other laboratory studies of swash zone turbulence displayed only vertical profiles of turbulent kinetic energy (TKE), not ϵ. Although

TKE and ϵ are not equivalent, these profiles still provide a useful indication of the dominant processes. *Petti and Longo* [2001] found a similar structure for the vertical TKE profile in a laboratory study as observed for ϵ in this chapter. *O'Donoghue et al.* [2010] found that TKE was nearly depth-uniform on a smooth beach slope, but that it decreased upwards during both the uprush and the backwash for a rough beach with a much larger grain size ($d \approx 5 \cdot 10^{-3}$m) than the study site discussed here ($d_{50} = 0.33 \cdot 10^{-3}$ m), highlighting the importance of bed roughness in the balance between bed-generated and surface-generated turbulence. In summary, vertical turbulence dissipation profiles observed in this study are generally consistent with previously observed profiles.

5.4.4 Turbulence Damping by Density Stratification

If turbulence dissipation was dominated by bed-generated turbulence during the backwash, the vertical dissipation profile may have followed the "log-layer" scaling [*Tennekes and Lumley*, 1972]. The log-layer scaling assumes that turbulence production $\mathcal{P}$ is balanced by dissipation:

$$\epsilon = \mathcal{P} = \frac{u_*^3}{\kappa z\prime} \tag{5.10}$$

where $u_* = \sqrt{\frac{\tau_b}{\rho_f}}$ is the friction velocity, τ_b is the bed shear stress, $\rho_f = 1025$ kg/m^3 is the fluid density and $\kappa = 0.41$ is the von Kármán constant. Dissipation rates in the surf zone were found to be greater than the log-layer prediction due to breaking-wave generated turbulence, even under strong alongshore flows [*Feddersen et al.*, 2007; *Grasso et al.*, 2012]. The log-layer dissipation scaling was examined for the phase-space-averaged backwash bin -1.25 m/s $\leq u_\infty \leq -0.75$ m/s, -0.50 m/s$^2 \leq$

$\frac{du_\infty}{dt} \leq 0\ \mathrm{m/s^2}$ (panel indicated by bold frame in Figure 5.7). The friction velocity was estimated using a quadratic drag law:

$$u_* = \sqrt{\frac{\tau_b}{\rho_f}} = \sqrt{\frac{\frac{1}{2}\rho_f f u_\infty^2}{\rho_f}} \tag{5.11}$$

The backwash friction factor *f* was estimated for this field dataset from log-law velocity profiles as $f = 0.021$ [*Puleo et al.*, 2014b], yielding $u_* = 0.1\ \mathrm{m/s}$. Based on this friction velocity estimate, the log-layer turbulence dissipation estimate [equation 5.10)] for $z' = 0.04$ m is $\epsilon = 6.6 \cdot 10^{-2}\mathrm{m^2/s^3}$, two orders of magnitude larger than the measured dissipation rate of $8.1 \cdot 10^{-4}\mathrm{m^2/s^3}$ (Figure 5.7).

The large discrepancy between measured dissipation rates and rates predicted by the log-law scaling may be partially due to uncertainties in the friction factor, the elevation above the bed *z'* of the velocity measurements, because the flow acceleration $\frac{du_\infty}{dt}$ was not zero or because the turbulence may have still been developing (production larger than dissipation) throughout the backwash. Another factor in the balance between turbulence production and dissipation is sediment-induced density stratification [*Ross and Mehta*, 1989; *Winterwerp*, 2001; *Hsu and Liu*, 2004]. The swash zone is characterized by some of the highest sediment concentrations found in the coastal environment and vertical sediment concentration gradients near the bed of $O(\frac{-10\frac{kg}{m^3}}{0.01\ m} = -1000\ \mathrm{kg/m^4})$ have been observed [*Puleo et al.*, 2000; *Aagaard and Hughes*, 2006]. Suspended sediment concentrations were measured at different elevations during this field study but the quality of the measurements was not sufficiently consistent to obtain a detailed spatio-temporal overview of suspended sediment concentration throughout the 10 tidal cycles. However, a detailed

investigation of suspended sediment concentrations on the same beach as the BeST study [*Masselink et al.*, 2005] showed a mean concentration profile $c(z')$ of

$$c(z') = 71\,\mathrm{kg/m^3} \cdot \exp\left(-\frac{z'}{0.023\mathrm{m}}\right) \tag{5.12}$$

during the backwash, yielding $\frac{dc}{dz} = -5.4 \cdot 10^2\ \mathrm{kg/m^4}$ and $\frac{d\rho}{dz} = \frac{\rho_s - \rho_f}{\rho_s}\frac{dc}{dz} = -3.3 \cdot 10^2\ \mathrm{kg/m^4}$ at $z' = 0.04$ m, with $\rho_s = 2650\ \mathrm{kg/m^3}$ the sediment density and ρ the density of the fluid-sediment mixture. A preliminary analysis of vertical suspended sediment concentration gradients observed during the BeST field study displayed similar magnitudes [*Puleo et al.*, 2014b]. An order-of magnitude estimate of the turbulence damping due to density stratification *S* was calculated as

$$S = \frac{\nu_t}{\rho \sigma_c}\frac{d\rho}{dz}g \tag{5.13}$$

where ν_t is the eddy viscosity and $\sigma_c = 0.7$ is the Prandtl-Schmidt number [*Winterwerp*, 2001; *Hsu and Liu*, 2004]. The eddy viscosity was calculated consistent with the log-law scaling as $\nu_t = \kappa z u_*$. With $\frac{d\rho}{dz}$ estimated using the result by *Masselink et al.* [2005], the stratification term *S* was $-7.5 \cdot 10^{-3} m^2/s^3$, an order of magnitude larger than the measured turbulence dissipation ϵ. The importance of density stratification was also assessed using the gradient Richardson number [*Turner*, 1979]:

$$Ri = \frac{\frac{1}{\rho}\frac{\partial \rho}{\partial z}g}{\left(\frac{\partial u}{\partial z}\right)^2}. \tag{5.14}$$

The phase-space-averaged velocity profile $u(z)$ is displayed in Figure 5.11. The vertical velocity gradient $\frac{du}{dz}$ at 0.04 m was estimated at $-3.2\ s^{-1}$. The Richardson number was then $Ri = 0.38 > 0.25$, meaning that turbulence was damped by density stratification [*Miles*, 1961; *Geyer and Smith*, 1987; *Trowbridge and Kineke*, 1994]. It

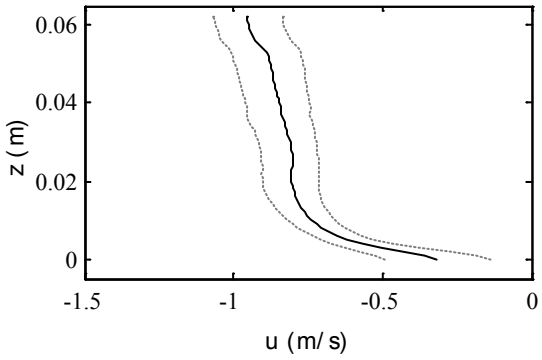

Figure 5.11: Phase-space averaged velocity profile for bin $-1.25\ \mathrm{m/s} \leq u_\infty \leq -0.75\ \mathrm{m/s}$, $-0.50\ \mathrm{m/s^2} \leq \frac{du_\infty}{dt} \leq 0\ \mathrm{m/s^2}$. Gray dotted lines indicate 25% and 75% percentiles of averaged velocity profiles.

is noted that stratification may reduce the value of κ in equation (5.10) [*Winterwerp*, 2001] but this does not lead to order-of-magnitude changes in the scaling analysis.

Suspended sediment concentrations have been observed to be even larger during the uprush than during the backwash [*Masselink et al.*, 2005] so density stratification effects are expected to occur during both the uprush and backwash phases of the swash cycle. Understanding the exact spatial and temporal importance of density stratification requires a detailed, simultaneous analysis of the suspended sediment concentrations and the turbulent kinetic energy budget that is beyond the scope of this chapter. However, this order-of-magnitude scaling analysis demonstrates that density stratification plays a significant role in the near-bed TKE budget in the swash zone. Laboratory and numerical studies of swash zone turbulence that do not include suspended sediment may therefore overestimate near-bed turbulence levels compared to natural conditions.

5.5 Conclusions

The turbulence dissipation rate ϵ in the swash zone and the inner surf zone of a dissipative beach was investigated using a structure function method. A laboratory test under stationary unidirectional flow displayed excellent agreement between turbulence dissipation estimates based on the structure function, the wavenumber spectrum and the frequency spectrum. The main advantages of the structure function method are that it does not invoke Taylor's hypothesis and that it provides the opportunity to investigate the spatial and temporal evolution of the dissipation rate. Swash zone dissipation rates were estimated between $6 \cdot 10^{-5}$ $\mathrm{m}^2/\mathrm{s}^3$ and $8 \cdot 10^{-3}$ $\mathrm{m}^2/\mathrm{s}^3$, with a mean of $1.2 \cdot 10^{-3}$ $\mathrm{m}^2/\mathrm{s}^3$ to $1.3 \cdot 10^{-3}$ $\mathrm{m}^2/\mathrm{s}^3$ depending on local water depth. Dissipation rates increased slightly with decreasing water depth in the swash zone and showed no significant correlation with offshore wave height, consistent with a saturated surf zone. The temporal variability of the turbulence dissipation was mainly driven by bores and a good agreement was observed between dissipation rates and remotely-sensed pixel intensities, which were used as a proxy for wave breaking. However, bores may carry significant turbulence dissipation even after the breaking wave surface signature has disappeared. Dissipation rates decayed rapidly after bore arrival following a decay rate similar to grid turbulence, in the form of a power law with exponent -1.94.

Vertical dissipation profiles showed that turbulence dissipation was dominated by bore-generated turbulence during the uprush and bed-generated turbulence during the later stages of the backwash, with the transition from bore-dominated to bed-dominated occurring during early stages of the backwash when the cross-shore velocity was approximately -0.5 m/s. Backwash turbulence dissipation rates, however, were two orders of magnitude smaller than values obtained from a log-layer

prediction. A scaling analysis revealed that due to the large suspended sediment concentrations in the swash zone, sediment-induced density stratification was an order of magnitude larger than measured turbulence dissipation. This finding has important implications for numerical and laboratory studies of swash zone turbulence, which may overestimate near-bed turbulence levels if the effect of sediment-induced density stratification on the turbulent kinetic energy budget is not accounted for.

Chapter 6

RECOMMENDATIONS FOR FURTHER RESEARCH

6.1 The Conductivity Concentration Profiler

The development of the Conductivity Concentration Profiler (Chapter 2), the first instrument capable of measuring sediment concentration profiles in the sheet flow layer under field conditions, opens a host of new research possibilities. First, more datasets are to be collected of sheet flow in different environments and conditions, including recent efforts in the Netherlands and Mexico. A few months after the first CCP measurements were taken during the BeST field experiment (Chapter 3 and 4), CCPs were again deployed during the Bardex II (Barrier Dynamics Experiment) study. The aim of this experiment was to "collect a near proto-type data set of energetic waves acting on a sandy beach/barrier system to improve our quantitative understanding and modelling capability of shallow water sediment transport processes in the inner surf, swash and overwash zone." [*Masselink et al.*, in preparation]. To this end, a sand barrier island was constructed in the large-scale Delta Flume facility in the Netherlands and exposed to a range of wave and water level conditions. CCPs were deployed in the swash zone that had a steep (roughly 1:10) slope and experienced wind-wave period (T = 8 - 12 s) dominated swash events, in contrast with the infragravity-timescale swash events on a low-sloping (roughly 1:45) beach during the BeST field study. Bardex II thus provided a second CCP dataset that was highly complementary to the BeST dataset. CCPs have also been deployed on a sea-breeze

dominated beach in Yucatan, Mexico in March - April 2014. A deployment in the surf zone as part of a large-scale laboratory study has been planned as well.

The CCP may also be useful for investigating other processes besides sheet flow. The sediment concentration profiles can be used to generate continuous time series of bed level elevation regardless of whether the sensor is submerged or emerged, in contrast with other techniques such as acoustic or lidar measurements which only give a bed level elevation estimate when the bed is emerged in between swash events. Analysis of these bed level elevation timeseries [*Puleo et al.*, 2014a] revealed interesting fluctuations at time scales from seconds to hours. Deploying two or three CCPs at small [O(1 m)] cross-shore separation distances would make it possible to study fluctuations of the local bed level slope. The CCP could also be modified to serve as a compact, field-capable conductivity profiler to measure other parameters such as the soil moisture content (saturation level) of the beach sand volume or to detect fresh or salt water lenses. A preliminary test has shown that the CCP may also be capable of measuring time-varying compaction of cohesive sediment beds. Since the conductivity probe is detachable from the main measurement board, a new conductivity probe with a different geometry could be tailor-made for each of these applications and remain compatible with the existing measurement board.

6.2 Sheet Flow and Swash-zone Morphology

Analysis of sediment concentration measurements in this work focused on sheet flow during quasi-steady backwash, which is the simplest case of sheet flow observed in the swash zone (Chapter 4). The more general case of sheet flow under arbitrary forcing conditions (in other words, sheet flow as it occurs throughout the entire swash cycle) is much more complicated due to additional sediment mobilization

mechanisms such as pressure gradients and bore turbulence and due to unsteady forcing. Near-bed sediment mobilization by pressure gradients is known as plug flow [*Sleath*, 1999; *Foster et al.*, 2006a] and sediment transport during the uprush in the swash zone may be a combination of sheet flow and plug flow. The Bardex II CCP dataset, which had shorter incident wave periods, no infragravity-dominated wave motion, and a higher CCP sampling frequency (8 Hz, compared to 4 Hz during BeST), provided an excellent starting point for the analysis of time-varying sheet flow.

The CCP has provided measurements of the sheet flow sediment concentration profile under field conditions with unprecedented detail. In order to calculate sediment fluxes, however, a velocity profile in the sheet flow layer is also necessary. The velocity profile in the sheet flow layer has been measured in laboratory experiments, e.g., using image analysis through the side-wall of a flow tunnel [*Ahmed and Sato*, 2001; *Capart et al.*, 2002], using an in-situ boroscope [*Cowen et al.*, 2010] or by computing the cross-correlation of sediment concentration time series measured at different locations along the flow [*McLean et al.*, 2001]. Acoustic Doppler velocimetry techniques have been optimized to penetrate into the sheet layer, but it is uncertain if measurements can be made at high concentrations in the lower sections of the sheet layer for natural sand particles [*Hurther et al.*, 2011; *Chassagneux and Hurther*, 2014]. None of these techniques are readily deployable in the field, either because the measurement instruments cannot be deployed without generating significant flow disturbance and scour, or because repeatable, controllable conditions are required to obtain reliable velocity estimates. *Puleo et al.* [submitted, 2014b] therefore calculated sediment fluxes from CCP concentration measurements and an

estimated velocity profile by extrapolating velocities measured above the sheet flow layer to the non-moving sediment bed using an assumed velocity profile function.

Developing field-capable measurement techniques for velocity in the sheet flow layer is therefore a crucial next step to improve estimates of the sediment transport budget in the swash zone. Of the aforementioned laboratory techniques, imaging techniques may be the most promising candidate to be adapted to field scale. A sideways-looking high-speed (90 frames per second) video camera was deployed in the swash zone during the Bardex II study as a pilot test. A plexiglass side-wall was placed parallel to the cross-shore flow so that the flow disturbance created by the camera housing did not influence the flow field in the camera field of view. The high-speed imagery will be analyzed using Particle Image Velocimetry (PIV) or other techniques to provide velocity estimates within the sheet flow layer. Cross-correlation of two sediment concentration signals measured at different cross-shore locations [*McLean et al.*, 2001; *Dohmen-Janssen and Hanes*, 2002; *Hassan and Ribberink*, 2005] may also appear promising for field-scale application. However, the technique has so far only proven successful when ensemble-averaging across several repeatable waves was used to suppress noise and find the cross-correlation peak. Ensemble averaging is difficult under irregular wave forcing and it is therefore uncertain whether a cross-correlation technique can be successful in field settings. In addition, concentration measurements must be collected at high sampling rates (1000 Hz) to perform cross-correlation. These sampling rates are achievable using a single-point concentration sensor such as the CCM. The CCP, which measures a 29-point concentration profile by cycling through an array of electrodes, presently has a

maximum sampling rate of 8 Hz and would have to be modified significantly to achieve high enough sampling rates to perform cross-correlation.

Measurements of sheet flow using the CCP and a yet-to-be-developed velocity measurement solution, as well as measurements of turbulence dissipation (Chapter 5), certainly lead to an improved understanding of the swash-zone sediment budget at the small scale (timescales on the order of seconds and minutes). However, it is important to bear in mind that even with improved predictions of small-scale sediment transport, accurate predictions of sediment transport at the meso-scale (time scales of hours, days or weeks), which are ultimately important for practical applications, are still far from achieved. An alternative approach for developing improved models of swash zone morphodynamics at the meso-scale may be to focus on meso-scale behavior directly rather than as the aggregate of small scale processes. For example, *Masselink et al.* [2009] suggested developing a sediment transport model based on the equilibrium gradient in the swash zone. Measurements of local beach slope fluctuations using the CCP (Section 6.1) would provide useful data to develop such a model.

6.3 Turbulence Dissipation Rates

Chapter 5 described how swash zone turbulence dissipation rates were estimated from high-resolution (1 mm), small-range (3 cm) velocity profile measurements using the structure function. Before this work, the structure function had only been applied to large-range [*O(10 m)*] velocity profiles measured by Acoustic Doppler Current Profilers (ADCPs) [*Wiles et al.*, 2006; *Mohrholz et al.*, 2008; *Whipple and Luettich*, 2009]. The advent of a next-generation profiling acoustic velocimeter, the Nortek Vectrino II [*Craig et al.*, 2011], made it possible for the first time to calculate the structure function at a smaller scale, e.g. in the shallow flows of

the swash zone. As these next-generation profiling velocimeters become more widespread, the structure function method will remain a valuable tool to estimate turbulence dissipation rates in different environments. For example, *Brinkkemper et al.* [in preparation] analyzed turbulence throughout the surf and swash zones during the Bardex II experiment and used the structure function for swash-zone dissipation rate estimates. Similarly, *Pieterse et al.* [2013] estimated turbulence dissipation rates in shallow flows over a tidal saltmarsh.

6.4 Negative Results

Recommendations for further research also come in the form of negative or unsuccessful research results, serving as both a warning to those who consider going down the same path and as an outtakes reel at the end of the story. During the development of the CCP, for example, some effort was initially made to extend the two-electrode conductivity measurement technique of *Puleo et al.* [2010] to operate in both fresh and salt water. This effort proved unsuccessful, and the approach was changed to the four-electrode conductivity measurement technique that is used in the current version of the CCP and the CCM.

A technique was also developed to estimate cross-shore velocities throughout the entire swash event and address the problem of backwash flows that are too shallow for in-situ current meters. The swash-zone free surface was detected from video images recorded by a camera looking through the side wall of a small wave flume, and a time series of depth-averaged velocities was calculated using the volume continuity technique validated by *Blenkinsopp et al.* [2010b]. While providing accurate results [*Lanckriet and Puleo*, 2010], the technique was cumbersome and could only be used in flumes with glass sidewalls. Acoustic distance meters and lidar are more

advantageous options than video imagery for obtaining measurements of the free surface since they are easier to set up and can be deployed in a wider range of environments, including large-scale laboratory and field experiments. These two techniques have therefore become increasingly popular [*Blenkinsopp et al.*, 2010a; *Puleo et al.*, 2014b].

Chapter 7

CONCLUSIONS

This work described field measurements and innovative measurement techniques to improve understanding of near-bed hydrodynamics and sediment transport in the swash zone. A first main accomplishment was the development of the Conductivity Concentration Profiler, a new sensor that measures sediment concentrations in the sheet flow layer. The CCP cycles through an array of electrodes to obtain a vertical profile of electrical conductivity with a 29 mm range and a 1 mm resolution. Laboratory measurements of natural sand suspended neutrally in a Lithium Metatungstate (LMT) solution demonstrated that electrical conductivity of the sediment-water mixture is a good measurement proxy for sediment concentration. The relationship between conductivity and concentration was described accurately by Archie's law. A finite differences model of the current field around the CCP conductivity probe was set up to analyze the CCP measurement volume and its smoothing effect on sharp gradients in the concentration profile. Model results showed that the measurement volume is large enough to contain at least several thousand sand grains leading to a robust estimate of the sediment volume fraction, and that sheet flow layers with a thickness of over 5 mm are accurately resolved by the CCP. The numerical model was also used to develop a correction formula to correct for any residual smoothing effect at larger sheet thicknesses.

A comprehensive field dataset of swash zone processes, including CCP measurements in the sheet flow layer, was obtained during the BeST (Beach Sand Transport) experiment conducted in Perranporth, UK, in October 2011.

Analysis of sheet flow measurements in this work focused on quasi-steady backwash, which generated sheet flow that was unaffected by surface-generated turbulence, phase lags and pressure gradients and thus was highly similar to stationary, unidirectional sheet flow. Sheet flow sediment concentration profiles displayed a self-similar shape for sheet flow layer thicknesses ranging from 6 to 18 mm, with a linear shape in the lower section of the profile and a power-law shape in the upper section. A single curve proposed by *O'Donoghue and Wright* [2004a] described the profile shape for all observed sheet flow layer thicknesses. Sheet flow layer thicknesses and sheet load showed good correlation ($r^2 = 0.60$ and 0.53, respectively) with the mobility number, a measure of hydrodynamic forcing that is proportional to the flow velocity squared. A previous analytical model to predict sheet flow layer thickness by *Wilson* [1987] assumed a linear shape of the concentration profile. Incorporating the curve by *O'Donoghue and Wright* [2004a] into this model provided sheet flow layer thickness predictions that are in better agreement with previous experiments.

High-resolution near-bed velocity profiles were also measured during the BeST field study using a new profiling acoustic Doppler velocimeter, and were used to estimate the turbulence dissipation rate based on the structure function. The structure function method was first validated in a laboratory test under stationary flow and showed excellent agreement with turbulence dissipation rate estimates derived from both the wavenumber spectrum and the frequency spectrum. Dissipation rates observed in the swash zone ranged between $6 \cdot 10^{-5}$ m^2/s^3 and $8 \cdot 10^{-3}$ m^2/s^3, with a

mean of $1.2 \cdot 10^{-3}$ m^2/s^3 to $1.3 \cdot 10^{-3}$ m^2/s^3 depending on local water depth. Dissipation rates tended to be highest immediately following bore arrival, then decreased rapidly during the remainder of the uprush, and then increased again during the backwash. The rapid decay of the dissipation rate following bore arrival was similar to grid turbulence decay, and can be described by a power law with exponent -1.94 (compared to -2.3 for grid turbulence). Large dissipation rates following bore arrival also corresponded with high pixel intensities in remotely sensed video imagery of the measurement site, indicative of wave breaking. The dominant turbulence generation mechanism was investigated based on vertical profiles of the dissipation rate. Bore-generated turbulence was the dominant source during the uprush and bed shear was dominant during the backwash. A scaling analysis showed that sediment-induced density stratification was an order of magnitude larger than turbulence dissipation rates measured during the backwash, indicating that even on sandy beaches, stratification effects are an important component in the near-bed turbulent kinetic energy budget.

Going forward, both the CCP and the structure function method will be important tools to quantify sheet flow sediment transport and turbulence dissipation rates, respectively, and will be used in future field and laboratory studies. Determining velocities in the sheet flow layer remains an important next step to accurately determine the sediment budget in the swash zone.

REFERENCES

Aagaard, T., and M. G. Hughes (2006), Sediment suspension and turbulence in the swash zone of dissipative beaches, *Marine Geology*, *228*(1–4), 117–135, doi:10.1016/j.margeo.2006.01.003.

Aarninkhof, S. G. J., and B. G. Ruessink (2004), Video observations and model predictions of depth-induced wave dissipation, *IEEE Transactions on Geoscience and Remote Sensing*, *42*(11), 2612–2622, doi:10.1109/TGRS.2004.835349.

Adler, P. M., C. G. Jacquin, and J.-F. Thovert (1992), The formation factor of reconstructed porous media, *Water Resources Research*, *28*(6), 1571–1576, doi:10.1029/92WR00059.

Ahmed, A. S. M., and S. Sato (2001), Investigation of bottom boundary layer dynamics of movable bed by using enhanced PIV technique, *Coastal Engineering Journal*, *43*(04), 239–258, doi:10.1142/S0578563401000360.

Ahmed, A. S. M., and S. Sato (2003), A Sheetflow Transport Model for Asymmetric Oscillatory Flows: Part II: Mixed Grain Size Sediments, *Coastal Engineering Journal*, *45*(03), 339–361, doi:10.1142/S0578563403000798.

Alsina, J. M., and I. Cáceres (2011), Sediment suspension events in the inner surf and swash zone. Measurements in large-scale and high-energy wave conditions, *Coastal Engineering*, *58*(8), 657–670, doi:10.1016/j.coastaleng.2011.03.002.

Alsina, J. M., I. Cáceres, J. Sospedrat, and T. E. Baldock (2009), Lagrangian modelling of suspended sediment in the swash zone, *Journal of Coastal Research*, *56*, 1716–1720.

Alsina, J. M., I. Cáceres, M. Brocchini, and T. E. Baldock (2012), An experimental study on sediment transport and bed evolution under different swash zone morphological conditions, *Coastal Engineering*, *68*, 31–43, doi:10.1016/j.coastaleng.2012.04.008.

Amoudry, L., T.-J. Hsu, and P. L.-F. Liu (2008), Two-phase model for sand transport in sheet flow regime, *Journal of Geophysical Research: Oceans*, *113*(C3), C03011, doi:10.1029/2007JC004179.

Archie, G. (1942), The electrical resistivity log as an aid in determining some reservoir characteristics, *Transactions of the American Institute of Mining, Metallurgical and Petroleum Engineers*, *146*, 54–62.

Armanini, A., H. Capart, L. Fraccarollo, and M. Larcher (2005), Rheological stratification in experimental free-surface flows of granular–liquid mixtures, *Journal of Fluid Mechanics*, *532*, 269–319, doi:10.1017/S0022112005004283.

Asano, T. (1995), Sediment transport under sheet-flow conditions, *Journal of waterway, port, coastal, and ocean engineering*, *121*, 239–246, doi:10.1061/(ASCE)0733-950X(1995)121:5(239).

Astruc, D., S. Cazin, E. Cid, O. Eiff, L. Lacaze, P. Robin, F. Toublanc, and I. Cáceres (2012), A stereoscopic method for rapid monitoring of the spatio-temporal evolution of the sand-bed elevation in the swash zone, *Coastal Engineering*, *60*, 11–20, doi:10.1016/j.coastaleng.2011.08.007.

Austin, M. J., G. Masselink, P. E. Russell, I. L. Turner, and C. E. Blenkinsopp (2011), Alongshore fluid motions in the swash zone of a sandy and gravel beach, *Coastal Engineering*, *58*(8), 690–705, doi:10.1016/j.coastaleng.2011.03.004.

Bagnold, R. A. (1954), Experiments on a Gravity-Free Dispersion of Large Solid Spheres in a Newtonian Fluid under Shear, *Proceedings of the Royal Society of London. Series A. Mathematical and Physical Sciences*, *225*(1160), 49–63, doi:10.1098/rspa.1954.0186.

Bagnold, R. A. (1956), The Flow of Cohesionless Grains in Fluids, *Philosophical Transactions of the Royal Society of London. Series A, Mathematical and Physical Sciences*, *249*(964), 235–297.

Bagnold, R. A. (1966a), *An approach to the sediment transport problem from general physics*, Professional Paper, U.S.G.S., Washington, D.C. [online] Available from: 10.1017/S0016756800049074

Bagnold, R. A. (1966b), The shearing and dilatation of dry sand and the "singing" mechanism, *Proceedings of the Royal Society of London. Series A. Mathematical and Physical Sciences*, *295*(1442), 219–232, doi:10.1098/rspa.1966.0236.

Bagnold, R. A., and G. Taylor (1946), Motion of Waves in Shallow Water. Interaction between Waves and Sand Bottoms, *Proceedings of the Royal Society of London. Series A, Mathematical and Physical Sciences*, *187*(1008), 1–18, doi:10.1098/rspa.1946.0062.

Bailard, J. A. (1981), An energetics total load sediment transport model for a plane sloping beach, *Journal of Geophysical Research: Oceans*, *86*(C11), 10938–10954, doi:10.1029/JC086iC11p10938.

Baker, J., and A. Kudrolli (2010), Maximum and minimum stable random packings of Platonic solids, *Physical Review E*, *82*(6), 061304, doi:10.1103/PhysRevE.82.061304.

Bakhtyar, R., D. A. Barry, L. Li, D. S. Jeng, and A. Yeganeh-Bakhtiary (2009a), Modeling sediment transport in the swash zone: A review, *Ocean Engineering*, *36*(9–10), 767–783, doi:10.1016/j.oceaneng.2009.03.003.

Bakhtyar, R., A. Ghaheri, A. Yeganeh-Bakhtiary, and D. A. Barry (2009b), Process-based model for nearshore hydrodynamics, sediment transport and morphological evolution in the surf and swash zones, *Applied Ocean Research*, *31*(1), 44–56, doi:10.1016/j.apor.2009.05.002.

Bakhtyar, R., A. Yeganeh-Bakhtiary, D. A. Barry, and A. Ghaheri (2009c), Two-phase hydrodynamic and sediment transport modeling of wave-generated sheet flow, *Advances in Water Resources*, *32*(8), 1267–1283, doi:10.1016/j.advwatres.2009.05.002.

Bakhtyar, R., D. A. Barry, A. Yeganeh-Bakhtiary, L. Li, J.-Y. Parlange, and G. C. Sander (2010), Numerical simulation of two-phase flow for sediment transport in the inner-surf and swash zones, *Advances in Water Resources*, *33*(3), 277–290, doi:10.1016/j.advwatres.2009.12.004.

Bakker, W. T., W. G. M. Van Kesteren, and Z. H. Yu (1988), Grain-Grain Interaction in Oscillating Sheetflow, in *Proc. 21st Int. Conf. Coastal Eng*, pp. 718–731, ASCE, Torremolinos, Spain.

Baldock, T. E., and M. G. Hughes (2006), Field observations of instantaneous water slopes and horizontal pressure gradients in the swash-zone, *Continental Shelf Research*, *26*(5), 574–588, doi:10.1016/j.csr.2006.02.003.

Baldock, T. E., F. Weir, and M. G. Hughes (2008), Morphodynamic evolution of a coastal lagoon entrance during swash overwash, *Geomorphology*, *95*(3–4), 398–411, doi:10.1016/j.geomorph.2007.07.001.

Barnes, M. P., and T. E. Baldock (2010), A Lagrangian model for boundary layer growth and bed shear stress in the swash zone, *Coastal Engineering*, *57*(4), 385–396, doi:10.1016/j.coastaleng.2009.11.009.

Barnes, M. P., T. O'Donoghue, J. M. Alsina, and T. E. Baldock (2009), Direct bed shear stress measurements in bore-driven swash, *Coastal Engineering*, *56*(8), 853–867, doi:10.1016/j.coastaleng.2009.04.004.

Bauer, B. O., and R. G. D. Davidson-Arnott (2003), A general framework for modeling sediment supply to coastal dunes including wind angle, beach geometry, and fetch effects, *Geomorphology*, *49*(1–2), 89–108, doi:10.1016/S0169-555X(02)00165-4.

Beach, R., and R. Sternberg (1991), Infragravity driven suspended sediment transport in the swash, inner and outer surf zone., in *Proc. Coastal Sediments 1991*, vol. 1, pp. 114–128, ASCE, Seattle, WA.

Beach, R. A., and R. W. Sternberg (1988), Suspended sediment transport in the surf zone: Response to cross-shore infragravity motion, *Marine Geology*, *80*(1–2), 61–79, doi:10.1016/0025-3227(88)90072-2.

Blenkinsopp, C. E., M. A. Mole, I. L. Turner, and W. L. Peirson (2010a), Measurements of the time-varying free-surface profile across the swash zone obtained using an industrial LIDAR, *Coastal Engineering*, *57*(11–12), 1059–1065, doi:10.1016/j.coastaleng.2010.07.001.

Blenkinsopp, C. E., I. L. Turner, G. Masselink, and P. E. Russell (2010b), Validation of volume continuity method for estimation of cross-shore swash flow velocity, *Coastal Engineering*, *57*(10), 953–958, doi:10.1016/j.coastaleng.2010.05.005.

Blenkinsopp, C. E., I. L. Turner, G. Masselink, and P. E. Russell (2011), Swash zone sediment fluxes: Field observations, *Coastal Engineering*, *58*(1), 28–44, doi:10.1016/j.coastaleng.2010.08.002.

Bodge, K. R. (1989), A Literature Review of the Distribution of Longshore Sediment Transport across the Surf Zone, *Journal of Coastal Research*, *5*(2), 307–328.

Bowen, A. J. (1980), Simple models of nearshore sedimentation; beach profiles and longshore bars, in *The Coastline of Canada*, edited by S. B. McCann, pp. 1–11, Geological Survey of Canada.

Briganti, R., N. Dodd, D. Pokrajac, and T. O'Donoghue (2011), Non linear shallow water modelling of bore-driven swash: Description of the bottom boundary layer, *Coastal Engineering*, *58*(6), 463–477, doi:10.1016/j.coastaleng.2011.01.004.

Brinkkemper, J. A., F. Grasso, B. G. Ruessink, T. Lanckriet, and J. A. Puleo (in preparation), Observations of turbulence within the surf and swash zone of a field-scale laboratory beach, *Coastal Engineering*.

Bruggeman, D. A. G. (1935), Berechnung verschiedener physikalischer Konstanten von heterogenen Substanzen. I. Dielektrizitätskonstanten und Leitfähigkeiten der Mischkörper aus isotropen Substanzen, *Annalen der Physik*, *416*(8), 636–664, doi:10.1002/andp.19354160802.

Bryan, K. R., K. P. Black, and R. M. Gorman (2003), Spectral Estimates of Dissipation Rate within and near the Surf Zone, *Journal of Physical Oceanography*, *33*(5), 979–993, doi:10.1175/1520-0485(2003)033<0979:SEODRW>2.0.CO;2.

Butt, T., and P. Russell (1999), Suspended sediment transport mechanisms in high-energy swash, *Marine Geology*, *161*(2-4), 361–375, doi:10.1016/S0025-3227(99)00043-2.

Butt, T., P. Russell, and I. Turner (2001), The influence of swash infiltration–exfiltration on beach face sediment transport: onshore or offshore?, *Coastal Engineering*, *42*(1), 35–52, doi:10.1016/S0378-3839(00)00046-6.

Butt, T., P. Russell, J. Puleo, J. Miles, and G. Masselink (2004), The influence of bore turbulence on sediment transport in the swash and inner surf zones, *Continental Shelf Research*, *24*(7–8), 757–771, doi:10.1016/j.csr.2004.02.002.

Butt, T., P. Russell, J. Puleo, and G. Masselink (2005), The Application of Bagnold-Type Sediment Transport Models in the Swash Zone, *Journal of Coastal Research*, *21*(5), 887–895, doi:10.2112/04-0210.1.

Cáceres, I., and J. M. Alsina (2012), A detailed, event-by-event analysis of suspended sediment concentration in the swash zone, *Continental Shelf Research*, *41*, 61–76, doi:10.1016/j.csr.2012.04.004.

Calantoni, J., and J. A. Puleo (2006), Role of pressure gradients in sheet flow of coarse sediments under sawtooth waves, *Journal of Geophysical Research: Oceans*, *111*(C1), C01010, doi:10.1029/2005JC002875.

Calantoni, J., J. A. Puleo, and K. Todd Holland (2006), Simulation of sediment motions using a discrete particle model in the inner surf and swash-zones, *Continental Shelf Research*, *26*(5), 610–621, doi:10.1016/j.csr.2005.11.013.

Capart, H., and L. Fraccarollo (2011), Transport layer structure in intense bed-load, *Geophysical Research Letters*, *38*(20), L20402, doi:10.1029/2011GL049408.

Capart, H., D. L. Young, and Y. Zech (2002), Voronoï imaging methods for the measurement of granular flows, *Experiments in Fluids*, *32*(1), 121–135, doi:10.1007/s003480200013.

Chassagneux, F. X., and D. Hurther (2014), Wave bottom boundary layer processes below irregular surfzone breaking waves with light-weight sheet flow particle transport, *Journal of Geophysical Research: Oceans*, *119*(3), 1668–1690, doi:10.1002/2013JC009338.

Chen, X., Y. Li, X. Niu, D. Chen, and X. Yu (2011), A two-phase approach to wave-induced sediment transport under sheet flow conditions, *Coastal Engineering*, *58*(11), 1072 – 1088, doi:10.1016/j.coastaleng.2011.06.003.

Conley, D. C., and J. G. Griffin Jr (2004), Direct measurements of bed stress under swash in the field, *Journal of Geophysical Research*, *109*(C3), C03050, doi:10.1029/2003JC001899.

Cowen, E., R. Dudley, Q. Liao, E. Variano, and P. Liu (2010), An insitu borescopic quantitative imaging profiler for the measurement of high concentration sediment velocity, *Experiments in Fluids*, *49*(1), 77–88, doi:10.1007/s00348-009-0801-8.

Cowen, E. A., I. M. Sou, P. L.-F. Liu, and B. Raubenheimer (2003), Particle Image Velocimetry Measurements within a Laboratory-Generated Swash Zone, *Journal of Engineering Mechanics*, *129*(10), 1119–1129, doi:10.1061/(ASCE)0733-9399(2003)129:10(1119).

Craig, R. G. A., C. Loadman, B. Clement, P. J. Rusello, and E. Siegel (2011), Characterization and testing of a new bistatic profiling acoustic Doppler velocimeter: The Vectrino-II, *Current, Waves and Turbulence Measurements*, 246 –252, doi:10.1109/CWTM.2011.5759559.

De La Rue, R. E., and C. W. Tobias (1959), On the Conductivity of Dispersions, *Journal of The Electrochemical Society*, *106*(9), 827–833, doi:10.1149/1.2427505.

Desombre, J., D. Morichon, and M. Mory (2013), RANS v2–f simulation of a swash event: Detailed flow structure, *Coastal Engineering*, *71*, 1–12, doi:10.1016/j.coastaleng.2012.07.001.

Dibajnia, M., and A. Watanabe (1998), Transport rate under irregular sheet flow conditions, *Coastal Engineering*, *35*(3), 167–183, doi:10.1016/S0378-3839(98)00034-9.

Dick, J. E. (1989), Sediment transport in oscillatory flow, Ph.D. dissertation, University of Cambridge, Cambridge, UK.

Dick, J. E., and J. F. A. Sleath (1991), Velocities and concentrations in oscillatory flow over beds of sediment, *Journal of Fluid Mechanics*, *233*, 165–196, doi:10.1017/S0022112091000447.

Dick, J. E., and J. F. A. Sleath (1992), Sediment transport in oscillatory sheet flow, *Journal of Geophysical Research: Oceans*, *97*(C4), 5745–5758, doi:10.1029/92JC00054.

Dinehart, R. L. (1992), Evolution of coarse gravel bed forms: Field measurements at flood stage, *Water Resources Research*, *28*(10), 2667–2689, doi:199210.1029/92WR01357.

Dingler, J. R., and D. L. Inman (1976), Wave-Formed Ripples in Nearshore Sands, in *Proc. 15th Int. Conf. Coastal Eng*, vol. 2, pp. 2109–2126, ASCE, Honolulu, HI. [online] Available from: http://journals.tdl.org/ICCE/article/view/3172

Dohmen-Janssen, C. M., and D. M. Hanes (2002), Sheet flow dynamics under monochromatic nonbreaking waves, *Journal of Geophysical Research*, *107*(C10), 21, doi:10.1029/2001JC001045.

Dohmen-Janssen, C. M., and D. M. Hanes (2005), Sheet flow and suspended sediment due to wave groups in a large wave flume, *Continental Shelf Research*, *25*(3), 333–347, doi:10.1016/j.csr.2004.10.009.

Dohmen-Janssen, C. M., W. N. Hassan, and J. S. Ribberink (2001), Mobile-bed effects in oscillatory sheet flow, *Journal of Geophysical Research: Oceans*, *106*(C11), 27103–27115, doi:10.1029/2000JC000513.

Dong, L. P., S. Sato, and H. Liu (2013), A sheetflow sediment transport model for skewed-asymmetric waves combined with strong opposite currents, *Coastal Engineering*, *71*, 87–101, doi:10.1016/j.coastaleng.2012.08.004.

Downing, J. (2006), Twenty-five years with OBS sensors: The good, the bad, and the ugly, *Continental Shelf Research*, *26*(17–18), 2299–2318, doi:10.1016/j.csr.2006.07.018.

Drake, T. G., and J. Calantoni (2001), Discrete particle model for sheet flow sediment transport in the nearshore, *Journal of Geophysical Research: Oceans*, *106*(C9), 19859–19868, doi:10.1029/2000JC000611.

Elfrink, B., and T. Baldock (2002), Hydrodynamics and sediment transport in the swash zone: a review and perspectives, *Coastal Engineering*, *45*(3–4), 149–167, doi:10.1016/S0378-3839(02)00032-7.

Elgar, S., B. Raubenheimer, and R. T. Guza (2005), Quality control of acoustic Doppler velocimeter data in the surfzone, *Measurement Science and Technology*, *16*(10), 1889–1893, doi:10.1088/0957-0233/16/10/002.

Feddersen, F. (2010), Quality controlling surf zone acoustic Doppler velocimeter observations to estimate the turbulent dissipation rate, *Journal of Atmospheric and Oceanic Technology*, *27*(12), 2039–2055, doi:10.1175/2010JTECHO783.1.

Feddersen, F. (2012a), Observations of the Surf-Zone Turbulent Dissipation Rate, *Journal of Physical Oceanography*, *42*(3), 386–399, doi:10.1175/JPO-D-11-082.1.

Feddersen, F. (2012b), Scaling surf zone turbulence, *Geophysical Research Letters*, *39*(18), L18613, doi:10.1029/2012GL052970.

Feddersen, F., J. H. Trowbridge, and A. J. Williams (2007), Vertical Structure of Dissipation in the Nearshore, *Journal of Physical Oceanography*, *37*(7), 1764–1777, doi:10.1175/JPO3098.1.

Flick, R. E., and R. A. George (1990), Turbulence scales in the surf and swash, in *Proc. 22nd Int. Conf. Coastal Eng.*, vol. 1, pp. 557–569, ASCE, Delft, The Netherlands.

Foster, D. L., A. J. Bowen, R. A. Holman, and P. Natoo (2006a), Field evidence of pressure gradient induced incipient motion, *Journal of Geophysical Research*, *111*(C05), C05004, doi:10.1029/2004JC002863.

Foster, D. L., R. A. Beach, and R. A. Holman (2006b), Turbulence observations of the nearshore wave bottom boundary layer, *Journal of Geophysical Research*, *111*(C4), C04011, doi:10.1029/2004JC002838.

George, R., R. E. Flick, and R. T. Guza (1994), Observations of turbulence in the surf zone, *Journal of Geophysical Research: Oceans*, *99*(C1), 801–810, doi:10.1029/93JC02717.

Gerbi, G. P., J. H. Trowbridge, E. A. Terray, A. J. Plueddemann, and T. Kukulka (2009), Observations of Turbulence in the Ocean Surface Boundary Layer: Energetics and Transport, *Journal of Physical Oceanography*, *39*(5), 1077–1096, doi:10.1175/2008JPO4044.1.

Geyer, W. R., and J. D. Smith (1987), Shear Instability in a Highly Stratified Estuary, *Journal of Physical Oceanography*, *17*(10), 1668–1679, doi:10.1175/1520-0485(1987)017<1668:SIIAHS>2.0.CO;2.

Goring, D., and V. Nikora (2002), Despiking Acoustic Doppler Velocimeter Data, *Journal of Hydraulic Engineering*, *128*(1), 117–126, doi:10.1061/(ASCE)0733-9429(2002)128:1(117).

Grasso, F., B. Castelle, and B. G. Ruessink (2012), Turbulence dissipation under breaking waves and bores in a natural surf zone, *Continental Shelf Research*, *43*(0), 133–141, doi:10.1016/j.csr.2012.05.014.

Guard, P. A., and T. E. Baldock (2007), The influence of seaward boundary conditions on swash zone hydrodynamics, *Coastal Engineering*, *54*(4), 321–331, doi:10.1016/j.coastaleng.2006.10.004.

Haller, M. C., and P. A. Catalán (2009), Remote sensing of wave roller lengths in the laboratory, *Journal of Geophysical Research: Oceans*, *114*(C7), C07022, doi:10.1029/2008JC005185.

Hanes, D. M., and A. J. Bowen (1985), A granular-fluid model for steady intense bed-load transport, *Journal of Geophysical Research*, *90*(C5), 9149–9158, doi:10.1029/JC090iC05p09149.

Hanes, D. M., and D. L. Inman (1985), Observations of rapidly flowing granular-fluid materials, *Journal of Fluid Mechanics*, *150*, 357–380, doi:10.1017/S0022112085000167.

Hassan, W. N., and J. S. Ribberink (2005), Transport processes of uniform and mixed sands in oscillatory sheet flow, *Coastal Engineering*, *52*(9), 745–770, doi:10.1016/j.coastaleng.2005.06.002.

Holland, T. K., R. A. Holman, T. C. Lippmann, J. Stanley, and N. Plant (1997), Practical use of video imagery in nearshore oceanographic field studies, *IEEE Journal of Oceanic Engineering*, *22*(1), 81–92, doi:10.1109/48.557542.

Horikawa, K., A. Watanabe, and S. Katori (1982), Sediment transport under sheet flow conditions, in *Proc. 18th Int. Conf. Coastal Eng*, pp. 1335–1352, Cape Town, South Africa. [online] Available from: https://journals.tdl.org/ICCE/issue/view/140/showToc

Horn, D. P., and T. Mason (1994), Swash zone sediment transport modes, *Marine Geology*, *120*(3–4), 309–325, doi:10.1016/0025-3227(94)90064-7.

Hsu, T.-J., and P. L.-F. Liu (2004), Toward modeling turbulent suspension of sand in the nearshore, *Journal of Geophysical Research: Oceans*, *109*(C6), C06018, doi:10.1029/2003JC002240.

Hsu, T.-J., and B. Raubenheimer (2006), A numerical and field study on inner-surf and swash sediment transport, *Continental Shelf Research*, *26*(5), 589–598, doi:10.1016/j.csr.2006.02.004.

Hsu, T.-J., J. T. Jenkins, and P. L.-F. Liu (2004), On two-phase sediment transport: sheet flow of massive particles, *Proceedings of the Royal Society of London. Series A: Mathematical, Physical and Engineering Sciences*, *460*(2048), 2223–2250, doi:10.1098/rspa.2003.1273.

Huang, Z.-C., S.-C. Hsiao, H.-H. Hwung, and K.-A. Chang (2009), Turbulence and energy dissipations of surf-zone spilling breakers, *Coastal Engineering*, *56*(7), 733–746, doi:10.1016/j.coastaleng.2009.02.003.

Huang, Z.-C., L. Lenain, W. K. Melville, J. H. Middleton, B. Reineman, N. Statom, and R. M. McCabe (2012), Dissipation of wave energy and turbulence in a shallow coral reef lagoon, *Journal of Geophysical Research: Oceans*, *117*(C3), C03015, doi:10.1029/2011JC007202.

Hughes, M. G. (1995), Friction Factors for Wave Uprush, *Journal of Coastal Research*, *11*(4), 1089–1098.

Hughes, M. G., and T. E. Baldock (2004), Eulerian flow velocities in the swash zone: Field data and model predictions, *Journal of Geophysical Research: Oceans*, *109*(C8), C08009, doi:10.1029/2003JC002213.

Hughes, M. G., and A. S. Moseley (2007), Hydrokinematic regions within the swash zone, *Continental Shelf Research*, *27*(15), 2000–2013, doi:10.1016/j.csr.2007.04.005.

Hughes, M. G., G. Masselink, and R. W. Brander (1997), Flow velocity and sediment transport in the swash zone of a steep beach, *Marine Geology*, *138*(1–2), 91–103, doi:10.1016/S0025-3227(97)00014-5.

Hughes, M. G., T. Aagaard, and T. E. Baldock (2007), Suspended Sediment in the Swash Zone: Heuristic Analysis of Spatial and Temporal Variations in Concentration, *Journal of Coastal Research*, *23*(6), 1345–1354, doi:10.2112/05-0531.1.

Hurther, D., P. D. Thorne, M. Bricault, U. Lemmin, and J.-M. Barnoud (2011), A multi-frequency Acoustic Concentration and Velocity Profiler (ACVP) for boundary layer measurements of fine-scale flow and sediment transport processes, *Coastal Engineering*, *58*(7), 594–605, doi:10.1016/j.coastaleng.2011.01.006.

Jackson, N. L., G. Masselink, and K. F. Nordstrom (2004), The role of bore collapse and local shear stresses on the spatial distribution of sediment load in the uprush of an intermediate-state beach, *Marine Geology*, *203*(1–2), 109–118, doi:10.1016/S0025-3227(03)00328-1.

Jackson, N. L., K. F. Nordstrom, D. R. Smith, and S. Saini (2014), Delivery and movement of horseshoe crab eggs (Limulus polyphemus) in the breaking waves and swash uprush of an estuarine foreshore, *Estuarine, Coastal and Shelf Science*, *136*, 191–198, doi:10.1016/j.ecss.2013.10.025.

Jackson, P. D., D. Taylor Smith, and P. N. Stanford (1978), Resistivity-porosity-particle shape relationships for marine sands, *Geophysics*, *43*(6), 1250–1268, doi:10.1190/1.1440891.

Julien, P. Y., and D. B. Simons (1985), Sediment transport capacity of overland flow, *Transactions of the ASAE*, *28*(3), 755–762.

Karambas, T. (2003), Modelling of infiltration-exfiltration effects of cross-shore sediment transport in the swash zone, *Coastal Engineering Journal*, *45*(1), 63–82, doi:10.1142/S057856340300066X.

Kikkert, G. A., T. O'Donoghue, D. Pokrajac, and N. Dodd (2012), Experimental study of bore-driven swash hydrodynamics on impermeable rough slopes, *Coastal Engineering*, *60*, 149–166, doi:10.1016/j.coastaleng.2011.09.006.

Kolmogorov, A. N. (1991), The local structure of turbulence in incompressible viscous fluid for very large Reynolds numbers, *Proceedings of the Royal Society of London. Series A: Mathematical and Physical Sciences*, *434*(1890), 9–13, doi:10.1098/rspa.1991.0075.

Küuntz, M., J. C. Mareschal, and P. Lavallée (2000), Numerical estimation of electrical conductivity in saturated porous media with a 2-D lattice gas, *Geophysics*, *65*(3), 766–772, doi:10.1190/1.1444775.

Lanckriet, T., and J. A. Puleo (2010), Spatially dense kinematic maps in the swash zone using a continuity-based imaging technique, American Geophysical Union, San Francisco, CA.

Lanckriet, T., J. A. Puleo, and N. Waite (2013), A Conductivity Concentration Profiler for Sheet Flow Sediment Transport, *IEEE Journal of Oceanic Engineering*, *38*(1), 55 –70, doi:10.1109/JOE.2012.2222791.

Landauer, R. (1952), The electrical resistance of binary metallic mixtures, *Journal of Applied Physics*, *23*(7), 779–784, doi:http://dx.doi.org/10.1063/1.1702301.

Lemaitre, J., J. P. Troadec, D. Bideau, A. Gervois, and E. Bougault (1988), The formation factor of the pore space of binary mixtures of spheres, *Journal of Physics D: Applied Physics*, *21*(11), 1589, doi:10.1088/0022-3727/21/11/007.

Li, X., and G. C. M. Meijer (2005), A low-cost and accurate interface for four-electrode conductivity sensors, *IEEE Transactions on Instrumentation and Measurement*, *54*(6), 2433–2437, doi:10.1109/TIM.2005.858130.

Longo, S., M. Petti, and I. J. Losada (2002), Turbulence in the swash and surf zones: a review, *Coastal Engineering*, *45*(3–4), 129–147, doi:10.1016/S0378-3839(02)00031-5.

Lumley, J. L., and E. A. Terray (1983), Kinematics of Turbulence Convected by a Random Wave Field, *Journal of Physical Oceanography*, *13*(11), 2000–2007, doi:10.1175/1520-0485(1983)013<2000:KOTCBA>2.0.CO;2.

Masselink, G., and M. Hughes (1998), Field investigation of sediment transport in the swash zone, *Continental Shelf Research*, *18*(10), 1179–1199, doi:10.1016/S0278-4343(98)00027-2.

Masselink, G., and J. A. Puleo (2006), Swash-zone morphodynamics, *Continental Shelf Research*, *26*(5), 661–680, doi:10.1016/j.csr.2006.01.015.

Masselink, G., and P. Russell (2006), Flow velocities, sediment transport and morphological change in the swash zone of two contrasting beaches, *Marine Geology*, *227*(3–4), 227–240, doi:10.1016/j.margeo.2005.11.005.

Masselink, G., and I. L. Turner (2012), Large-scale laboratory investigation into the effect of varying back-barrier lagoon water levels on gravel beach morphology and swash zone sediment transport, *Coastal Engineering*, *63*, 23–38, doi:10.1016/j.coastaleng.2011.12.007.

Masselink, G., A. Ruju, D. Conley, I. Turner, G. Ruessink, A. Matias, C. Thompson, B. Castelle, and G. Wolters (in preparation), Large-scale Barrier Dynamics Experiment II (BARDEX II): experimental design, instrumentation, test programme and data set, *Coastal Engineering*.

Masselink, G., D. Evans, M. G. Hughes, and P. Russell (2005), Suspended sediment transport in the swash zone of a dissipative beach, *Marine Geology*, *216*(3), 169–189, doi:10.1016/j.margeo.2005.02.017.

Masselink, G., P. Russell, I. Turner, and C. Blenkinsopp (2009), Net sediment transport and morphological change in the swash zone of a high-energy sandy beach from swash event to tidal cycle time scales, *Marine Geology*, *267*(1–2), 18–35, doi:10.1016/j.margeo.2009.09.003.

Masselink, G., P. Russell, C. Blenkinsopp, and I. Turner (2010), Swash zone sediment transport, step dynamics and morphological response on a gravel beach, *Marine Geology*, *274*(1–4), 50–68, doi:10.1016/j.margeo.2010.03.005.

McLean, S. R., J. S. Ribberink, C. M. Dohmen-Janssen, and W. N. Hassan (2001), Sand Transport in Oscillatory Sheet Flow with Mean Current, *Journal of Waterway, Port, Coastal, and Ocean Engineering*, *127*(3), 141–151, doi:10.1061/(ASCE)0733-950X(2001)127:3(141).

Meyer-Peter, E., and R. Müller (1948), Formulas for bed-load transport, pp. 39–64, Proceedings of the 2nd Meeting of the International Association for Hydraulic Structures Research, Stockholm, Sweden.

Miles, J. W. (1961), On the stability of heterogeneous shear flows, *Journal of Fluid Mechanics*, *10*(04), 496–508, doi:10.1017/S0022112061000305.

Mohrholz, V., H. Prandke, and H. U. Lass (2008), Estimation of TKE dissipation rates in dense bottom plumes using a Pulse Coherent Acoustic Doppler Profiler (PC-ADP) — Structure function approach, *Journal of Marine Systems*, *70*(3–4), 217–239, doi:10.1016/j.jmarsys.2007.03.004.

Montreuil, S., and B. Long (2009), Bedload sediment transport budget using CT-Scanning, in *Proc. Coastal Dynamics 2009*, pp. 1–11, ASCE-COPRI, Tokyo, Japan.

Moreno, M., T. J. Ferrero, V. Granelli, V. Marin, G. Albertelli, and M. Fabiano (2006), Across shore variability and trophodynamic features of meiofauna in a microtidal beach of the NW Mediterranean, *Estuarine, Coastal and Shelf Science*, *66*(3–4), 357–367, doi:10.1016/j.ecss.2005.08.016.

Mori, N., T. Suzuki, and S. Kakuno (2007), Noise of Acoustic Doppler Velocimeter Data in Bubbly Flows, *Journal of Engineering Mechanics*, *133*(1), 122–125, doi:10.1061/(ASCE)0733-9399(2007)133:1(122).

Nielsen, P. (1992), *Coastal bottom boundary layers and sediment transport*, Advanced Series on Ocean Engineering, World Scientific, Singapore.

Nielsen, P. (1998), Coastal groundwater hydrodynamics, in *Proc. Coastal Dynamics '97*, pp. 546–555.

Nielsen, P. (2002), Shear stress and sediment transport calculations for swash zone modelling, *Coastal Engineering*, *45*(1), 53–60, doi:10.1016/S0378-3839(01)00036-9.

O'Donoghue, T., and S. Wright (2004a), Concentrations in oscillatory sheet flow for well sorted and graded sands, *Coastal Engineering*, *50*(3), 117–138, doi:10.1016/j.coastaleng.2003.09.004.

O'Donoghue, T., and S. Wright (2004b), Flow tunnel measurements of velocities and sand flux in oscillatory sheet flow for well-sorted and graded sands, *Coastal Engineering*, *51*(11–12), 1163–1184, doi:10.1016/j.coastaleng.2004.08.001.

O'Donoghue, T., D. Pokrajac, and L. J. Hondebrink (2010), Laboratory and numerical study of dambreak-generated swash on impermeable slopes, *Coastal Engineering*, *57*(5), 513–530, doi:10.1016/j.coastaleng.2009.12.007.

Osborne, P. D., and G. A. Rooker (1999), Sand Re-Suspension Events in a High Energy Infragravity Swash Zone, *Journal of Coastal Research*, *15*(1), 74–86.

Othman, I. K., T. E. Baldock, and D. P. Callaghan (2014), Measurement and modelling of the influence of grain size and pressure gradient on swash uprush sediment transport, *Coastal Engineering*, *83*, 1–14, doi:10.1016/j.coastaleng.2013.09.001.

Petti, M., and S. Longo (2001), Turbulence experiments in the swash zone, *Coastal Engineering*, *43*(1), 1–24, doi:10.1016/S0378-3839(00)00068-5.

Pieterse, A., J. A. Puleo, and T. E. McKenna (2013), Hydrodynamics and inundation of a tidal saltmarsh in Kent County, Delaware, American Geophysical Union, San Francisco, CA.

Pope, S. B. (2000), *Turbulent Flows*, Cambridge University Press, Cambridge, UK.

Pugh, F. J., and K. C. Wilson (1999), Velocity and concentration distributions in sheet flow above plane beds, *Journal of Hydraulic Engineering*, *125*(2), 117–125, doi:10.1061/(ASCE)0733-9429(1999)125:2(117).

Puleo, J. A. (2009), Tidal Variability of Swash-Zone Sediment Suspension and Transport, *Journal of Coastal Research*, *254*, 937–948, doi:10.2112/08-1031.1.

Puleo, J. A., and T. Butt (2006), The first international workshop on swash-zone processes, *Continental Shelf Research*, *26*(5), 556–560, doi:10.1016/j.csr.2006.01.008.

Puleo, J. A., and K. T. Holland (2001), Estimating swash zone friction coefficients on a sandy beach, *Coastal Engineering*, *43*(1), 25–40, doi:10.1016/S0378-3839(01)00004-7.

Puleo, J. A., T. Lanckriet, D. Conley, and D. Foster (submitted), Sediment transport partitioning in the swash zone of a large-scale laboratory beach, *Coastal Engineering*.

Puleo, J. A., R. A. Beach, R. A. Holman, and J. S. Allen (2000), Swash zone sediment suspension and transport and the importance of bore-generated turbulence, *Journal of Geophysical Research*, *105*(C7), 17021–17044, doi:10.1029/2000JC900024.

Puleo, J. A., K. T. Holland, N. G. Plant, D. N. Slinn, and D. M. Hanes (2003), Fluid acceleration effects on suspended sediment transport in the swash zone, *Journal of Geophysical Research*, *108*(C11), 3350–3362, doi:10.1029/2003JC001943.

Puleo, J. A., A. Farhadzadeh, and N. Kobayashi (2007), Numerical simulation of swash zone fluid accelerations, *Journal of Geophysical Research*, *112*(C7), C07007, doi:10.1029/2006JC004084.

Puleo, J. A., J. Faries, M. Davidson, and B. Hicks (2010), A Conductivity Sensor for Nearbed Sediment Concentration Profiling, *Journal of Atmospheric and Oceanic Technology*, *27*(2), 397–408, doi:10.1175/2009JTECHO718.1.

Puleo, J. A., T. Lanckriet, and P. Wang (2012), Near bed cross-shore velocity profiles, bed shear stress and friction on the foreshore of a microtidal beach, *Coastal Engineering*, *68*, 6–16, doi:10.1016/j.coastaleng.2012.04.007.

Puleo, J. A., T. Lanckriet, and C. Blenkinsopp (2014a), Bed level fluctuations in the inner surf and swash zone of a dissipative beach, *Marine Geology*, *349*, 99–112, doi:10.1016/j.margeo.2014.01.006.

Puleo, J. A. et al. (2014b), Comprehensive Field Study of Swash-Zone Processes. I: Experimental Design with Examples of Hydrodynamic and Sediment Transport Measurements, *Journal of Waterway, Port, Coastal, and Ocean Engineering*, *140*(1), 14–28, doi:10.1061/(ASCE)WW.1943-5460.0000210.

Rapp, R. J., and W. K. Melville (1990), Laboratory Measurements of Deep-Water Breaking Waves, *Philosophical Transactions of the Royal Society of London. Series A, Mathematical and Physical Sciences*, *331*(1622), 735–800, doi:10.1098/rsta.1990.0098.

Raubenheimer, B., S. Elgar, and R. T. Guza (2004), Observations of swash zone velocities: A note on friction coefficients, *Journal of Geophysical Research*, *109*(C1), C01027, doi:10.1029/2003JC001877.

Ribberink, J. S., and A. Al-Salem (1992), *Time-dependent sediment transport phenomena in oscillatory boundary-layer flow under sheet-flow conditions.*, Delft Hydraulics, The Netherlands.

Ribberink, J. S., and A. A. Al-Salem (1994), Sediment transport in oscillatory boundary layers in cases of rippled beds and sheet flow, *Journal of Geophysical Research*, *99*(C6), 12707–12,727, doi:10.1029/94JC00380.

Ribberink, J. S., and A. A. Al-Salem (1995), Sheet flow and suspension of sand in oscillatory boundary layers, *Coastal Engineering*, *25*(3–4), 205–225, doi:10.1016/0378-3839(95)00003-T.

Ribberink, J. S., C. M. Dohmen-Janssen, D. M. Hanes, S. R. McLean, and C. Vincent (2000), Near-Bed Sand Transport Mechanisms Under Waves: A Large-Scale Flume Experiment (Sistex99), in *Proc. 27th Int. Conf. Coastal Eng.*, pp. 254–254, ASCE, Sydney, Australia.

Ribberink, J. S., J. J. van der Werf, T. O'Donoghue, and W. N. M. Hassan (2008), Sand motion induced by oscillatory flows: Sheet flow and vortex ripples, *Journal of Turbulence*, *9*(20), 1–32, doi:10.1080/14685240802220009.

Rodriguez, A., A. Sánchez-Arcilla, J. M. Redondo, and C. Mösso (1999), Macroturbulence measurements with electromagnetic and ultrasonic sensors: a comparison under high-turbulent flows, *Experiments in Fluids*, *27*(1), 31–42, doi:10.1007/s003480050326.

Ross, M. A., and A. J. Mehta (1989), On the Mechanics of Lutoclines and Fluid Mud, *Journal of Coastal Research*, *5*, 51–62, doi:10.2307/25735365.

Ruessink, B. G., H. Michallet, T. Abreu, F. Sancho, D. A. V. der A, J. J. V. der Werf, and P. A. Silva (2011), Observations of velocities, sand concentrations, and fluxes under velocity-asymmetric oscillatory flows, *Journal of Geophysical Research*, *116*(C3), C03004, doi:10.1029/2010JC006443.

Russell, P. E., G. Masselink, C. Blenkinsopp, and I. L. Turner (2009), A Comparison of Berm Accretion in the Swash Zone on Sand and Gravel Beaches at the Timescale of Individual Waves, *Journal of Coastal Research*, 1791–1795.

Sánchez-Arcilla, A., I. Cáceres, L. van Rijn, and J. Grüne (2011), Revisiting mobile bed tests for beach profile dynamics, *Coastal Engineering*, *58*(7), 583–593, doi:10.1016/j.coastaleng.2011.01.005.

Savage, S. B., and S. Mckeown (1983), Shear stresses developed during rapid shear of concentrated suspensions of large spherical particles between concentric cylinders, *Journal of Fluid Mechanics*, *127*, 453–472, doi:10.1017/S0022112083002827.

Schretlen, J. J. L. M., J. S. Ribberink, and T. O'Donoghue (2010), Boundary layer flow and sand transport under full scale surface waves, in *Proc. 32nd Int. Conf. Coastal Eng.*, vol. 1, ASCE, Shanghai, China. [online] Available from: http://journals.tdl.org/ICCE/article/view/1271

Shields, A. (1936), Anwendung der Ähnlichkeitsmechanik und der Turbulenzforschung auf die Geschiebebewegung, *Preussische Versuchsanstalt für Wasserbau und Schiffbau*, *26*, 524–526.

Shook, C., R. Gillies, D. Haas, W. Husband, and M. Small (1982), Flow of coarse and fine sand slurries in pipelines., *Journal of Pipelines*, *3*(1), 13–21.

Sleath, J. F. A. (1999), Conditions for plug formation in oscillatory flow, *Continental Shelf Research*, *19*(13), 1643–1664, doi:10.1016/S0278-4343(98)00096-X.

Song, C., P. Wang, and H. A. Makse (2008), A phase diagram for jammed matter, *Nature*, *453*(7195), 629–632, doi:10.1038/nature06981.

Sou, I. M., and H. Yeh (2011), Laboratory study of the cross-shore flow structure in the surf and swash zones, *Journal of Geophysical Research*, *116*(C3), C03002, doi:10.1029/2010JC006700.

Sou, I. M., E. A. Cowen, and P. L.-F. Liu (2010), Evolution of the Turbulence Structure in the Surf and Swash Zones, *Journal of Fluid Mechanics*, *644*, 193–216, doi:10.1017/S0022112009992321.

Spinewine, B., H. Capart, L. Fraccarollo, and M. Larcher (2011), Laser stripe measurements of near-wall solid fraction in channel flows of liquid-granular mixtures, *Experiments in Fluids*, *50*(6), 1507–1525, doi:10.1007/s00348-010-1009-7.

Steenhauer, K., D. Pokrajac, and T. O'Donoghue (2012), Numerical model of swash motion and air entrapment within coarse-grained beaches, *Coastal Engineering*, *64*(0), 113–126, doi:10.1016/j.coastaleng.2012.01.004.

Stockdon, H. F., R. A. Holman, P. A. Howd, and A. H. Sallenger Jr. (2006), Empirical parameterization of setup, swash, and runup, *Coastal Engineering*, *53*(7), 573–588, doi:10.1016/j.coastaleng.2005.12.005.

Sumer, B. M., A. Kozakiewicz, J. Fredsoe, and R. Deigaard (1996), Velocity and Concentration Profiles in Sheet-Flow Layer of Movable Bed, *Journal of Hydraulic Engineering*, *122*(10), 549–558, doi:10.1061/(ASCE)0733-9429(1996)122:10(549).

Tennekes, H., and J. L. Lumley (1972), *A First Course in Turbulence*, MIT press, Cambridge, MA.

Thornton, E. B., and R. T. Guza (1982), Energy saturation and phase speeds measured on a natural beach, *Journal of Geophysical Research: Oceans*, *87*(C12), 9499–9508, doi:10.1029/JC087iC12p09499.

Torres-Freyermuth, A., J. A. Puleo, and D. Pokrajac (2013), Modeling swash-zone hydrodynamics and shear stresses on planar slopes using Reynolds-Averaged Navier–Stokes equations, *Journal of Geophysical Research: Oceans*, *118*(2), 1019–1033, doi:10.1002/jgrc.20074.

Trowbridge, J., and S. Elgar (2001), Turbulence Measurements in the Surf Zone, *Journal of Physical Oceanography*, *31*(8), 2403–2417, doi:10.1175/1520-0485(2001)031<2403:TMITSZ>2.0.CO;2.

Trowbridge, J. H., and G. C. Kineke (1994), Structure and dynamics of fluid muds on the Amazon Continental Shelf, *Journal of Geophysical Research: Oceans*, *99*(C1), 865–874, doi:10.1029/93JC02860.

Turner, I. L., and G. Masselink (1998), Swash infiltration-exfiltration and sediment transport, *Journal of Geophysical Research: Oceans*, *103*(C13), 30813–30824, doi:10.1029/98JC02606.

Turner, I. L., P. E. Russell, and T. Butt (2008), Measurement of wave-by-wave bed-levels in the swash zone, *Coastal Engineering*, *55*(12), 1237–1242, doi:10.1016/j.coastaleng.2008.09.009.

Turner, J. S. (1979), *Buoyancy effects in fluids*, Cambridge University Press, Cambridge, UK.

Van der A, D. A., T. O'Donoghue, and J. S. Ribberink (2010), Measurements of sheet flow transport in acceleration-skewed oscillatory flow and comparison with practical formulations, *Coastal Engineering*, *57*(3), 331–342, doi:10.1016/j.coastaleng.2009.11.006.

Van der Zanden, J., J. Alsina, I. Cáceres, R. Buijsrogge, and J. Ribberink (2013), New CCM technique for sheet flow measurements and its first application in swash zone experiments, in *Proceedings of the 6th International Short Course/Conference on Applied Coastal Research*, Lisbon, Portugal.

Van Rooijen, A., A. Reniers, J. van Thiel de Vries, C. Blenkinsopp, and R. Mccall (2012), Modelling swash zone sediment transport at Le Truc Vert, France, in *Proc. 33nd Int. Conf. Coastal Eng.*, ASCE, Santander, Spain.

Veron, F., and W. K. Melville (1999), Pulse-to-Pulse Coherent Doppler Measurements of Waves and Turbulence, *Journal of Atmospheric and Oceanic Technology*, *16*(11), 1580–1597, doi:10.1175/1520-0426(1999)016<1580:PTPCDM>2.0.CO;2.

Voulgaris, G., and J. H. Trowbridge (1998), Evaluation of the Acoustic Doppler Velocimeter (ADV) for Turbulence Measurements, *Journal of Atmospheric and Oceanic Technology*, *15*(1), 272–289, doi:10.1175/1520-0426(1998)015<0272:EOTADV>2.0.CO;2.

Wahl, T. L. (2003), Discussion of "Despiking Acoustic Doppler Velocimeter Data" by Derek G. Goring and Vladimir I. Nikora, *Journal of Hydraulic Engineering*, *129*(6), 484–487, doi:10.1061/(ASCE)0733-9429(2003)129:6(484).

Wang, P., E. R. Smith, and B. A. Ebersole (2002), Large-Scale Laboratory Measurements of Longshore Sediment Transport under Spilling and Plunging Breakers, *Journal of Coastal Research*, *18*(1), 118–135.

Wang, Y.-H., and G.-H. Yu (2007), Velocity and concentration profiles of particle movement in sheet flows, *Advances in Water Resources*, *30*(5), 1355–1359, doi:10.1016/j.advwatres.2006.11.012.

Whipple, A. C., and R. A. Luettich (2009), A comparison of acoustic turbulence profiling techniques in the presence of waves, *Ocean Dynamics*, *59*(5), 719–729, doi:10.1007/s10236-009-0208-3.

Wiles, P. J., T. P. Rippeth, J. H. Simpson, and P. J. Hendricks (2006), A novel technique for measuring the rate of turbulent dissipation in the marine environment, *Geophysical Research Letters*, *33*(21), L21608, doi:10.1029/2006GL027050.

Wilson, K. C. (1987), Analysis of Bed-Load Motion at High Shear Stress, *Journal of Hydraulic Engineering*, *113*(1), 97–103, doi:10.1061/(ASCE)0733-9429(1987)113:1(97).

Winterwerp, J. C. (2001), Stratification effects by cohesive and noncohesive sediment, *Journal of Geophysical Research: Oceans*, *106*(C10), 22559–22574, doi:10.1029/2000JC000435.

Yu, X., T.-J. Hsu, and D. M. Hanes (2010), Sediment transport under wave groups: Relative importance between nonlinear waveshape and nonlinear boundary layer streaming, *Journal of Geophysical Research*, *115*(C2), C02013, doi:10.1029/2009JC005348.

Yu, X., T.-J. Hsu, J. T. Jenkins, and P. L.-F. Liu (2012), Predictions of vertical sediment flux in oscillatory flows using a two-phase, sheet-flow model, *Advances in Water Resources*, *48*(0), 2–17, doi:10.1016/j.advwatres.2012.05.012.

Yu, Z., H. D. Niemeyer, and W. T. Bakker (1990), Site investigation on sand concentration in the sheet-flow layer, in *Proc. 22nd Int. Conf. Coastal Eng.*, pp. 2361–2371, ASCE, Delft, The Netherlands.

Zala Flores, N., and J. F. A. Sleath (1998), Mobile layer in oscillatory sheet flow, *Journal of Geophysical Research*, *103*(C6), 12783–12793, doi:199810.1029/98JC00691.

Zhang, Q., and P. L.-F. Liu (2008), A numerical study of swash flows generated by bores, *Coastal Engineering*, *55*(12), 1113–1134, doi:10.1016/j.coastaleng.2008.04.010.

Appendix

COPYRIGHT NOTES

The abstract (in part), Chapter 2, and Chapter 7 (in part) are ©2013 IEEE. Reproduced and modified, with permission, from Lanckriet, T., J. A. Puleo, and N. Waite (2013), A Conductivity Concentration Profiler for Sheet Flow Sediment Transport, *IEEE Journal of Oceanic Engineering*, 38(1), 55 –70, doi:10.1109/JOE.2012.2222791. Statement from IEEE:

> The IEEE does not require individuals working on a thesis to obtain a formal reuse license, however, you may print out this statement to be used as a permission grant:
>
> Requirements to be followed when using any portion (e.g., figure, graph, table, or textual material) of an IEEE copyrighted paper in a thesis:
>
> 1) In the case of textual material (e.g., using short quotes or referring to the work within these papers) users must give full credit to the original source (author, paper, publication) followed by the IEEE copyright line © 2011 IEEE.
>
> 2) In the case of illustrations or tabular material, we require that the copyright line © [Year of original publication] IEEE appear prominently with each reprinted figure and/or table.
>
> 3) If a substantial portion of the original paper is to be used, and if you are not the senior author, also obtain the senior author's approval.
>
> Requirements to be followed when using an entire IEEE copyrighted paper in a thesis:
>
> 1) The following IEEE copyright/ credit notice should be placed prominently in the references: © [year of original publication] IEEE.

The abstract (in part), section 2.3 (in part), section 3.2 (in part), Chapter 4, section 6.2 (in part) and Chapter 7 (in part) are reproduced and modified, with permission from ASCE, from Lanckriet, T., J. Puleo, G. Masselink, I. Turner, D. Conley, C. Blenkinsopp, and P. Russell (2014), Comprehensive Field Study of Swash-Zone Processes. II: Sheet Flow Sediment Concentrations during Quasi-Steady Backwash, *Journal of Waterway, Port, Coastal, and Ocean Engineering*, 140(1), 29–42, doi:10.1061/(ASCE)WW.1943-5460.0000209.

Chapter 3 (in part) is reproduced and modified, with permission from ASCE, from Puleo, J. A. et al. (2014), Comprehensive Field Study of Swash-Zone Processes. I: Experimental Design with Examples of Hydrodynamic and Sediment Transport Measurements, *Journal of Waterway, Port, Coastal, and Ocean Engineering*, 140(1), 14–28, doi:10.1061/(ASCE)WW.1943-5460.0000210.

Statement from ASCE:

"As an ASCE author, you are permitted to reuse you own content for another ASCE or non-ASCE publication. Please add the full credit line "With permission from ASCE" to your source citation. Please print this page for your records."

Chapter 5 and Chapter 7 (in part) are reproduced and modified, with permission from John Wiley and Sons, from Lanckriet, T., and J. A. Puleo (2013), Near-bed turbulence dissipation measurements in the inner surf and swash zone, *Journal of Geophysical Research: Oceans*, 118(12), 6634–6647, doi:10.1002/2013JC009251. Statement from John Wiley and Sons:

JOHN WILEY AND SONS LICENSE TERMS AND CONDITIONS

Feb 12, 2014

This is a License Agreement between Thijs M. Lanckriet ("You") and John Wiley and Sons ("John Wiley and Sons") provided by Copyright Clearance Center ("CCC"). The license consists of your order details, the terms and conditions provided by John Wiley and Sons, and the payment terms and conditions.

All payments must be made in full to CCC. For payment instructions, please see information listed at the bottom of this form.

License Number	3326631021314
License date	Feb 12, 2014
Licensed content publisher	John Wiley and Sons
Licensed content publication	Journal of Geophysical Research: Oceans
Licensed content title	Near-bed turbulence dissipation measurements in the inner surf and swash zone
Licensed copyright line	©2013. American Geophysical Union. All Rights Reserved.
Licensed content author	Thijs Lanckriet,Jack A. Puleo
Licensed content date	Dec 6, 2013
Start page	6634
End page	6647
Type of use	Dissertation/Thesis
Requestor type	Author of this Wiley article
Format	Print and electronic
Portion	Full article
Will you be translating?	No
Title of your thesis / dissertation	Near-bed hydrodynamics and sediment transport in the swash zone
Expected completion date	May 2014
Expected size (number of pages)	200
Total	0.00 USD
Terms and Conditions	